RICE UNIVERSITY

Modifying Terahertz Waveguide Geometries: Bends, Tapers, and Grooves

by

Victoria Astley

A THESIS SUBMITTED
IN PARTIAL FULFILLMENT OF THE
REQUIREMENTS FOR THE DEGREE

Doctor of Philosophy

APPROVED, THESIS COMMITTEE

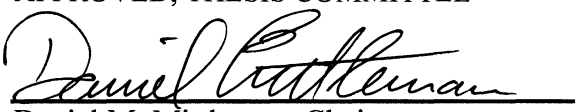

Daniel M. Mittleman, Chair
Professor,
Electrical and Computer Engineering

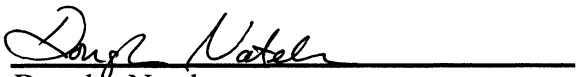

Douglas Natelson
Professor, Physics and Astronomy
Electrical and Computer Engineering

Kevin Kelly
Associate Professor,
Electrical and Computer Engineering

HOUSTON, TEXAS
April 2012

Abstract

Modifying Terahertz Waveguide Geometries: Bends, Tapers, and Grooves

by

Victoria Astley

Terahertz waveguides are the focus of considerable research interest due to their potential for sensing, imaging and communications applications. Two of the most promising designs are the metal wire waveguide and the parallel-plate waveguide.

The metal wire waveguide exhibits excellent low loss and low dispersion characteristics. However, the radiation is only weakly coupled to the wire and the beam extends a great distance from the waveguide, which can lead to high bending loss. In my research I show that this large beam extent also gives a high degree of flexibility in the geometry required to couple radiation into the waveguide or between waveguide sections. I also show that the traditional formalism of bending loss is incomplete, and that there is an optimum radius of curvature to reduce loss.

The relationship between the beam extent and the radius of the wire presents the possibility of a tapered waveguide to confine the radiation as it propagates. I here present experimental data and simulations results to verify this subwavelength confinement at the tip of a tapered metal wire waveguide, which is of great interest for near-field imaging applications.

The parallel-plate waveguide is another design frequently employed due to its low loss and low dispersion characteristics. Resonant structures may also be easily incorporated into the waveguide for sensing and filtering applications. One such structure is a single rectangular groove, which serves as a notch filter with a very narrow linewidth when the transverse-electric (TE) mode of the waveguide is excited, though its physical origin is poorly understood. In this work I present a detailed experimental and theoretical study of the rectangular resonant cavity in a TE-mode parallel-plate waveguide, particularly with respect to its potential as a microfluidic refractive index sensor. This study is extended to include the possibility of two grooves, in both coupled and non-coupled geometries, and their efficacy as multichannel or high-resolution single-channel microfluidic sensors.

Acknowledgments

This thesis would not have been possible without the help and support of many people. First and foremost I would like to thank my advisor Dr. Daniel Mittleman, from whom I have learned so much over these years. I am grateful for his guidance and encouragement, scientific expertise, patience and enthusiasm (and sense of humor), along with his willingness to indulge my eccentricities in the name of motivation. I am also grateful to the members of my thesis committee, Dr. Doug Natelson and Dr. Kevin Kelly, for their time and insight.

I would also like to thank Dr. Jason Deibel, whose guidance in my first years at Rice was invaluable and who taught me the experimental skills I would later depend on for all the work presented in this thesis. And I must express my sincere thanks to Dr. Rajind Mendis for always pushing me to a higher standard of excellence no matter how much I resisted. I wouldn't be half the scientist I am without him.

I also want to thank group members past and present Marx Mbonye, Jingbo Liu, Kim Reichel, Daniel Nickel, Dr. Kanglin Wang, Dr. Hui Zhan, and Dr. Jonathan Laib for all the beach barbecues, political debates, kvetching sessions and conference shenanigans that made our lab group so much fun. I am also grateful to my labmates for all their scientific input and problem-solving advice and to my undergraduate assistants Jonathan Jones, Blake McCracken and Julianna Scheiman for their help in collecting much of the data presented in this thesis.

Lastly I would like to thank my friends and family for their support. I could not have done this without my parents, to whom I am grateful for their endless love, support, patience, sympathy, encouragement and care packages. I would say I hope they are proud of me, but I know they have never been anything else. I would also like to thank my brother Henry, with whom I could commiserate about the trials and tribulations of experimental science, and my sister-in law Gemma, with whom I could commiserate about Henry. (Kidding!) And finally I would like to thank Rey and Chad (my partners in crime) and all my friends online and IRL, my fellow travelers on the journey through graduate school, my co-adventurers on the road to and from Greyhawk, and my shipmates on the Kalmar Nyckel, for adding a rich texture of joy to my life.

Contents

List of Figures

List of Tables

Chapter 1

Introduction

1.1. Introduction and Background

"Terahertz radiation" is the term used to describe electromagnetic radiation with a frequency generally defined as between 0.1-10 THz, a range that overlaps somewhat with microwave or millimeter wave radiation. This range was for many years known as the "THz gap", a part of the spectrum between the microwave and infrared regimes for which there was no practical means of generation or detection. The frequency of THz waves is too high for many electronic techniques used in the microwave regime, such as horn antennas or coaxial waveguides, but the frequency is also too low for many optical techniques employed in the infrared, such as fiber optic waveguides and photonic detection mechanisms. This meant that novel techniques had to be developed to explore this frequency range, but it proved to be

a worthwhile effort due to the huge potential and vast array of applications that make use of the unique properties of THz radiation.

A surge of interest in terahertz in the 1980s led to the development of terahertz time-domain spectroscopy, the technique used in this thesis. Time-domain spectroscopy involves a direct measurement of the magnitude of the electric field over time, rather than a frequency-domain measurement which only gives the spectral content of the signal, or a photon-counting technique with even more limited information. The advantage of time-domain measurement is that it includes much more information: the polarity of the electric field and the amplitude and phase over a wide range of component frequencies. This allows traditional spectral measurements but also phase-dependent imaging, polarization manipulation, determination of the complex refractive index, etc. While frequency-domain measurement or intensity measurements using bolometers have their applications, the versatility of time-domain measurement is what makes it the dominant THz modality and the technique that provides the foundation for this work.

As mentioned above, terahertz research includes a very wide range of applications, with more being developed every day [2]. Terahertz spectroscopy provides a valuable tool for characterizing materials, particularly since the rotational modes of a huge range of molecules have resonances in the THz range. It is used, for example, to investigate DNA and other biomolecules [3], explosives and chemicals of security interest [4], and semiconductors and other solid-state materials [5-7]. THz imaging has its own catalog of applications, many taking

advantage of the transparency of cloth, cardboard, paper and other packing materials in the THz and of the sensitivity of THz to the presence of water or water vapor [8]. Examples of imaging applications include characterizations of semiconductor behavior [9] and industrial studies of materials such as space shuttle foam [10], as well as more esoteric applications such as art restoration [11] and tree-ring analysis [12]. Besides spectroscopy and imaging, THz has attracted attention for studying electron transport in materials such as carbon nanotubes [13] and for potential communications technology [14], among other applications.

One of the drawbacks of terahertz radiation that limits its potential in a real-world environment is the lack of an efficient waveguide – i.e. a means to transmit the radiation over long distances without excessive loss of information or signal degradation and to transmit along pathways that are not unobstructed line-of-sight. The revolution in telecommunications that resulted from the development of fiber optic cables is excellent proof of the value of a good waveguide.

Unfortunately, fiber optic cables do not effectively carry terahertz radiation, nor do many other optical waveguides, which are generally constructed of materials like glass and silica which are highly absorptive/opaque at terahertz frequencies. Techniques in microwave such as transmission lines [15] and hollow metal waveguides with rectangular or cylindrical cross-sections [16] are effective but dispersive, distorting the shape of the THz pulse and limiting the potential applications. Again, new techniques must be developed to bridge the terahertz gap.

Over the years, a wide variety of THz waveguides have been developed, each performing differently on the various criteria for waveguide performance. These criteria include the waveguide's characteristic attenuation, dispersion, bending loss, beam extent, supported bandwidth and coupling efficiency, among others. Many waveguides will perform well for some criteria and not others, such as the low-loss high-dispersion hollow waveguides mentioned above. Due to the wide range of THz applications, different waveguides are more suited to particular applications than others depending on which criteria are the most critical – for example, dispersion is not a concern for continuous-wave applications – but efforts continue to find an optimum general purpose waveguide and to improve and expand the performance of the available designs.

Several waveguides proposed for terahertz frequencies are based on designs employed in the microwave regime such as the aforementioned hollow metallic tubes and transmission lines. Other proposals draw inspiration from the optical regime such as dielectric fibers [17], plastic photonic crystal fibers [18] and other photonic crystal waveguides [19-21]. The two waveguide designs that are considered in this thesis are the metal wire waveguide and the parallel-plate waveguide. These will be discussed in much greater detail in later Chapters but a brief overview is presented here.

The metal wire waveguide [22] was developed by a previous PhD student in our research group, Kanglin Wang, after observing the unintended propagation of THz signals along a metal probe used in an apertureless near-field microscopy

system [23]. The metal wire waveguide compares well with the waveguides listed above in many ways, particularly its very low loss and dispersion [24], but it is characterized by a weak coupling and large beam extent, which can lead to high bending loss. The research presented in this thesis, however, posits that this large beam extent also gives a high degree of flexibility in the coupling geometry and that the traditional formalism of bending loss is incomplete. Experimental data and simulation results are also presented to verify the possibility of subwavelength confinement of energy at the tip of a tapered metal wire waveguide, which is of great interest for near-field imaging applications. This work can be found in Chapter 2.

The second waveguide to be discussed is the TE-mode parallel-plate waveguide. The parallel-plate waveguide was a design inspired by microwave rectangular waveguides and represents another mathematically elegant and geometrically simple waveguide structure. Its low loss and low-dispersion are well-established [25], while the primary disadvantage – diffractive loss from the unconfined sides – has been challenged by recent results [26, 27]. Like the metal wire, it is already incorporated in many applications such as spectroscopy [28], sensing [29], imaging [27, 30], and superfocusing [26]. Of particular interest is the possibility of incorporating resonant structures into the waveguide for sensing and filtering applications. A single rectangular groove incorporated into a TE-mode parallel-plate waveguide has been demonstrated as a notch filter with a very narrow linewidth, and it has been implemented as a highly sensitive microfluidic sensor [1]. However, the origins of this resonance and the sensing mechanism are not well

understood. In Chapter 3 a detailed overview is presented of the theory and potential of TE-mode parallel-plate waveguides, along with an experimental and theoretical study of the origins of the resonance from the rectangular groove and its sensitivity to the refractive index of a dielectric filling. Also presented are an experimental and theoretical study of the possibilities when two grooves are incorporated in the waveguide, in both coupled and non-coupled geometries, and a demonstration of the effectiveness of these designs as multichannel or high-resolution single-channel microfluidic sensors.

1.2. Methods

With the importance of finding effective ways to guide and control terahertz radiation and the significance of the metal wire and parallel-plate waveguides established, we move on to a brief overview of the experimental and simulation techniques underlying the work presented in this thesis.

All of the experimental results presented in this work were obtained using a terahertz time-domain spectroscopy system. The basic design of this apparatus is presented in Section 1.2.1 below.

There are also several results from simulation presented in this thesis. The simulation software and methods are discussed in Section 1.2.2.

1.2.1. Terahertz Time-domain Spectroscopy

Time-domain spectroscopy is based on ultrafast laser pulses, which in this case are focused onto photoconductive switches to generate and detect the terahertz radiation. By varying the time-delay between the pulses, the entire terahertz waveform can be measured. By using linear photoconductive antennas, we can generate linearly-polarized terahertz pulses and, at the receiver, directly measure the component of the electric field aligned with the antenna axis. A diagram of a THz-TDS system is shown below in Figure 1-1.

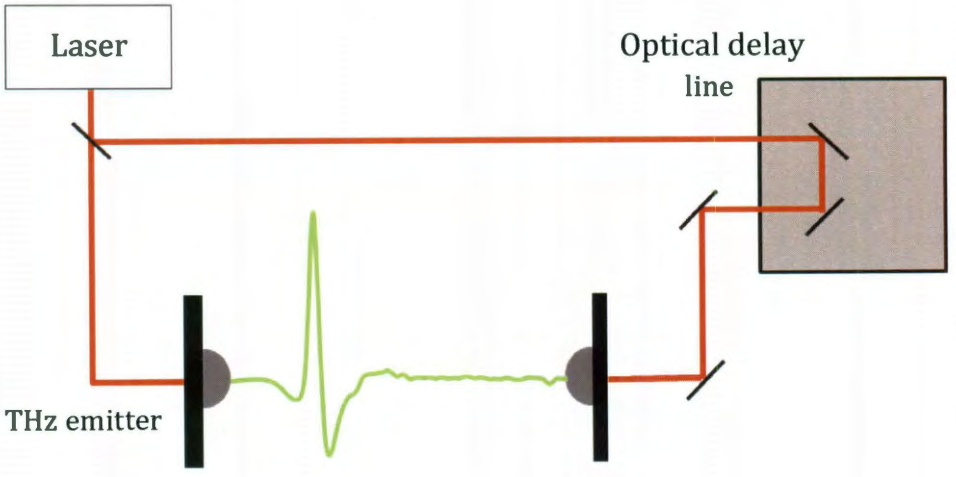

Figure 1-1 Typical terahertz time-domain spectroscopy experimental setup.

For coupling to a wire waveguide, linearly-polarized radiation is less effective than a radially-polarized input beam. So for experiments involving the wire waveguide, the linear antenna transmitter is replaced with a radially-symmetric antenna [31].

We can also fiber-couple the antennas, using fiber optics to direct the laser pulses to the antennas without the use of free-space optics. This allows us to freely position the transmitter and receiver, as well as to translate the receiver for imaging applications. A diagram of the fiber-coupled system is shown in Figure 1-2 below.

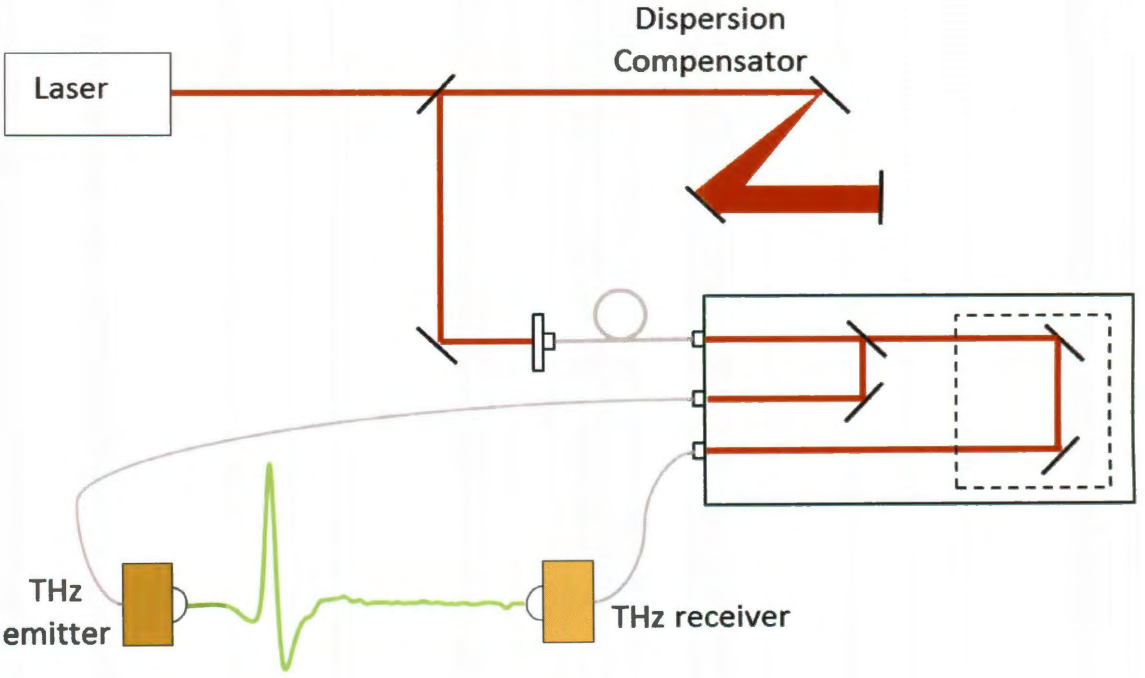

Figure 1-2 Diagram of the fiber-coupled THz-TDS system.

The experiments in the following Chapters are based on these two experimental setups or variations of them.

1.2.2. FEM simulation

The experiments in the following chapters are frequently supported by the results from finite element method (FEM) simulation. In finite element method simulation, the geometry to be simulated is divided up into smaller elements called the "mesh", and the relevant equations (in this case, Maxwell's equations) are evaluated for each of these smaller elements.

The results presented in this thesis were obtained using a commercial FEM simulation package, COMSOL. All simulations are two-dimensional, or three-dimensional with radial symmetry in the case of the wire waveguide simulations. The simulations are in the frequency domain, so all results presented are for one particular frequency only, in contrast to the time-domain experimental data. The size of the mesh elements must be at most $\lambda/3$ for reliable results, though it is possible to use smaller elements, even as small as $\lambda/50$ for the parallel-plate waveguide simulations. Because of the limitations of the computing power of our workstation, there is an upper limit to the number of elements that can be handled by the simulation, and so higher frequency simulations are increasingly difficult.

More details on the finite element method simulation techniques used in this thesis can be found in reference [32].

Chapter 2

Metal Wire Waveguides

Some of the results presented in this chapter have been previously published in references [33] and [34].

2.1. Introduction to the Metal Wire Waveguide

In the search for ever more versatile and efficient terahertz waveguides, the metal wire waveguide has drawn considerable attention due to its simplicity – a bare metal wire, easily obtained commercially – and its promising low-loss and low-dispersion characteristics [22]. The concept of transporting terahertz radiation via waves on bare wires has been the focus of a great deal of research [24, 35-37], including applications in spectroscopy [38, 39], subwavelength focusing [40], and near-field imaging [41-43]. However, despite the amount of interest, there are several key aspects of the wire waveguide's performance that have not been sufficiently studied, in particular the bending and coupling losses and the capability

for subwavelength confinement due to tapering. In this chapter experimental and computational studies will be presented that will help to clarify the capabilities and limitations of wire waveguides for future applications.

The concept behind the metal wire terahertz waveguide is the Sommerfeld wave, so called because in 1899 Sommerfeld gave the first mathematical description of propagation of a surface wave on a wire [44, 45]. Later, Gobau [45] and then King and Wiltse [46] continued the analysis, emphasizing the Sommerfeld wave's potential for practical application and calculating the transmission loss and radial extent of the field for a wide variety of waveguide radii at microwave and millimeter-wave frequencies.

The Sommerfeld wave is radially-polarized with a small axial component, propagating as a TM_0 transverse-magnetic mode on an infinite cylindrical wire of finite conductivity as illustrated in Figure 2-1.

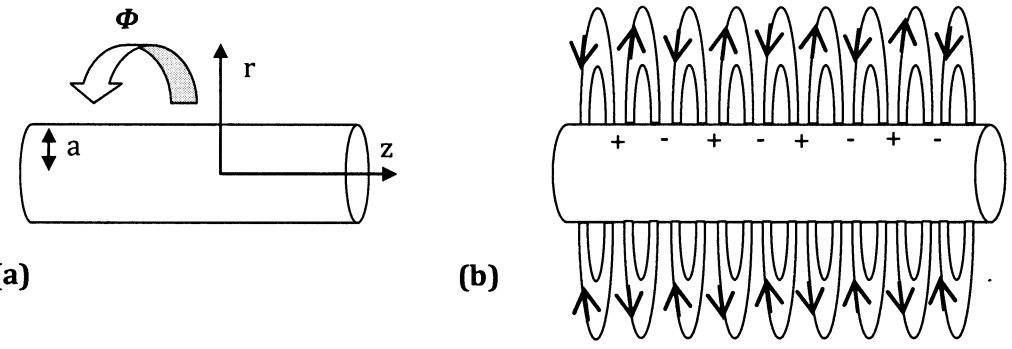

Figure 2-1 (a) Diagram of the wire waveguide and the coordinate system. (b) Illustration of the electric field of the TM_0 mode.

The field components of this TM_0 mode are given below:

$$E_r = jA\frac{h}{\gamma}Z_1(\gamma r)e^{j(\omega t - hz)} \quad \text{[2-1]}$$

$$E_z = AZ_0(\gamma r)e^{j(\omega t - hz)} \quad \text{[2-2]}$$

$$H_\Phi = jA\frac{k^2}{\omega\mu\gamma}Z_1(\gamma r)e^{j(\omega t - hz)} \quad \text{[2-3]}$$

where h is the propagation constant of the guided wave, identical inside and outside the wire. The functions Z_0 and Z_1 are replaced by the Bessel functions J_0 and J_1 inside the wire and the Hankel functions of the first kind $H_0^{(1)}$ and $H_1^{(1)}$ outside the wire. The parameter γ relates h and the free-space propagation constant k through the below relations, where the subscripts d and c refer to the value inside the dielectric (air) and the conductor (wire) respectively:

$$\gamma_d = {k_d}^2 - h^2 \quad \text{[2-4]}$$

$$\gamma_c = {k_c}^2 - h^2 \quad \text{[2-5]}$$

and where $k = (\varepsilon\mu)^{1/2}$, using values for permittivity and permeability of the relevant materials.

At the surface of the conductor ($r=a$), E_z and H_Φ are continuous, thus Equations [2-2] and [2-3] can be combined to one transcendental equation:

$$\frac{{k_d}^2}{\mu_d \gamma_d} \frac{H_1^{(1)}(\gamma_d a)}{H_0^{(1)}(\gamma_d a)} = \frac{{k_c}^2}{\mu_c \gamma_c} \frac{J_1(\gamma_c a)}{J_0(\gamma_c a)} \qquad \textbf{[2-6]}$$

This equation has been solved in the past using a variety of approximations based on assumptions such as a frequency-independent conductivity or a radius that is large compared to skin depth but not too large compared to wavelength [45, 46]. Due to astronomical increases in computing power over the last 50 years, most of these approximations are unnecessary and the equation can be solved numerically with only the assumption of a large radius relative to skin depth, $|\gamma_c a| \gg 1$, which is reasonable at terahertz frequencies [47].

By solving Equation [2-6], we can obtain the propagation constant h (and correspondingly the parameter γ) and from it the group velocity dispersion and the attenuation of the Sommerfeld wave. Since $\gamma << k$, the loss in cm^{-1} can be calculated from the imaginary part of the propagation constant h, given by the equation below where θ is the phase constant [46]:

$$\alpha = Im(h) = \frac{|\gamma a|^2}{2ka^2} sin2\theta \qquad \textbf{[2-7]}$$

We can solve Equation [2-6] for wire waveguides with a wide range of diameters and a wide range of materials, as long as $|\gamma_c a| \gg 1$ remains true, and so we can develop a picture of how the attenuation is dependent on radius, material

and frequency. For example, Figure 2-2 below plots the attenuation versus frequency for aluminum wire waveguides with radii from 150 μm to 1.5 mm.

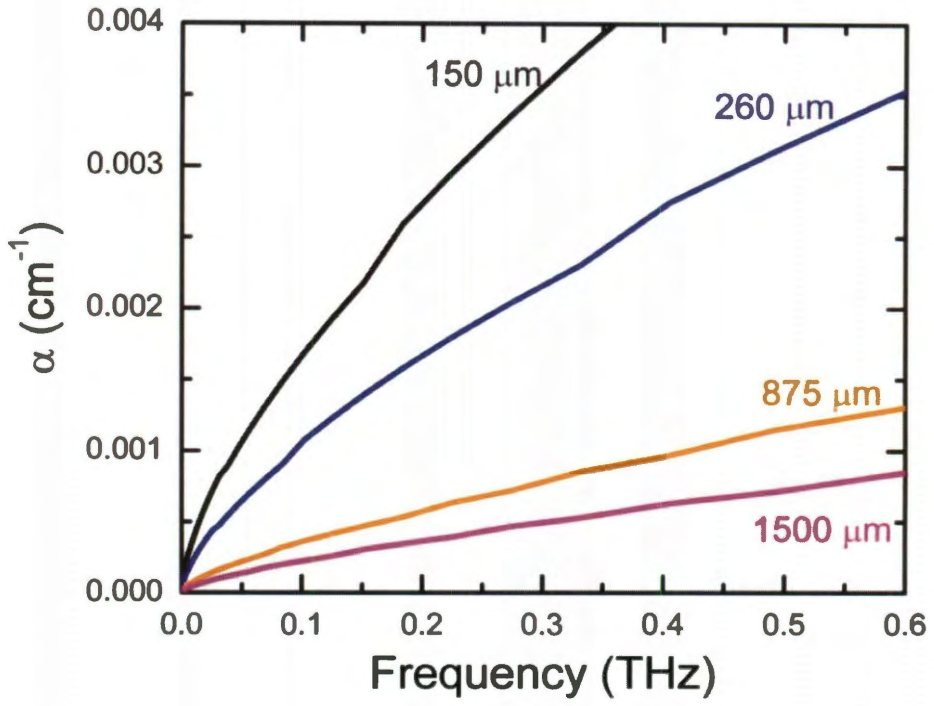

Figure 2-2 Plot of the attenuation α in cm^{-1} versus frequency for aluminimum wire waveguides with radius (listed top to bottom) 150 μm (black), 260 μm (blue), 875 μm (orange), and 1.5 mm (magenta).

Two trends are immediately clear from the above plot: (1) attenuation increases with increasing frequency, and (2) thicker wires exhibit less attenuation than thinner wires. This reflects the fact that at smaller diameters, more power is transmitted inside the skin depth of the metal [37, 47].

The attenuation is also dependent on the properties of the metal, particularly the permittivity. While not ideal at terahertz frequencies, the Drude model can be used to model the frequency-dependent permittivity of a metal, based on its plasma

frequency and electron collision rate (obtained from Ref. [48]). Figure 2-3 below plots the attenuation versus frequency for aluminum, copper, gold, tin, and iron waveguides with a radius of 875 μm.

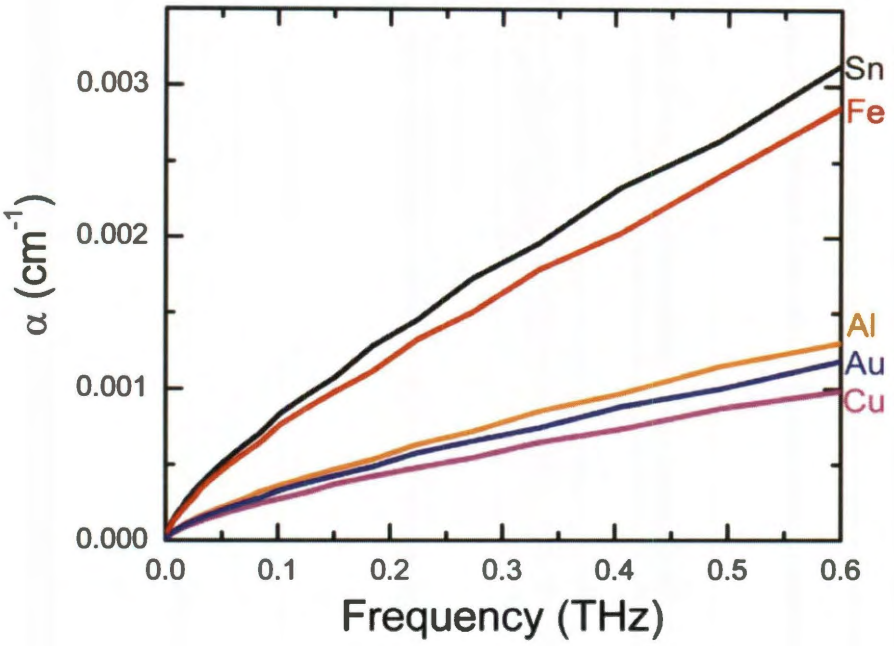

Figure 2-3 Plot of the attenuation α in cm^{-1} versus frequency for waveguides with a radius of 875 μm composed of (top to bottom) tin (black), iron (red), aluminum (orange), gold (blue), and copper (magenta).

From this plot there appears to be a general relationship between attenuation and conductivity, with higher attenuation for materials with lower conductivity.

From the solution to Equation [2-6] we can also measure the power transmitted outside a given radius ρ around the wire, N_ρ.

$$N_\rho = Re\left[2\pi \int_\rho^\infty r E_r H_\Phi{}^* dr\right] \quad \textbf{[2-8]}$$

The percentage of the power flow outside the area ρ around the wire is given by the ratio of N_ρ/N, where N is the total power flow around the wire ($\rho = a$).

$$\frac{N_\rho}{N} = \frac{Re\left[2\pi \int_\rho^\infty r E_r H_\Phi{}^* dr\right]}{Re\left[2\pi \int_a^\infty r E_r H_\Phi{}^* dr\right]} \quad \textbf{[2-9]}$$

$$= Re\left[\frac{\gamma^* \rho H_1^{(1)}(\gamma\rho) H_0^{(1)}(\gamma\rho)^* - \gamma\rho H_1^{(1)}(\gamma\rho)^* H_0^{(1)}(\gamma\rho)^*}{\gamma^* a H_1^{(1)}(\gamma a) H_0^{(1)}(\gamma a)^* - \gamma a H_1^{(1)}(\gamma a)^* H_0^{(1)}(\gamma a)^*}\right]$$

This equation can be used to calculate the beam extent, the radius within which 75% or 90% of the energy flow is contained. The beam extent is dependent on the frequency as well as the radius of the wire, and at terahertz frequencies and typical radii the beam extent is quite large -- for example, from King and Wiltse's calculations, at a frequency of 100 GHz a wire with a diameter of 2 mm carries 75% of its transmitted power within a radius of 2.5 cm. Larger wires have a larger beam extent (for comparison, a 2 cm diameter wire carries 75% of its power within a 10-cm radius), and higher frequencies have a smaller beam extent [46]. At low frequencies, the field may extend tens of centimeters away from the waveguide.

This large beam extent has several consequences for potential applications of the metal wire waveguide at millimeter-wave and terahertz frequencies. Large beam extent is indicative of a weak plasmon-based coupling mechanism, and weak coupling limits the effectiveness of a waveguide – for example, weakly-coupled waves have much higher bending losses than strongly coupled waves. As a result, the conventional wisdom of wire waveguides states that bends should be avoided where possible, or if a bend cannot be avoided it should be made as slow and gradual as possible in order to minimize loss, which is a distinct disadvantage in real-world waveguide applications [24, 35, 45, 49].

A large beam extent also makes the waveguide more sensitive to its surroundings, requiring a much larger unobstructed beam path and requiring more carefully-designed support structures to hold and direct the waveguide. A fiber optic cable, with its beam confined to within the core, can be strung in pipes, along walls, or underground, and it can placed side by side with other cables without interference, while all of these scenarios are problematic for the large beam of the wire waveguide.

This is not solely a disadvantage, however. The large beam extent can be a tremendous advantage for coupling, because coupling can be efficient with less rigorous alignment and with a wider range of geometries. The high bending loss may be overcome through the use of dielectric coatings to more tightly bind the wave [45] or the use of a mirror [49] to avoid a bend entirely. The conventional wisdom in favor of slow gradual bends also overlooks the increased ohmic losses of

long curves. Section 2.2 explores the bending and coupling loss of a wire waveguide in detail.

Also, the relationship between beam extent and wire diameter has excellent potential for imaging applications, in particular for tapered waveguides. A waveguide may have a larger initial diameter to optimize coupling, but if it is tapered to a point the beam extent will decrease along with the waveguide diameter, creating the possibility for excellent subwavelength confinement [40, 50]. This possibility is discussed through simulation and experiment in Section 2.3.

2.2. Bending and Coupling Losses

The characterization of the bending and coupling losses of the wire waveguide is primarily an experimental study. The waveguide is considered in situ, in its experimental framework, to obtain a reliable estimation of its loss behavior for real-world applications.

The experimental study was conducted using the THz time-domain spectroscopy setup described in Section 1.2.1, in which a free-space ultrafast laser pulse is focused onto a radial photoconductive antenna, with the resulting radiation detected using a fiber-coupled photoconductive receiver that is part of the commercial T-Ray system. In the experiments, a 12-cm-long section of 1.75 mm diameter stainless steel wire is placed against the antenna and aligned to obtain maximum coupling (see Figure 2-4 below). This waveguide remains in place during

subsequent experiments to ensure consistent coupling from the antenna, while additional straight and curved waveguide sections are incorporated in varying geometries for the characterization of the coupling between waveguides.

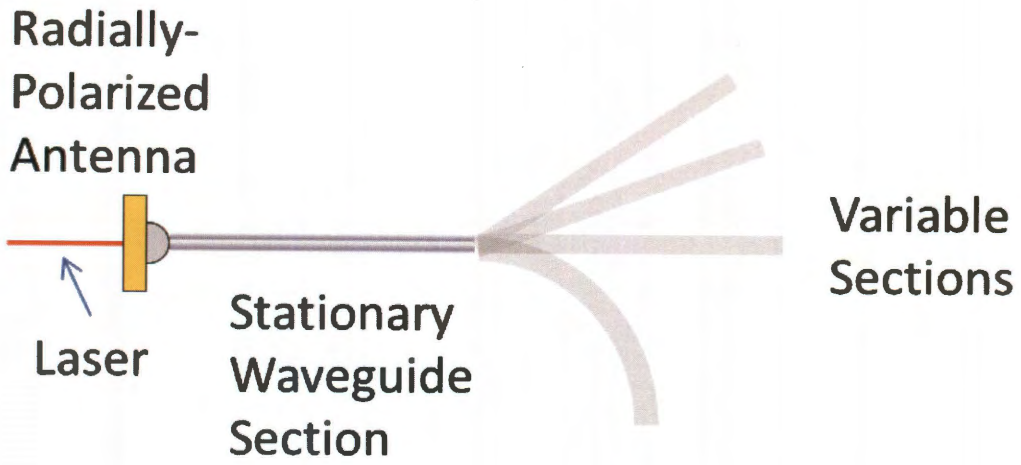

Figure 2-4 Diagram of the basic setup for the following experiments. A stationary waveguide section is placed for maximum coupling to a radially-polarized antenna. Additional sections are end-coupled to this stationary waveguide section to conduct experiments with gaps, angles, curves, etc.

First, the propagation on the original 12 cm waveguide section is characterized, to ensure that the coupled radiation is a single-mode Sommerfeld wave. This is done by measuring the time-domain waveform with the receiver displaced a few centimeters laterally to both the left and right of the end of the waveguide (see the diagram of receiver positions in Figure 2-6). For a radially polarized Sommerfeld wave, the electric field direction in a linear sense is reversed on opposing sides of the waveguide (Figure 2-5 (a)). As a result, there should be a polarity flip in the electric field measured on opposite sides of the waveguide. If the

wave did not couple, we would be detecting the free space propagation which would exhibit no polarity flip. In Figure 2-5 (b) below, there is a clear polarity flip visible in the waveforms, which are otherwise nearly identical as expected for measurements at the same radial displacement. There is a slight asymmetry in the waveform shape, which is most likely due to a small asymmetry in the receiver positions (one position may have been slightly closer or further from the waveguide than the other in either the radial or axial direction).

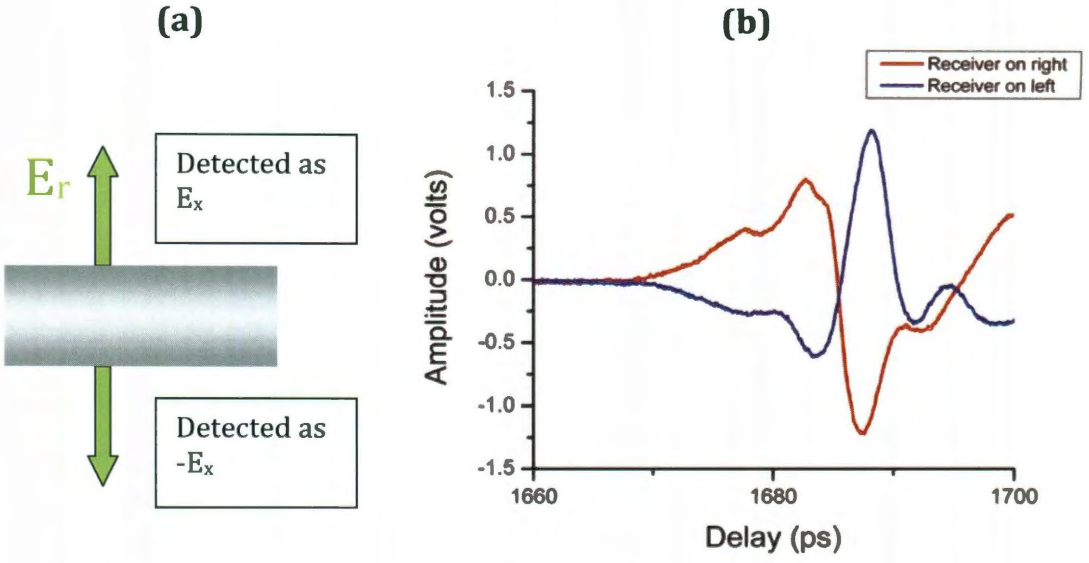

Figure 2-5 (a) Diagram of the radially-polarized electric field on the waveguide, illustrating the polarity flip when the field is measured on opposite sides of the waveguide. (b)Time-domain waveforms measured at the end of the single 12 cm waveguide, with the receiver displaced a few centimeters to the right (red curve) and left (blue curve) of the waveguide. There is a clear polarity flip, indicating a radially-polarized mode is propagating on the waveguide.

These results support the Sommerfeld wave nature of the mode propagating on the single wire waveguide. With the wave propagation established, we move on

to exploring the efficiency with which radiation can couple from the end of one wire, across an air gap, onto the end of a second parallel wire situated on axis with the first. We start with the 12-cm long stainless steel wire aligned to couple radiation from the radial antenna as before. The second 12-cm wire is translated along a line parallel to the axis of both wires, so a gap of varying width can be created between the two wires (Figure 2-6 below). This permits us to explore the frequency-dependent diffraction that occurs in the air gap [51] and is similar to earlier work on surface plasmon coupling across a gap between two flat metal surfaces [52].

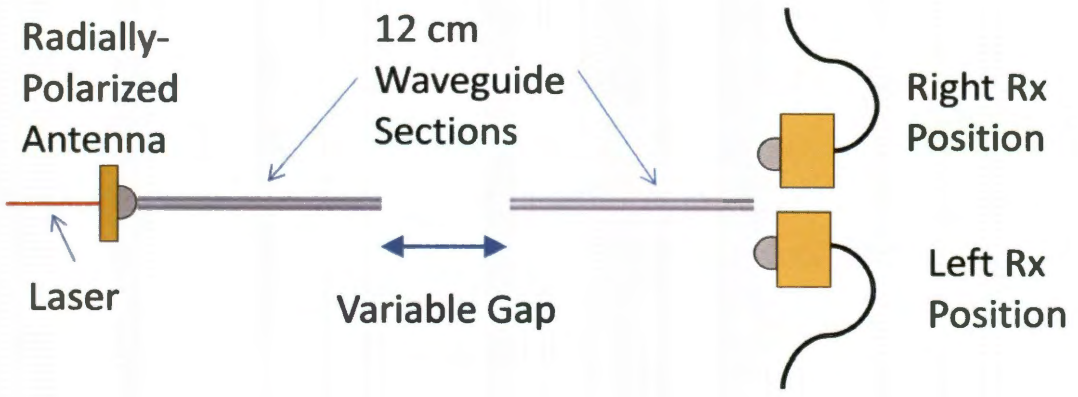

Figure 2-6 Diagram of the experimental setup. As the gap between waveguide sections is increased, the receiver is moved back a corresponding distance and measurements are taken at the left and right receiver positions indicated in the schematic.

The receiver is translated along with the second wire and the time-domain THz waveform is measured at the end of this wire with the receiver in two locations on opposite sides of the wire – this allows us to check the symmetry of the mode on the waveguide. A decline in mode symmetry would indicate a breakdown of effective coupling. Figure 2-7 below shows the peak-to-peak amplitude of the time-

domain waveforms as a function of the gap distance. Signals from both sides of the waveguide are plotted on the same scale, ignoring the polarity flip, in order to demonstrate the mode symmetry. From this figure, it is evident that the coupling across the gap decreases with increasing gap size.

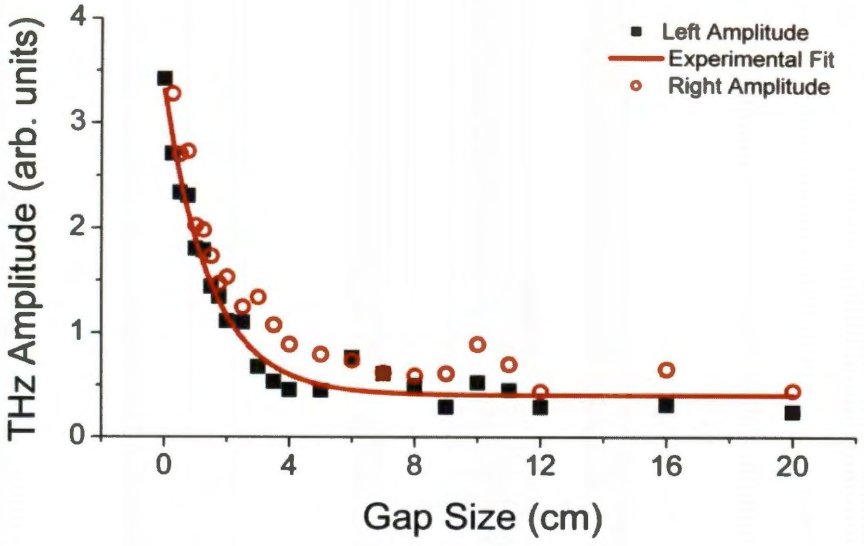

Figure 2-7 Peak-to-peak terahertz field amplitude for increasing gap between the two waveguide sections. Filled black squares and open red circles represent measurements on opposite sides of the waveguide to illustrate the symmetry of the mode. The red line is an exponential fit of the amplitude measured on the left side of the waveguide.

Previous simulation and experimental work has shown that the diffraction at the end of a wire waveguide is strongly frequency dependent [51]. This implies that the coupling across a gap would also be frequency-dependent. To investigate this, the time-domain waveforms were Fourier transformed into the frequency domain. To improve the quality of the amplitude spectra, the waveforms were windowed and corrected for DC-offset before the Fourier transform was applied. Figure 2-8

below shows the amplitude spectra for gaps of 0 cm and 12 cm. This illustrates that, even for large gaps on the order of the waveguide length, the spectral bandwidth is almost unaffected despite the overall decrease in signal strength.

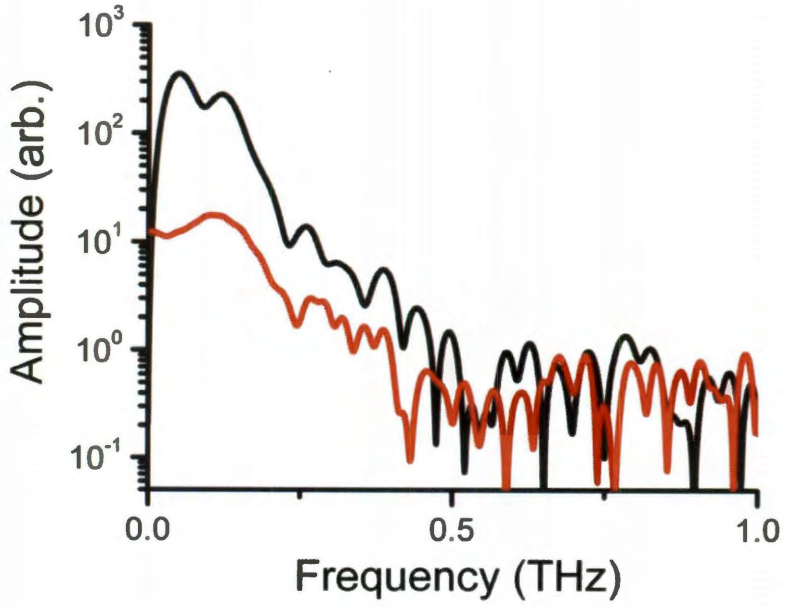

Figure 2-8 Amplitude spectra for 0 cm (black curve) and 12 cm (red curve) gap sizes. This illustrates that the signal decreases when a gap is inserted, but the bandwidth is essentially unchanged.

We can further examine the frequency dependence of the coupling by considering the dependence of the signal strength on gap size for a few selected spectral components (Figure 2-9). This plot shows that the initial decrease of signal with increasing gap size is independent of frequency, but at larger gaps a clear dependence emerges as higher frequencies re-couple more efficiently onto the second wire. This is consistent with the fact that higher frequencies diffract less strongly than lower frequencies [51].

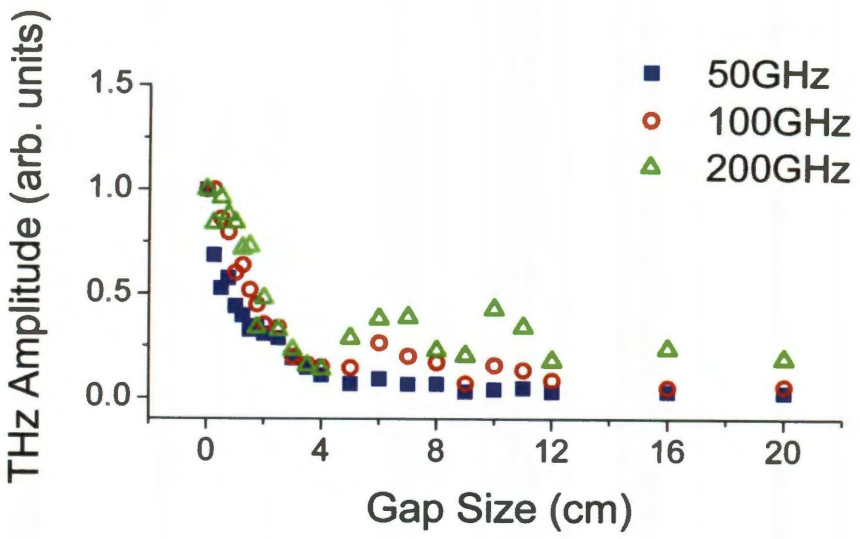

Figure 2-9 Relative dependence of signal strength on gap size, for a few selected spectral components. Higher frequencies diffract less strongly at the end of the first wire, and therefore couple across the gap more efficiently. All components are normalized based on their value at the 0 cm gap.

For gaps of this size, it is possible to insert a Teflon lens into the gap to improve the coupling between the two waveguide sections. Figure 2-10 below illustrates the effect on the THz time-domain waveforms when a lens with a focal length of 6 cm is inserted into the 12 cm gap, clearly demonstrating the increase in coupling efficiency (from 17% to 79% of peak-to-peak amplitude). The flip in polarity between Figure 2-10 (a) and (c) due to the insertion of the lens is a result of the 180° Gouy phase shift that occurs when a Gaussian beam is focused [53].

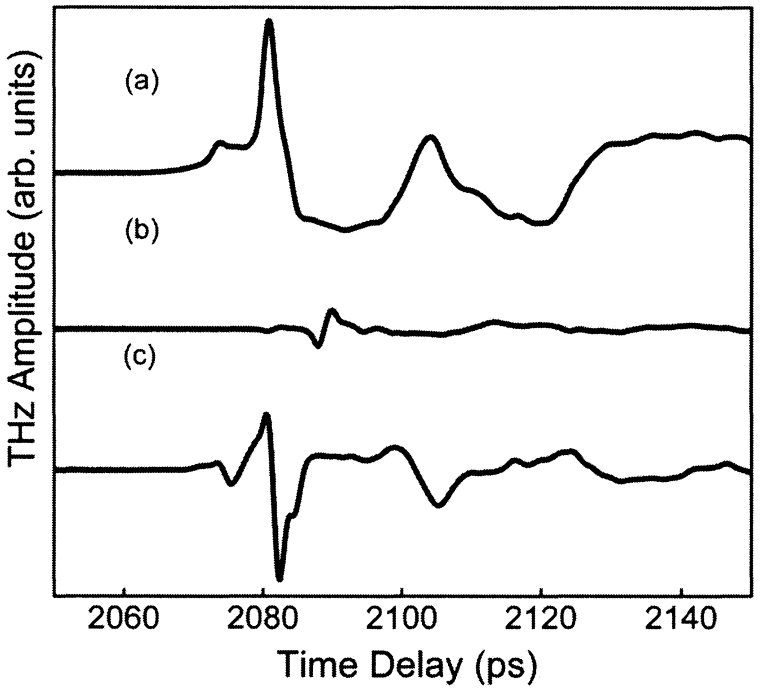

Figure 2-10 Time domain terahertz waveforms (a) with no gap between waveguide sections, (b) with a 12 cm gap between sections, and (c) with a lens of focal length 6 cm placed in the gap. Signal amplitude with the lens is 79% of the initial amplitude with no gap between sections.

In addition to the coupling between two wires with aligned axes, we also investigated coupling between wires whose axes are not aligned, and determined the dependence of wire-to-wire coupling on the angle between the axes. We maintain an end-to-end coupling distance of zero, but vary the angle of the second wire axis relative to the axis of the first. The location of the receiver remains fixed relative to the second wire as it is rotated. As seen in Figure 2-11 below, significant signal remains even at angles as great as 30°, while angular offsets less than 10° retain the majority of the signal strength. These results imply that a small error in

the angular axial alignment between the waveguide sections can be tolerated in real-world coupling applications.

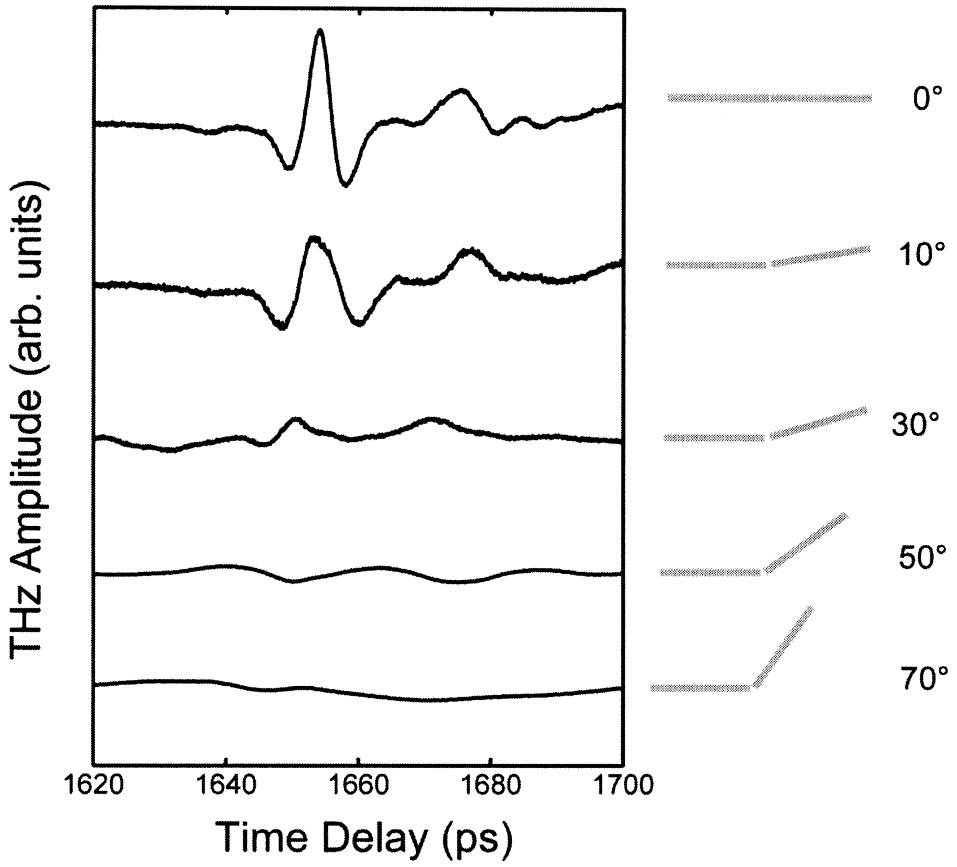

Figure 2-11 Time-domain terahertz waveforms for a series of waveguide configurations at increasing angular offset, as illustrated in the schematics to the right. Significant signal remains until approximately 30° of angular displacement.

As noted previously in Section 2.1, a disadvantage of the wire waveguide is that the Sommerfeld wave is only weakly guided, leading to high bending losses when the wave is curved [24, 35, 45]. It has been suggested in previous work that

these bending losses can be avoided by the use of a mirror with these angled configurations of straight sections [49]. As observed above, a high angular offset between the two waveguide sections results in a greatly decreased signal. At an offset of 90°, with the two waveguide sections aligned perpendicular to one another, there is essentially zero detected signal (Figure 2-12 (b)). With a polished aluminum mirror of 5 cm diameter placed at the junction of the two waveguides, at a 45° angle to both wires (see schematic in Figure 2-12 (c)), the signal amplitude drops to only 75% of the amplitude for the 0° offset waveguides.

The mirror has the effect of diverting (reflecting) the radiation at the output of the first waveguide onto the input of the second to allow the two sections to essentially act as a continuous wire. This reflection is the cause of the polarity flip observed in the waveforms above. The small decrease in signal amplitude is most likely due to the size of the mirror, which was smaller than the predicted beam extent. The transmission could be further improved by using a larger mirror, or by angling or faceting the waveguide faces to lie flush with the mirror surface.

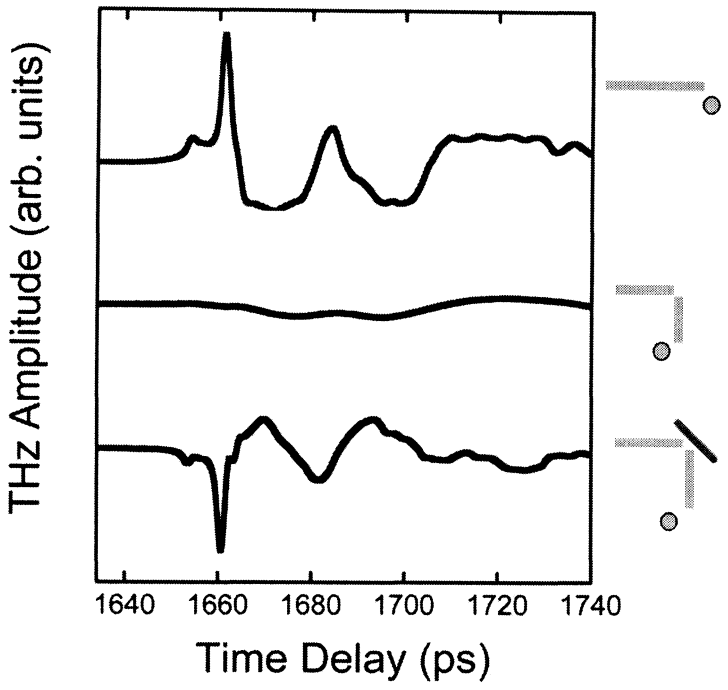

Figure 2-12 Time-domain terahertz waveforms for (a) a straight waveguide, (b) two waveguide sections in a perpendicular arrangement, and (c) perpendicular waveguides with the addition of a turning mirror. The gray circle in the schematic indicates the receiver position. The amplitude of the signal in (c) is 75% of the amplitude in (a).

To compare the high transmission from this mirror geometry to that of a curved wire, we apply the theory of radiative bend loss to a circular wire arc with an angle of 90° and a radius of curvature R. An abrupt right-angle turn such as the one considered above (Figure 2-12 (b), without the corner mirror), may be taken as the limiting case of this situation with a radius of curvature $R=0$. The total amplitude attenuation α_T of a wave at frequency f travelling along a curved waveguide includes contributions from both the radiative bend loss, which increases exponentially with decreasing radius R (see Equation [2-10]) [24, 54], and the intrinsic attenuation α of

the Sommerfeld wave as discussed in Section 2.1, which is constant (independent of R) for a given arc length z.

$$\alpha_{bend} = c_1 e^{-c_2 R} \quad \textbf{[2-10]}$$

$$\alpha_T = \alpha_{bend} + \alpha = c_1 e^{-c_2 R} + \alpha \quad \textbf{[2-11]}$$

For a curved waveguide with an arc of angle θ, radius R, and total length $z=R\theta$, the amplitude transmission is given by the below equation:

$$t = e^{-\alpha_T z} = e^{-R\theta\left(c_1 e^{-c_2 R}+\alpha\right)} \quad \textbf{[2-12]}$$

For reasonable values of the parameters c_1, c_2, and α, this is a monotonically decreasing function with increasing radius R (see Figure 2-13). The decreasing bend loss is counteracted by the increasing propagation loss with the larger propagation distances required to turn 90° at larger values of R.

However, this result is obviously nonphysical for very small values of R, for which the transmission should diminish rapidly (as shown by Figure 2-12 (b)). This difficulty arises from the assumption of an exponential bend loss, which is only valid for $R > \Delta$, where Δ is the transverse spatial extent of the propagating mode [54]. The value of Δ depends on the frequency and waveguide diameter, among other parameters, and in our experiments Δ is on the order of a few centimeters.

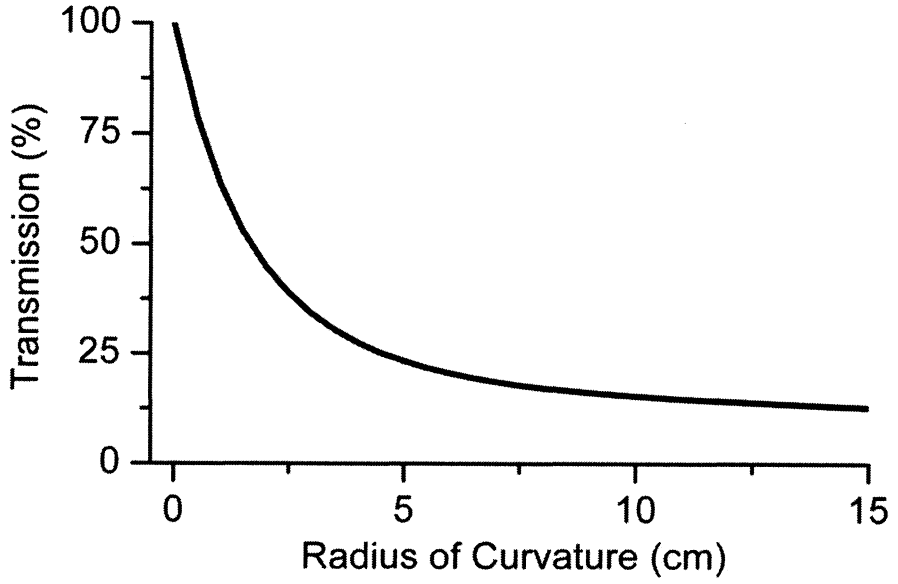

Figure 2-13 An example illustration of the transmission predicted by Equation [2-12]. This shows monotonic behavior as a function of *R*, which is inconsistent with the fact that the transmission must vanish as $R \to 0$. Values for c_1, c_2, and α are obtained from experiment as described below.

The exponential loss formula is based on the assumption that spatial overlap between propagating modes on the straight waveguide section and along the curve is significant. For smaller values of R in which the turn is very sharp relative to the spatial extent of the mode Δ, there is likely to be little spatial overlap between the propagating modes of the straight and curved sections and therefore a reduced coupling around the curve, implying a departure from this exponential form. Indeed, since the transmission must vanish for both $R \to 0$ and $R \to \infty$, it is clear that there is a point of maximum transmission: an optimum value for R at which the total loss for traversing a 90° bend is minimized.

In order to include this effect in our transmission equation, we modify Equation [2-12] to include the spatial scale Δ which must be relevant at small R.

$$t = e^{-R\theta\left(c_1 e^{-c_2 R}+\alpha\right)}\left(1 - e^{-\frac{R}{\Delta}}\right) \qquad \textbf{[2-13]}$$

This additional factor forces the transmission to zero for $R = 0$, and thus guarantees a physically reasonable result (Figure 2-14).

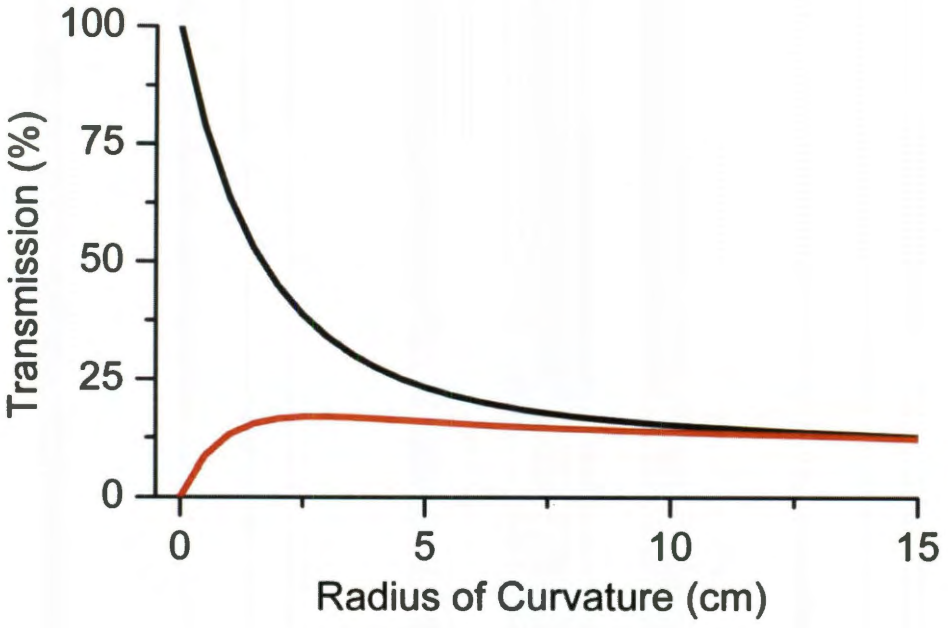

Figure 2-14 An example illustration of the transmission with (red) and without (black) the added spatial factor. When the spatial factor is added, the transmission vanishes as $R \rightarrow 0$. The value for Δ is based on the fit to experimental results as described below.

To confirm this result experimentally, we fabricated several curved waveguides of varying radii, each with a 90° turn angle [1]. By inserting these curved waveguides between two straight waveguide sections and maintaining a constant receiver position relative to the end of the second straight section, we can determine the transmission for various radii of curvature for a fixed turn angle of 90° (see schematic in Figure 2-15 below).

For each curved waveguide section, we calculated the transmission by comparing the peak amplitude of the measured time-domain waveform of the entire waveguide (two straight sections bracketing one curved section) to that of the peak amplitude from the straight waveguide sections alone.

---

[1] Notes for experimental implementation: we created these curves by bending straight stainless steel wire sections against a variety of cylindrical objects. It is important to keep the wire level during bending to ensure the bend is only in two dimensions. The curved waveguide is then compared to a right-angle marker such as a T-square and cut to generate a 90° arc. The ends of the waveguide are then carefully filed to ensure they are perpendicular to the waveguide axis, which is necessary for good and consistent coupling with the straight waveguide sections. It is very easy to have a slightly offset end facet in some waveguides, leading to inconsistent coupling that greatly affects the measured transmission. If the two straight sections are placed at 90° angle with respect to each other, the curved waveguide can be trimmed and filed off to fit in between, to obtain a 90° arc with appropriately angled end facets.

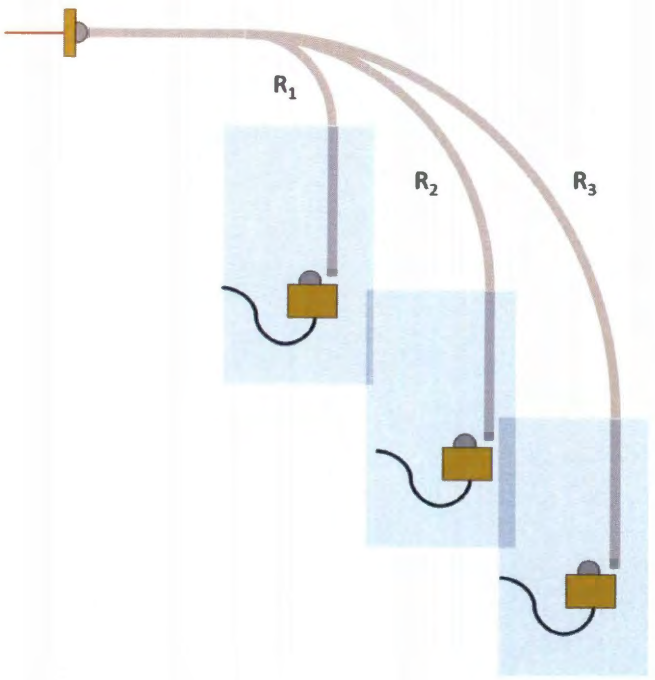

Figure 2-15 Schematic of the setup for the curved waveguide transmission experiment. The initial straight waveguide section is stationary. An additional waveguide section is stationary relative to the receiver; both the receiver and straight waveguide are freely translated (blue squares represent the movable apparatus). Between the two straight sections, a series of curved waveguides of varying radii (R_1, R_2, R_3 shown) are inserted to give a 90° turn angle.

In Figure 2-16 below we plot the measured transmission versus the radius of curvature of the curved waveguide section. We observe a clear peak in the transmission at a radius of curvature of approximately 3 cm, on the same order as the spatial extent Δ. For smaller radii, the transmission decreases rapidly due to the bending loss, whereas for larger radii the transmission is increasingly dominated by the intrinsic propagation loss. The maximum amplitude transmission is approximately 20%, significantly smaller than the value obtained with a corner mirror, but potentially large enough for many applications in which a mirror is not practical, such as an endoscope [22].

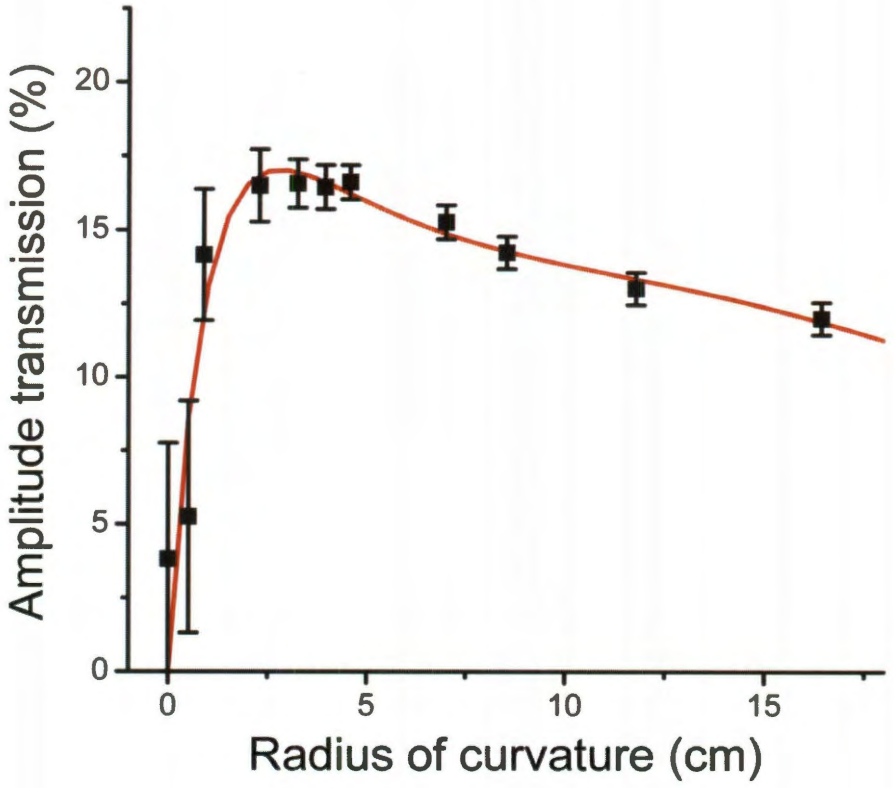

Figure 2-16 Amplitude transmission after propagation along a curved waveguide section of radius *R* and turn angle of 90°. Error bars are based on the difference between multiple data sets. The decrease at small radii results from bending loss, whereas the behavior at large radii is dictated by intrinsic propagation loss. The solid curve is a fit to the data using Equation [2-13] which includes the mode size parameter Δ. The parameters derived from this fit are c_1 = .264, c_2 = .145, α =.028, and Δ= 4.34. These are the same parameters used to generate Figure 2-13 and Figure 2-14.

The solid line in the above figure is a fit using Equation [2-13], giving a Δ value of approximately 4 cm and an intrinsic propagation loss α of .03 cm^{-1}. Since the data are extracted from time-domain waveforms, these values are spectrally weighted averages. This loss is large compared to the prediction for an iron wire obtained previously in Section 2.1, Figure 2-3, which ranged from 0 to .003 cm^{-1} over the bandwidth of this system. However, it is consistent with some previous

experimental measurements [24]. In our case, it is possible that the increased loss may come from interactions of the large beam with the apparatus used to support the waveguides or from the addition of extra Teflon pieces to hold the curved waveguide sections, which would lead to an artificially high measurement of the intrinsic attenuation α.

These results have many implications for any eventual applications of the wire waveguide, particularly for its bending and coupling losses in a variety of geometric configurations. Through these results, we clarify the dependence of the bending loss on the radius of curvature, emphasizing the significant role of the spatial extent of the mode, invalidating the conventional formalism for small radii, and correcting a longstanding misconception about the desirability of slow gradual bends. We also establish the flexibility of this waveguide with respect to coupling and alignment errors and present a mirrored geometry as a high-transmission alternative to a curved waveguide.

2.3. Tapered Wire Waveguide

One of the potential applications for the wire waveguide is in superfocusing of radiation for near-field imaging applications. Superfocusing – light focused to spot sizes significantly lower than the traditional diffraction limit – with the use of waveguides is a lively area of research interest, because it is a technique for confining electromagnetic radiation that does not necessarily suffer from the high

loss and dispersion of aperture-based techniques or the low image contrast of apertureless techniques.

A variety of surface-plasmon waveguides have been used for superfocusing applications, such as a coaxial conical horn microwave antenna [55], metal nanoparticle chains [56], metal or metal-coated wedges [57], metal nanowires [58], waveguides with gap plasmons [59], metal-coated optical fiber tips [60], and tapered metal stripes [61]. For wire waveguides, both corrugations [62] and dielectric coatings [45] have been proposed to achieve confinement. Of particular relevance to this thesis are tapered metallic wires [50, 63, 64], in which a metal wire guides a surface plasmon to a tapered conical tip. The size of the propagating wave tapers along with the waveguide diameter, resulting in subwavelength confinement of electromagnetic energy at the tip.

This geometry has been investigated primarily in the visible wavelength regime, which requires nanoscale wires. Simulations at the nanoscale predict an intensity increase of three orders of magnitude at the end of the tip [50] though the enhancement is dependent on factors such as the wavelength, the taper angle, the waveguide material, and the tip radius [65].

In the terahertz region of the spectrum, tapered wire waveguides have been investigated through analytic theory [40] and numerical simulation [32, 62, 66], which both predict subwavelength confinement at the tip of the taper. We performed additional finite element method simulations to explore the confinement effects. A plot of the electric field propagating on an untapered wire is shown below.

The radial field, E_r, shows the Sommerfeld wave pattern during the propagation on the wire, along with the diffraction at the end (Figure 2-17). Previous simulations [51] and experiments (see Section 2.2) established the frequency dependence of this diffraction behavior. The longitudinal field, E_z, is very small during normal propagation, since Sommerfeld waves have only a small longitudinal component, but at the end of the waveguide E_z is greatly enhanced as a result of the diffraction of the propagating wave (Figure 2-18). This E_z component exhibits three-dimensional confinement, strongly concentrated at the end of the wire.

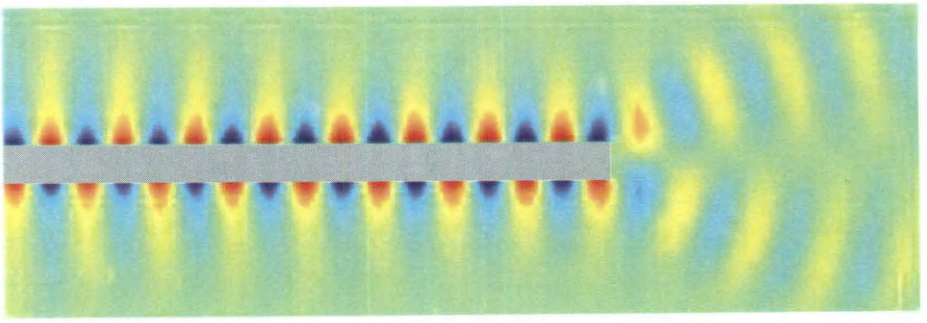

Figure 2-17 FEM simulation plot of the electric field E_x for a cross-section of a cylindrical waveguide with a diameter of 1.56mm. The propagating wave has a frequency of 100 GHz. The change in polarity on each side of the waveguide indicates the radial polarization. Diffraction is clearly visible at the end of the waveguide as the radiation couples into free space.

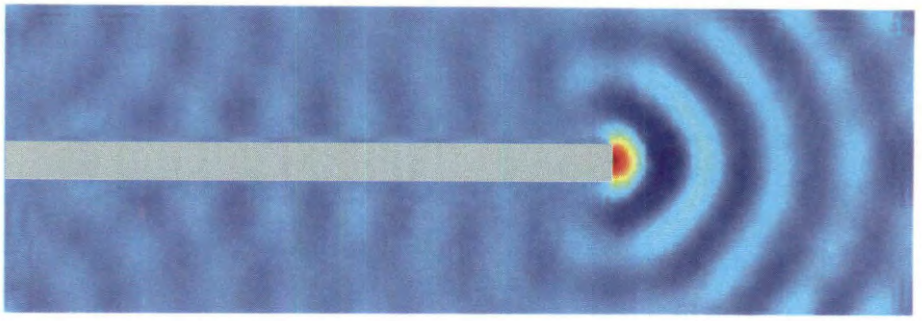

Figure 2-18 FEM simulation plot of the longitudinal electric field E_z for a cross-section of a waveguide with a diameter of 1.56 mm. The propagating wave has a frequency of 100 GHz. The longitudinal component is nearly zero during Sommerfeld mode propagation, but is enhanced and confined in three dimensions at the end of the waveguide.

These same properties can be observed for a tapered wire. The radial field shows the same Sommerfeld propagation pattern (Figure 2-19). As the wire tapers to a point, the field extent decreases along with it, resulting in confinement of the field at the tip before it diffracts out into free space (Figure 2-20).

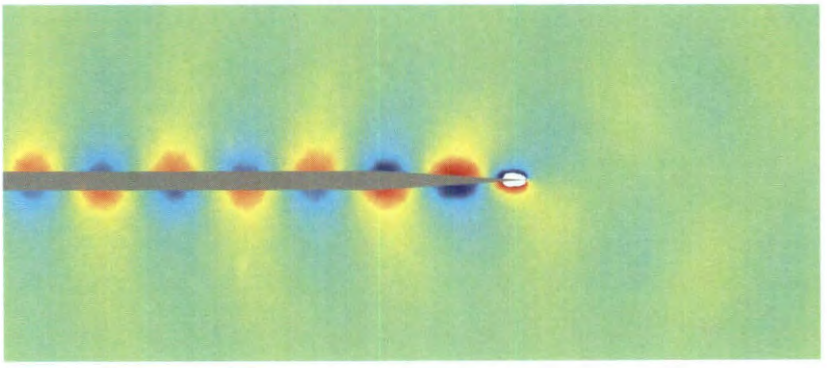

Figure 2-19 FEM simulation plot of the electric field E_x for a cross-section of a tapered waveguide. As the waveguide diameter tapers, the field tapers as well, resulting in a greatly enhanced field near the end of the taper. The scale on the figure has been saturated so that the wave is visible during propagation.

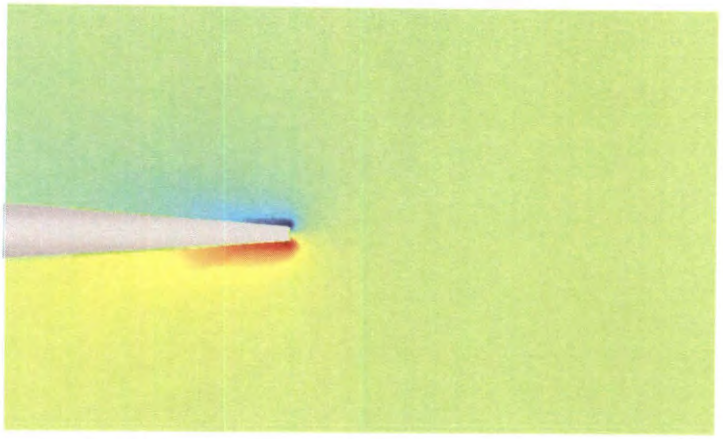

Figure 2-20 Expanded view of the electric field E_x at the end of the taper in Figure 2-19. The high degree of enhancement and confinement is clearly visible.

The longitudinal field component for a tapered wire is even more interesting, with a very strong three-dimensional confinement to the end of the waveguide.

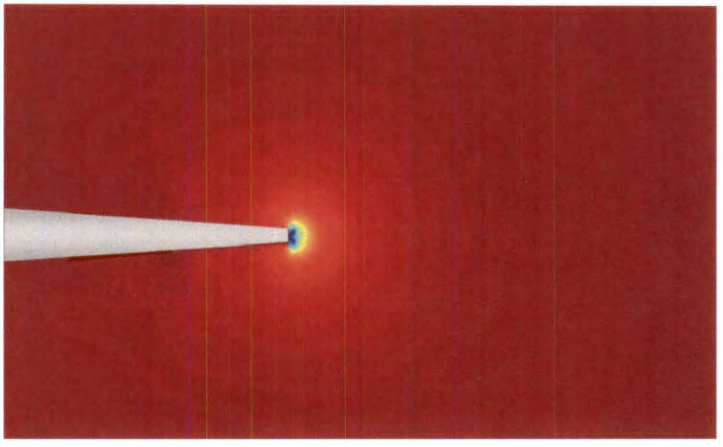

Figure 2-21 FEM simulation plot of the longitudinal E_z field at the end of the taper. The high degree of enhancement and three-dimensional confinement are clearly visible.

Experimental confirmation of this confinement has been limited, due to the difficulty of observing the confinement directly. Existing techniques for measuring

the output of a waveguide do not have sufficient resolution, while most near-field techniques are not applicable to this kind of free-space measurement. Initial results have been obtained based on a variety of indirect techniques such as the use of a taper to couple terahertz radiation from the antenna to the waveguide [66] or the use of a metal tip to concentrate and distort free-space terahertz radiation [67]. These results support the predictions of field enhancement in the region of the tip, but provide no direct measurement of the confinement itself. Based on these previous experiments, tapered wires have begun to be implemented for terahertz near-field imaging and spectroscopy, with promising results [41, 43, 68].

However, despite these applications, there has been no direct experimental study of the efficacy of confining a guided terahertz surface (Sommerfeld) wave using a tapered wire. Without such direct observation, the implementation of tapered waveguides as near-field probes or to generate high-intensity localized terahertz plasmons is shaped by the assumed accuracy of simulations that have not been compared to experimental data. In this work, we use a technique I developed in my previous work (see Ref. [69] and [70]) called scattering-probe imaging, which is uniquely capable of directly measuring the extent of the electric field at the tip of the tapered waveguide and providing a quantitative experimental result to compare to the predictions of simulation and theory.

Scattering-probe imaging is described in detail in my master's thesis (Ref. [70]), but the concept can be described briefly here. We use a sharp metal probe tip, similar to those used in apertureless near-field microscopy (ANSOM) [68, 71], to

sample the electric field in the immediate vicinity of the tip. The tip of the probe acts as an antenna, and it is excited by the component of the incident electric field polarized parallel to the probe axis. The antenna then re-radiates this signal which is detected in the far-field, with a resolution limited by the tip size. This technique is similar to other apertureless near-field microscopy techniques in that it does not suffer from the cutoff effects and limited resolution of aperture probes [72], with the added advantage that it does not require a substrate to form the image charges, as is necessary in traditional probe-based ANSOM [72, 73].

The experimental setup for the measurement of electric field confinement is based on that for the waveguide coupling experiments in Section 2.2 above and uses the photoconductive fiber-coupled THz TDS system described in the Methods Section 1.2.1. A stainless steel cylindrical wire is coupled to the radially-polarized photoconductive antenna. This waveguide may have a tapered (Figure 2-22 (b)) or untapered (Figure 2-22 (a)) end facet. A tungsten scattering probe with a tip diameter of 20 μm is placed with its tip at the end of the waveguide and its axis aligned along the direction of propagation (the *z* axis). In this configuration, the scattering probe is sensitive to the E_z component of the electric field, so the full 3D confinement of the axial field can be measured.

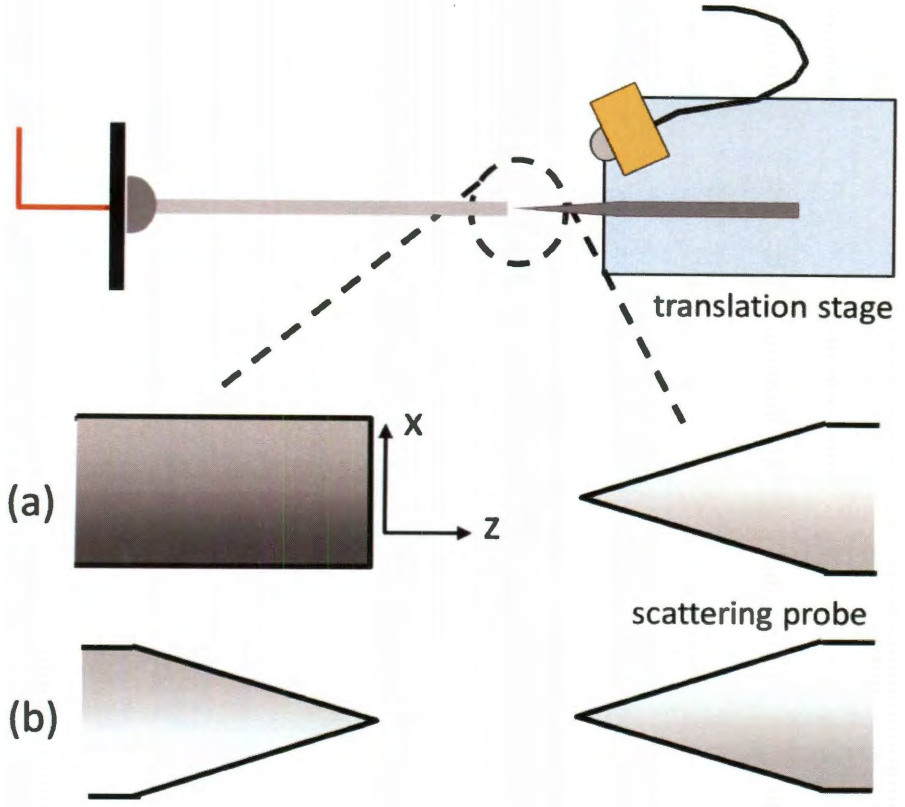

Figure 2-22 Diagram of experimental setup with both untapered (a) and tapered (b) waveguide geometries. The receiver in this diagram is actually 90° out of plane. The receiver and scattering probe are mounted on the same translation stage, while the scattering probe is also mounted on a piezoelectric transducer to modulate its distance from the waveguide.

Terahertz radiation propagates along the waveguide, then couples into free space and scatters off the probe tip. The scattered radiation is detected in the far field using a fiber-coupled receiver. This receiver is positioned 90 degrees out of plane relative to the figure to reduce any asymmetry effects due to receiver positioning. Both the probe and the receiver are placed on a two-axis translation stage, in order to map the E_z field in the two-dimensional region just beyond the end of the waveguide. The probe is mounted on a piezoelectric transducer which shakes

it in the *z* direction with an amplitude of 10 μm and a frequency of 160 Hz. This modulation, which serves as a reference for lock-in detection, greatly increases the signal-to-noise ratio of the obtained data, removes background signals and ensures that the detected signal originates only from scattering at the probe tip [69, 70].

Using this procedure, we map the field at the end of several different waveguides with varying geometries. The initial tests of this procedure used a 1.56 mm diameter steel wire waveguide 25 cm long as the "untapered" control waveguide. An additional tapered section, starting with a matching diameter of 1.56 mm and tapering adiabatically to a tip with diameter 170 μm, is added to measure the confinement. Using the translation stage to move the scattering probe and receiver in a slice along the transverse x-direction, we obtain a plot of the peak-to-peak amplitude of the detected THz signal at various positions relative to the displacement from the waveguide axis for both the tapered and untapered waveguides (Figure 2-23).

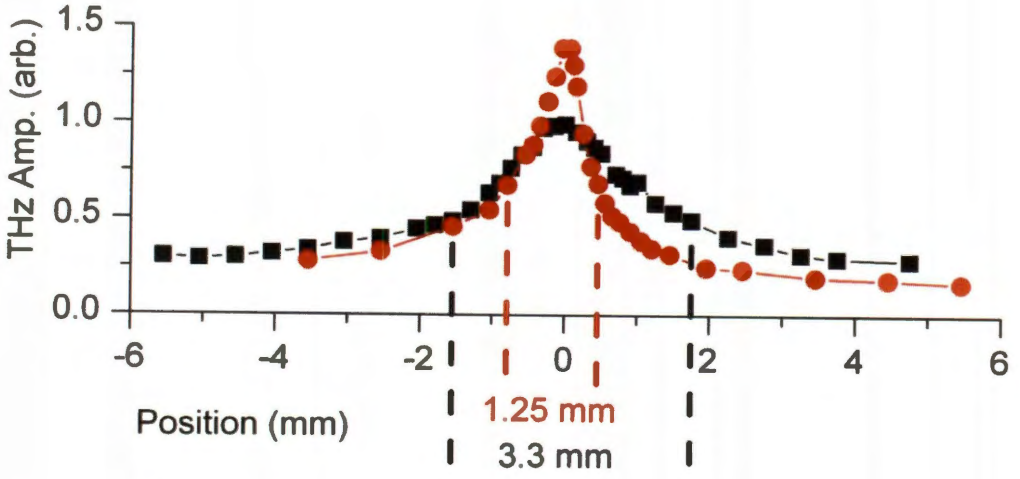

Figure 2-23 Peak to peak amplitude of THz signals for the tapered (red circles) and untapered (black squares) waveguides. The full widths at half max are noted with the dashed lines.

This figure clearly demonstrates both the field confinement (evident in the smaller FWHM) and the field enhancement (evident in the significantly higher peak amplitude) of the tapered tip compared to the untapered case.

We compared these preliminary experimental results to those obtained from finite element method simulation (as described in Section 1.2.2). Since FEM simulation is single-frequency, a Fourier transform was performed on the experimental waveforms at each point to extract the relevant frequency components for comparison to the simulations. The amplitude and phase were used to reconstruct the electric field strength at each point. The best (i.e. lowest noise, clearest pattern) frequency values were chosen for comparison to simulation: 100 GHz in the untapered case and 150 GHz for the tapered (Figure 2-24, red and blue squares).

For the comparison, a radially-polarized wave was simulated on a cylindrical metal waveguide ending with either a tapered or untapered tip. The untapered waveguide diameter was 1.56 mm to match the experiment, while the tapered tip diameter was 250 μm, slightly larger than the experimental diameter (at this scale the difference is assumed to be small.) A 1-D slice of the axial component of the electric field was extracted along a line perpendicular to the waveguide axis at a distance of 200 μm from the plane at the end of the waveguide. (Figure 2-24, black curves). These frequency-domain results demonstrate both an intense primary peak, with significantly greater confinement for the tapered waveguide, and a series of oscillations due to the phase change as the wave propagates which are also replicated in the experimental data. The plots below are all normalized for comparison.

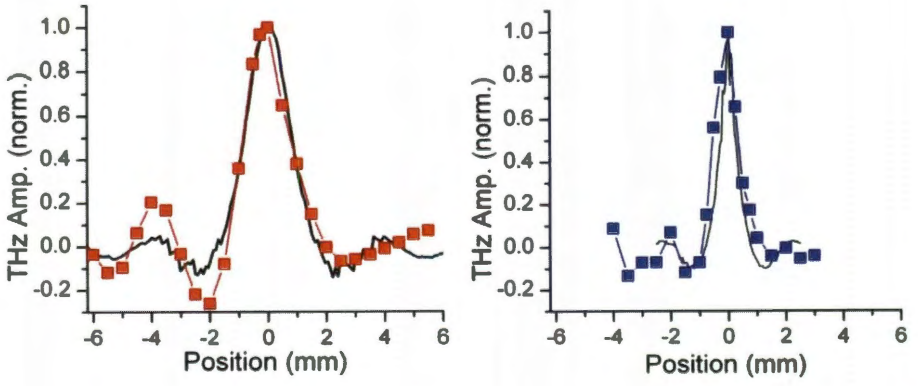

Figure 2-24 (left) Axial component E_z of the electric field at 200 μm from an untapered tip at 100 GHz. (right) Axial component of the electric field at 200 μm from a tapered tip at 150 GHz. In both plots, solid black curves are the FEM simulation and colored squares are the experimental data.

In both tapered and untapered cases, there is excellent agreement with simulation. The FWHM for the tapered case is 0.5 mm in simulation compared to 0.9 mm in experiment, while in the untapered case the FWHM is 1.6 mm for both experiment and simulation. The experimental FWHM of 0.9mm for the tapered wire is approximately $\lambda/2$ for a 150 GHz wave. Therefore we have achieved a confirmation of the subwavelength confinement of the field at the end of the tapered wire waveguide, with quantitative agreement to simulation. However, this result could be significantly improved with a smaller taper – 170 μm is fairly large compared to THz wavelengths.

To explore the possibility of even higher confinement, we continue the experiment with a second set of waveguides, this time with a diameter of 500 μm. The waveguide section coupled to the photoconductive antenna has a flat end and no taper, maintaining this 500 μm diameter. A tapered section with a matching original radius of 500 μm, a taper cone angle of 4.7° and a final diameter of 20 μm is coupled to the end of the untapered wire to form the tapered waveguide [2].

As before, we scan the probe in one-dimension to sample the E_z field at various points along a line perpendicular to the waveguide axis for both the tapered and untapered waveguides, with the probe tip at closest approach ($z \approx 0$). Plots of the peak-to-peak amplitude of the z-component of the terahertz electric field at the

---

[2] Experimental note: this is the same as the tungsten probe tip, made by Micromanipulator.

end of the untapered (blue) and tapered (red) waveguides are shown in Figure 2-25 below. For the untapered waveguide, the full width at half max (FWHM) of the field distribution is approximately 630 μm, which is roughly equal to the waveguide diameter. In contrast, the FWHM for the tapered waveguide is approximately 30 μm, comparable to the taper size and 100 times less than the average free-space wavelength (λ = 3 mm at 100 GHz). The increase in both confinement and maximum field strength for the tapered waveguide versus the untapered one is clearly visible in the figure.

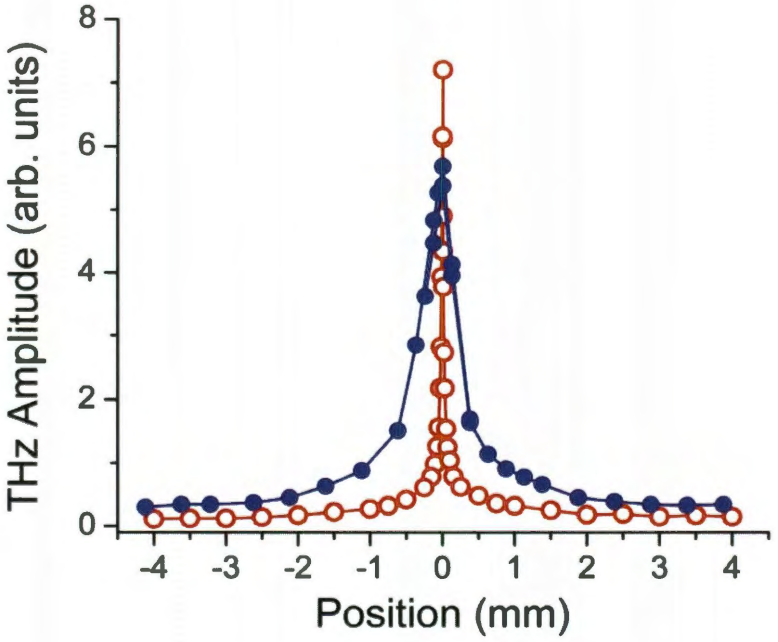

Figure 2-25 One-dimensional (along the *x* direction) plot of the peak-to-peak amplitude of the *z* component of the terahertz electric field at the end of the untapered (solid blue circles) and tapered (open red circles) waveguides. The field confinement for the tapered waveguide is comparable to the size of the tip, roughly 20 times smaller than in the untapered case, and over 100 times less than the average free-space wavelength.

Similarly, we scan the probe in the *z*-direction (parallel to the waveguide axis) to obtain confirmation of the confinement in the axial direction, as predicted for the E_z component in contrast to the radial E_r component, which is predicted to show high confinement only at the tip of the waveguide, before strongly diffracting once the energy escapes into free space [51]. A plot of the peak amplitude for this axial scan is shown in Figure 2-26 below for the untapered and tapered waveguides. The decay of the signal with increasing z follows a power law, as expected for a conical metal tip [74]. For the untapered waveguide, the 1/e distance is 130 μm, while for the tapered waveguide it is only 9 μm, demonstrating the very strong three-dimensional confinement of the axial electric field E_z at the end of a tapered waveguide.

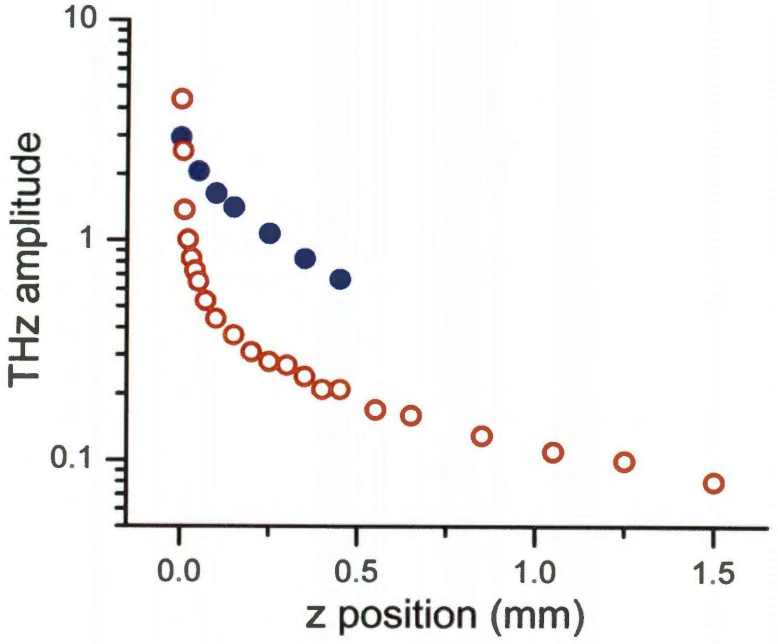

Figure 2-26 One-dimensional (along the axial *z* direction) plot of the peak amplitude of the *z* component of the terahertz electric field at the end of the untapered (solid blue circles) and tapered (open red circles) waveguides. This logarithmic plot shows the power-law decay of the field along the *z* axis.

In addition to the individual *z*- and *x*-direction one-dimensional scans, we also performed full two-dimension *x*-*z* scans of the electric field at the end of both the tapered and untapered waveguides, to generate an image of the field confinement. Figure 2-27 (a) and Figure 2-28 (a) below show such images, calculated by plotting the peak-to-peak amplitude at each location on the x-z grid and interpolating to create a smooth color map. Figure 2-27 (b) and Figure 2-28(b) are images of the E_z amplitude at 100 GHz obtained from FEM simulation of similar geometries to those in the experiments. Note the extended scales in the *z* direction; the axial component in both cases is confined to within a few hundred microns in the z direction as a natural consequence of propagation and diffraction of the wave.

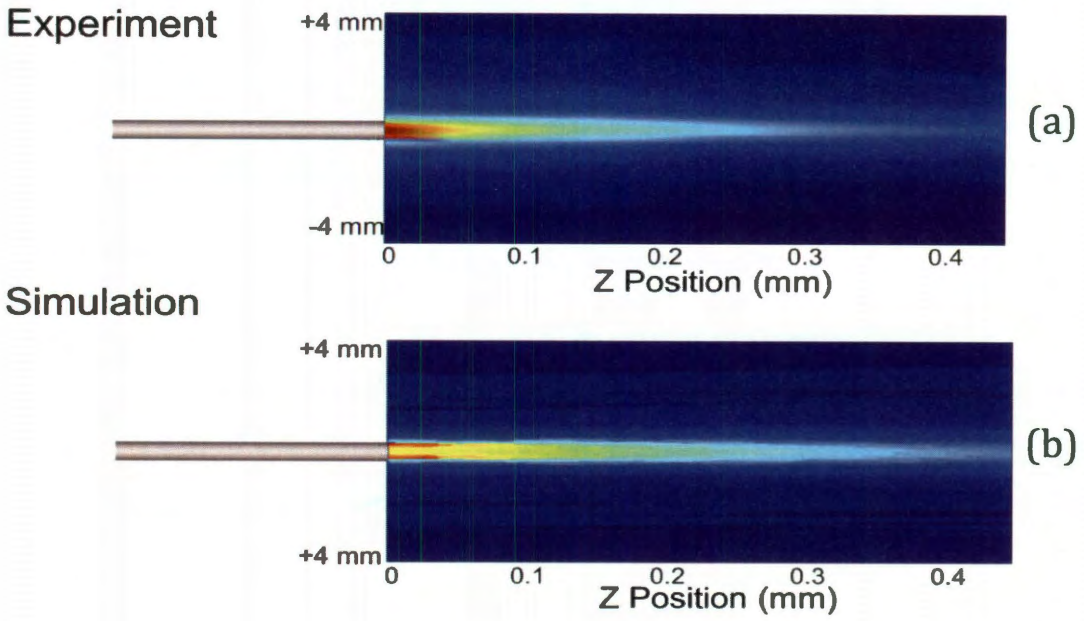

Figure 2-27 Experimental (a) and simulated (b) plots of the *z* component of the electric field in the region just after the end of the untapered waveguide.

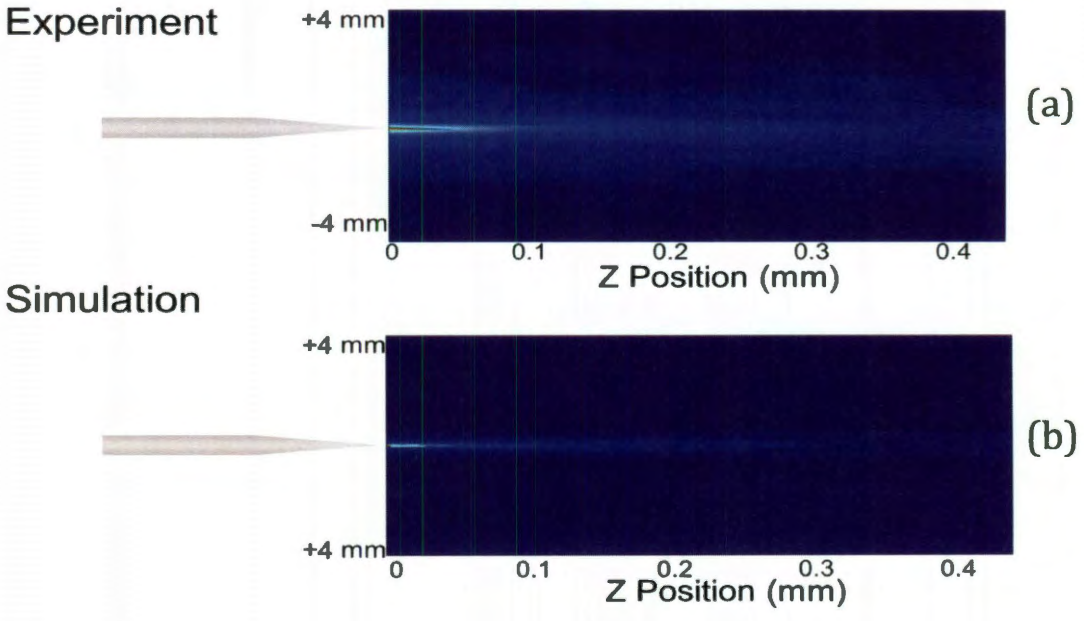

Figure 2-28 Experimental (a) and simulated (b) plots of the *z* component of the electric field in the region just after the end of the tapered waveguide.

It is clear from these images that there is excellent qualitative agreement between experiment and simulation, with the three-dimensional confinement exhibited by the tapered waveguide clearly visible.

We also conducted a more thorough quantitative comparison between the experimental and simulation results. As before, the experimental time-domain waveforms are Fourier transformed to extract the amplitude and phase of the terahertz field at 100 GHz along a line perpendicular to the waveguide axis with the probe tip at closest approach (Figure 2-29 below, red squares). This "closest approach" point is estimated to be at approximately z = 5 μm, based on the oscillation amplitude of the probe tip. A scan of E_z at this distance from the waveguide tip is extracted from the FEM simulation (Figure 2-29 below, black line) and compared to the experimental results.

At 100 GHz, the experimental FWHM is 31 μm, whereas the simulation indicates a higher field confinement with a FWHM of 17 μm. This difference, roughly a factor of 2, could result from experimental considerations, such as an incorrect determination of the ($z \approx 0$) point of closest approach or a misalignment of the probe in a direction orthogonal to the waveguide axis. Or, more interestingly, the discrepancy could result from a modification of the field confinement by the presence of the scattering probe. This modification would arise from the distortion of the charge distribution in the metal waveguide induced by the nearby metal scattering probe. In analogy to the formation of an image dipole when a metal object is close to a ground plane, this would strengthen the field at the tip of the

waveguide relative to the field without the probe. This is essentially equivalent to the well-known "height artifact" of apertureless near-field microscopy [75] and could lead to an inaccurate estimation of the field confinement at the tip of an isolated tapered waveguide.

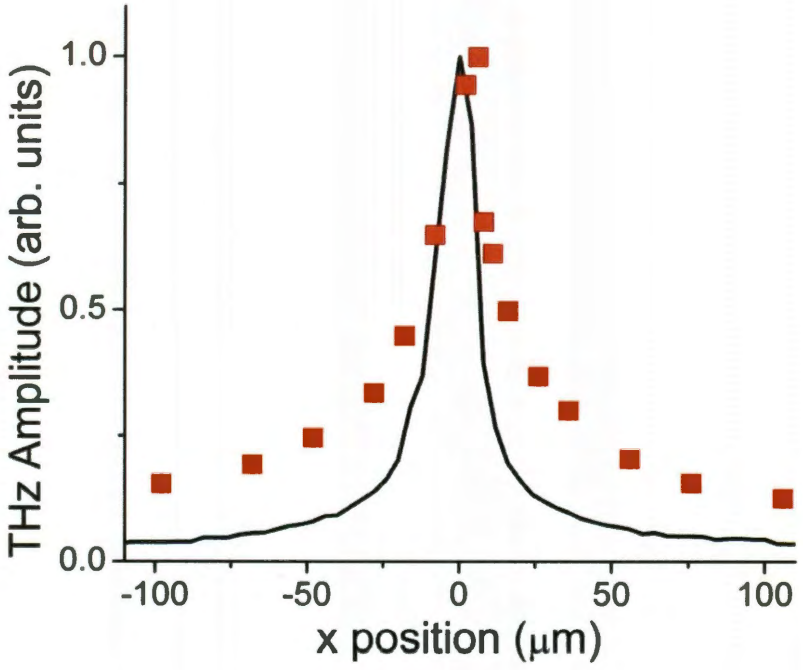

Figure 2-29 A comparison of measured and simulated one-dimensional E_z field patterns along the *x* direction. The red squares denote the experimentally measured values at 100 GHz, extracted from the time-domain waveforms by Fourier transform. The solid black line is the result of a single FEM simulation, showing the value of E_z along a line at $z = 5$ μm beyond the end of the tip. Both are normalized for comparison.

To investigate this latter possibility, we have performed a series of additional FEM simulations and extracted slices of E_z in the x-direction at a distance of $z = 5$ μm beyond the end of the waveguide for several waveguide geometries (Figure 2-30 below).

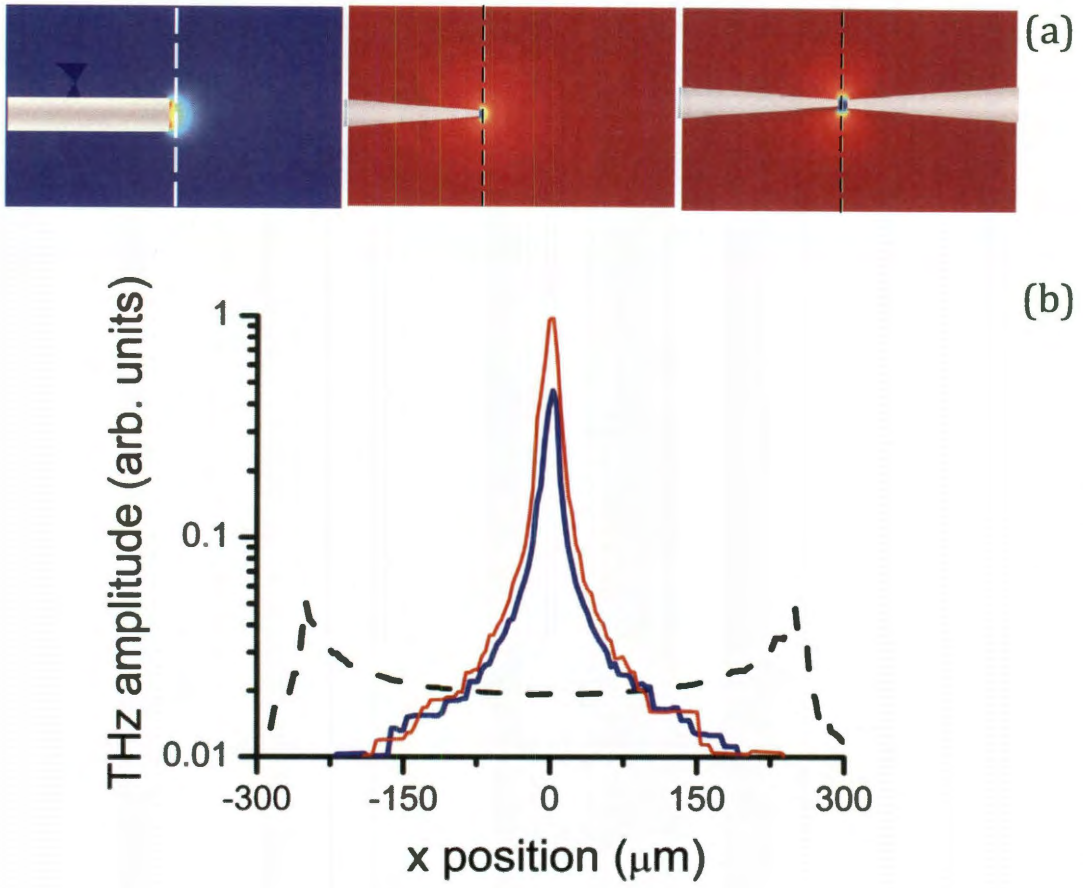

Figure 2-30 (a) Plots from FEM simulation of the field at the end of three different waveguide configurations. Left: an untapered waveguide. Center: a tapered waveguide. Right: A tapered waveguide with a probe located 10 μm away. (b) Plots of the strength of the axial field component E_z along a line 5 μm from the end of each waveguide configuration, untapered (black dashed line), tapered (blue line) and tapered with the probe present (red line). Tapering the waveguide leads to a field enhancement on-axis of about a factor of 10, relative to the untapered waveguide. Adding a second metal tip leads to an *additional* enhancement of about a factor of 2.

The dashed curve shows the results for an untapered waveguide, exhibiting small peaks at $x = \pm 250$ μm, the positions corresponding to the locations of the two (in the simulations, perfectly sharp) corners where the cylindrical wire terminates. The tapered waveguide (thick blue curve), identical to that plotted in Figure 2-29, shows a dramatic (factor of 10) field enhancement at $x = 0$ and a correspondingly

high field confinement. In the third simulation (thin red curve), we add a *second* tapered metal structure on axis, representing the probe, at a position z = 10 μm from the waveguide. This clearly leads to an additional strengthening of the field, roughly by a factor of 2 at x = 0. These results indicate that the presence of the probe has some effect on the measured field enhancement and field confinement.

However, this figure is not sufficient in understanding the effect of the probe, because those enhancement and confinement effects are dependent on the relative positions in the x-direction of the probe and waveguide, which naturally varies as the probe is scanned across the waveguide end facet. Figure 2-31 below presents an image from simulation of the E_z field for a probe position offset from the waveguide axis. An enhancement of the field is visible at the end of the tapered waveguide, as before, but also at the end of the scattering probe. This indicates that the presence of the probe will have an effect on the measured field pattern even at significant distances from the waveguide axis.

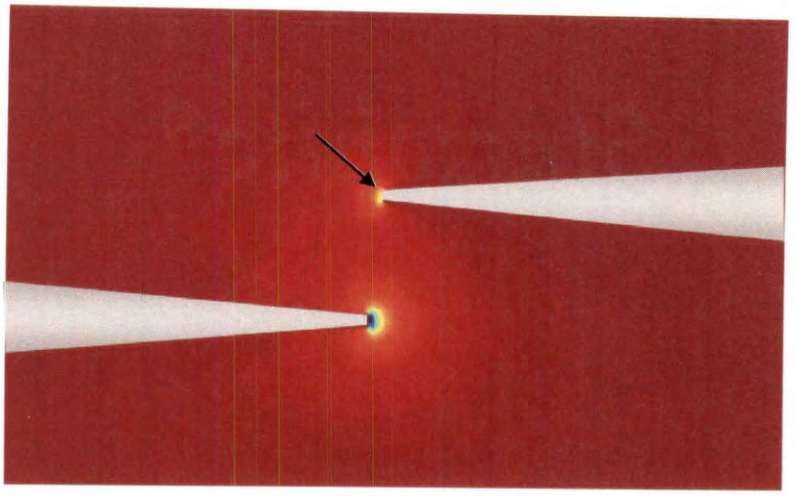

Figure 2-31 Plot of the E_z field at the end of the tapered waveguide in the presence of the scattering probe when the probe is offset from the waveguide axis. There is a distinct enhancement at the tip of the scattering probe in addition to that at the end of the waveguide.

To investigate the effect of this second probe on the measured field at the tip of the tapered wire waveguide, we perform additional simulations, in which the scattering probe is included at z = 10 μm at various offset positions along the *x*-direction (Figure 2-31 above is one example). At each offset, we extract the value of E_z at a position 5 μm from the end of the probe (indicated by arrow). This procedure accounts for the additional field strengthening as well as its dependence on the lateral (*x*) offset of the probe. We compare these results to the previously presented (Figure 2-29 above) results from experiment and from simulation without the probe. All three plots are presented in Figure 2-32 below.

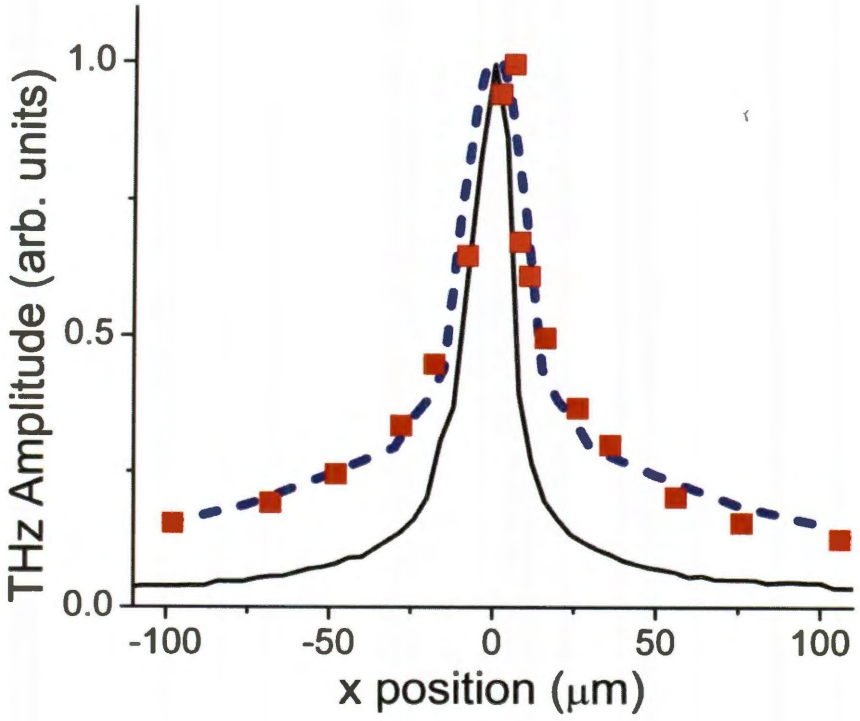

Figure 2-32 A comparison of measured and simulated one-dimensional field patterns along the *x* direction. The red squares denote the experimentally measured values at 100 GHz. The solid black line is the result of a single FEM simulation, showing the value of E_z at z = 5 μm beyond the end of the tip. The dashed blue line is extracted from a series of FEM simulations, each including both the tapered waveguide and the scattering probe. This shows the effect of the field strengthening that results from the presence of the probe. All are normalized for comparison.

The results from simulation including the effect of the scattering probe (Figure 2-32 dashed blue curve) show much better agreement with the experimental results at 100 GHz. As a result, we conclude that the measured field confinement of ~ 30 μm in fact corresponds to a true field confinement of less than 20 μm in the absence of the scattering probe, a confinement approximately equal to the tip diameter of the tapered waveguide.

In conclusion, we experimentally confirmed the subwavelength confinement of the *z*-component of the electric field at the end of a tapered metal wire waveguide in agreement with numerical simulations. The scale of the lateral confinement is tip-size limited and more than 100 times smaller than the free-space wavelength. This result supports the use of tapered waveguides for THz near-field imaging applications and for generating high-intensity localized terahertz surface plasmons, thereby laying a firm foundation for the applications already being employed or considered by other researchers. We have also established that the presence of a (detecting) scattering probe can modify the apparent degree of field confinement, and must be considered for a quantitative analysis. The effect of the detector on the confinement is also a concern for near-field imaging applications, where the presence of a conductive sample may alter the field and limit the achievable confinement and by extension the achievable spatial resolution of the images. Lastly, the confirmation of three-dimensional confinement of the E_z field component implies that E_z may be more experimentally fruitful than the radial component which exhibits only 2D confinement, which may be an important concern for future experimental implementations of the tapered wire waveguide.

Chapter 3

Parallel-Plate Waveguides

Some of the results presented in this chapter have been previously published in references [76] and [77].

3.1. Introduction to the Grooved Parallel-Plate Waveguide

The primary application intended for most waveguides is the transportation of radiation – as the name says, to guide waves. Because of this, waveguide research such as the work discussed in Chapter 2 often focuses on the capacity of a waveguide to transport radiation long distances, to direct it around bends or along non-line-of-sight paths, or to focus or confine the radiation. However, due to the fact that waveguides by their nature control or confine radiation, they can also be employed in conjunction with resonant structures in order to create devices such as sensors and filters.

The development of resonant structures in the terahertz has grown as an area of research in recent years, with a variety of structures being proposed for different sensing applications. Many designs have been studied at terahertz frequencies, such as dielectric fiber-based sensors [78, 79], photonic crystal structures and cavities [20, 80, 81], corrugated metallic slit waveguides [82], metallic meshes [83], and split-ring resonators [84-86]. In addition, there have also been several designs that employed resonant structures embedded within parallel-plate waveguides (PPWGs) such as Bragg gratings and photonic band gap structures [87-89]. In the basic parallel-plate waveguide structure, the electromagnetic energy is confined between the flat surfaces of two bulk conductors, frequently thick plates of aluminum or other metals. While the wave is free to expand in the direction parallel to the plates, it is confined in the direction perpendicular to the plates, and as separation between the plates is generally smaller than the extent of a free space terahertz beam this leads to a concentration of the energy into a small, well-controlled area. By placing resonant structures inside such a waveguide, higher extinction and longer interaction lengths can be obtained.

Previous work with resonant structures in PPWGs has focused on incorporating these structures into PPWGs operated using the transverse electromagnetic (TEM) mode, which provides low-loss and low-dispersion propagation of the terahertz waves [25]. These designs were effective at producing stopband filters [87, 88], transmission resonances [87, 88], and notch filters [89]. However, in general the designs were fairly complex to fabricate. To ensure single-mode propagation, TEM-mode parallel-plate waveguides are generally operated

with plate separations on the order of ~100 μm, requiring a complicated silicon lens scheme to couple the terahertz radiation into the waveguide from free space. The resonant structures are similarly complicated, generally taking the form of a Bragg grating with feature sizes of less than 100 μm which must be fabricated by lithography and other clean room techniques. Using these structures as a sensor, for example, would require a sophisticated fabrication, the incorporation of a sample into a complicated structure in a repeatable, uniform way, and a coupling system that can be difficult to align.

To overcome these difficulties, Mendis et al. proposed an alternative parallel-plate waveguide resonant structure: a simple rectangular groove machined into one face of the waveguide, which is operated in the lowest-order transverse electric mode (TE_1) instead of TEM mode [90]. This structure is simple to machine, requiring only a machine shop mill and a saw blade of appropriate width, and it is already incorporated into the waveguide. By operating in TE_1 mode, the waveguide geometry is on a more manageable scale -- millimeters instead of 10s of microns -- thus it does not require any complicated alignment of coupling lenses, and the process of introducing a sample into the resonant structure is considerably more straightforward. Also, the groove generally produces a single narrow line-width notch resonance, which is more desirable than a stopband or low- or high-pass filter for materials sensing applications.

The single groove PPWG geometry was proposed, demonstrated, and applied as a microfluidic sensor in previous work [1]. However, the underlying mechanism

of this resonance was not at all understood, and the true capabilities of the sensor had not been established. The work presented in this Chapter consists of experiments, analysis, and simulation to fully characterize the single groove waveguide resonant structure, and then to expand its capabilities by exploring variant geometries to widen its application potential, including establishing its capabilities for multichannel sensing.

3.2. Transverse Electric Parallel-plate Waveguide Modes

The parallel-plate waveguide is a physically and mathematically simple structure that is well understood in classical waveguide theory. It consists of two parallel conductive plates, which confine the wave in one transverse direction but extend infinitely in the other (see Figure 3-1). Waves propagate between the plates with their electric field polarized either perpendicular to the plates (TM) or parallel to the plates (TE).

In the lowest-order transverse electromagnetic (TEM) mode, the electric field is oriented perpendicular to the plates with a uniform magnitude across the gap. This mode has no cutoff frequency, and consequently it has no group velocity

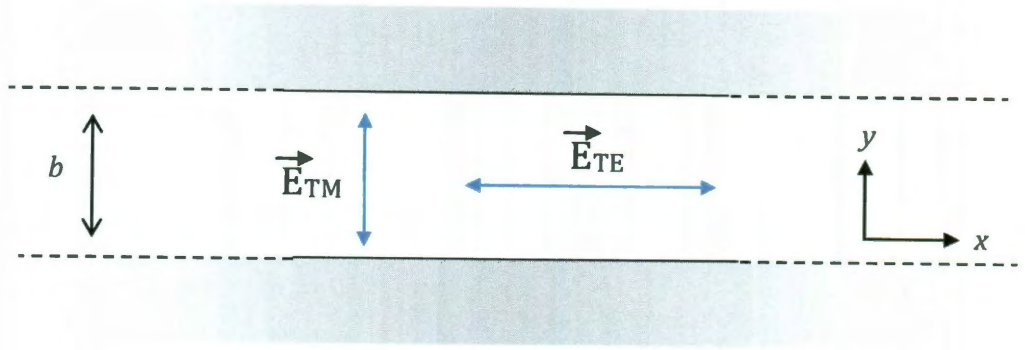

Figure 3-1 Diagram of parallel-plate waveguide geometry, including plate spacing *b* and the electric field orientation for TM and TE modes. Propagation is into/out of the page, in the *z*-direction.

dispersion for plates of infinite conductivity and very minimal dispersion for finite conductivity plates [3]. It also exhibits very low losses, which combined with the lackof dispersion makes the TEM mode very useful for long-distance undistorted pulse propagation [25]. TEM-mode parallel-plate waveguides have been used for spectroscopy [28], sensing [29], imaging [27, 30], and superfocusing [26] among other applications, in addition to providing a base for the resonant structures discussed above in Section 3.1.

In contrast, the transverse electric (TE) modes of the PPWG have an electric field oriented parallel to the plates instead of perpendicular. Whereas the TEM mode has only transverse E_y and H_x components, TE modes also have a longitudinal

[3] The equations and theory discussion presented in this Chapter are based on plates with infinite conductivity. The effect of finite conductivity is negligible at terahertz frequencies.

magnetic field component H_z. The TE field components are given by the equations from classical waveguide theory [91]:

$$E_x = \frac{A_n \beta_y}{\varepsilon} \sin(\beta_y y) e^{-j\beta_z z} \quad \text{[3-1]}$$

$$H_y = \frac{A_n \beta_y \beta_z}{\omega \mu \varepsilon} \sin(\beta_y y) e^{-j\beta_z z} \quad \text{[3-2]}$$

$$H_z = -j \frac{A_n {\beta_y}^2}{\omega \mu \varepsilon} \cos(\beta_y y)\, e^{-j\beta_z z} \quad \text{[3-3]}$$

where A_n is the amplitude of each mode and the phase constants β, β_y and β_z are given by:

$$\beta = \frac{2\pi}{\lambda} \quad \text{[3-4]}$$

$$\beta_y = \frac{n\pi}{b} \quad \text{[3-5]}$$

$$\beta_z = \sqrt{\beta^2 - {\beta_y}^2} \quad \text{[3-6]}$$

where n is the mode number, λ is the wavelength, and b is the spacing between the two plates. It is clear from these equations that TE modes have a low-frequency cutoff.

The cutoff frequency for the *n*th mode is given by:

$$f_{cn} = \frac{nc}{2b} \qquad [3\text{-}7]$$

A consequence of this cutoff frequency is high dispersion at frequencies near the cutoff, leading to severe distortion of a terahertz pulse. At a typical plate spacing of 500 μm, this cutoff frequency for the first-order TE_1 mode is 300 GHz, well within the bandwidth of THz radiation in a photoconductive system. For this reason, the TE_1 mode was not commonly employed for terahertz time-domain measurement.

However, because the cutoff frequency is dependent on the plate separation, this dispersion can be minimized by widening the gap between the two plates from 500 μm to 5 mm, moving the cutoff frequency to 30 GHz, near the low-frequency limit of the input THz frequency range and allowing a typical time-domain terahertz pulse to propagate without dispersion [92]. However, a lower cutoff frequency can lead to multimode propagation in the waveguide, as now there are several modes (TE_1, TE_3, TE_5, etc.) within the input frequency spectrum. This effect can be minimized by optimizing the input coupling.

This can be done fairly simply due to the modal field patterns for the transverse-electric modes. They are given by

$$\Phi_n = \sqrt{\frac{2}{a}} \sin\left(\frac{n\pi y}{a}\right) \qquad [3\text{-}8]$$

Figure 3-2 below is a diagram of these field patterns inside a waveguide. It is clear that there is a similarity between the TE_1 mode pattern and that of a Gaussian input beam. Even-numbered modes (TE_2, TE_4) will not couple due to symmetry, and higher-order modes can be eliminated by matching the diameter of input Gaussian beam to that of the TE_1 mode pattern, leading to single-mode TE_1 propagation [92]. This also simplifies the coupling scheme, since this is obtained by direct coupling from free space without the use of lenses as required by TEM mode operation.

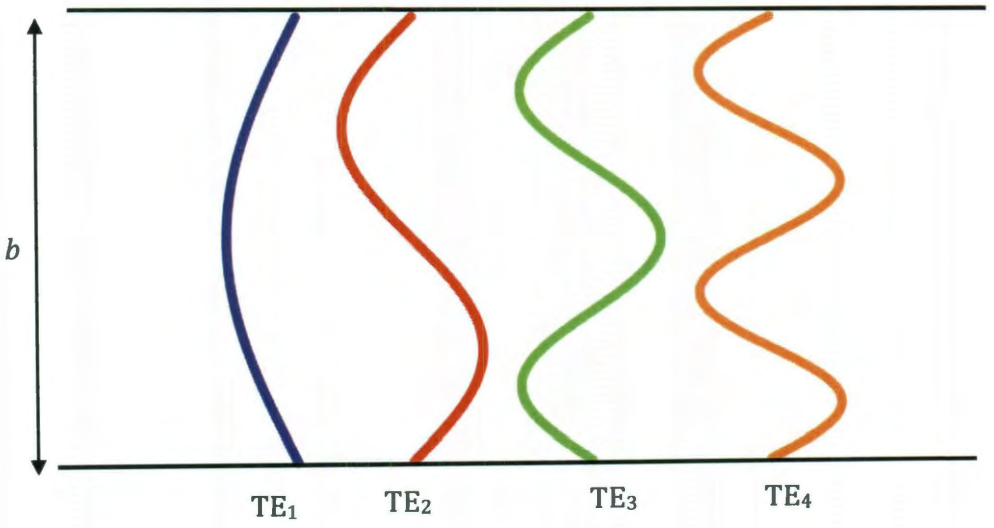

Figure 3-2 Electric field patterns for the TE_1 to TE_4 modes of the parallel-plate waveguide

As well as improved coupling, the TE_1 mode has another advantage over the TEM mode for parallel-plate waveguide applications: low ohmic loss.

To compare, the equations for the ohmic loss for both TEM and TE modes are given below:

$$\alpha_{TEM} = \frac{2nR_s}{Z_0 b} \quad \textbf{[3-9]}$$

$$\alpha_{TE} = \frac{4nR_s(f_c/f)^2}{Z_0 b\sqrt{1-(f_c/f)^2}} \quad \textbf{[3-10]}$$

where R_s is the surface resistance $(\pi f\mu/\sigma)^{1/2}$ and Z_0 is the free-space impedance [90]. These equations show an interesting dependence on frequency. For the TEM mode, the attenuation increases as frequency increases due to the decreasing skin depth. However, for the TE modes, attenuation actually decreases with increasing frequency. When the cutoff is pushed to lower frequencies by increasing the plate separation, the ohmic loss for the TE modes becomes significantly lower than that of the TEM mode at all frequencies of the input spectrum – several orders of magnitude lower at 1 THz [90].

In addition to the lower loss and improved coupling, TE modes also have several unique applications in comparison to the TEM mode – whispering gallery modes [93], artificial dielectrics [94], tunable spectral filters [95], etc. One such application is a very simple resonant structure: a single rectangular groove machined into one face of the waveguide. In the initial experimental demonstration, a groove with dimensions 538 μm x 538 μm in a waveguide with a plate spacing of 1mm gave a single strong high-extinction resonance at 280 GHz [90], and later

experiments confirmed that the single strong resonant feature is characteristic of this resonant structure geometry [1, 76].

It is this resonant groove that is the focus of the next several sections of this thesis. The origin of the resonant behavior and its dependence on geometric factors are not well understood, and so we collect data through simulation and experiment to develop an analytical understanding of the resonance.

3.3. The Grooved Parallel-Plate Waveguide

The grooved parallel-plate waveguide is a very simple design. A diagram of this structure geometry is shown below (Figure 3-3). The extent of the groove along the direction of propagation is labeled the "width" and the extent of the groove into the plate is the "depth". In theory and simulation we treat this groove as infinite in the *x*-direction – the direction transverse to the beam propagation direction and parallel to the plate surfaces – while in experiments the groove is fabricated to extend beyond the size of the propagating beam so as to be effectively infinite.

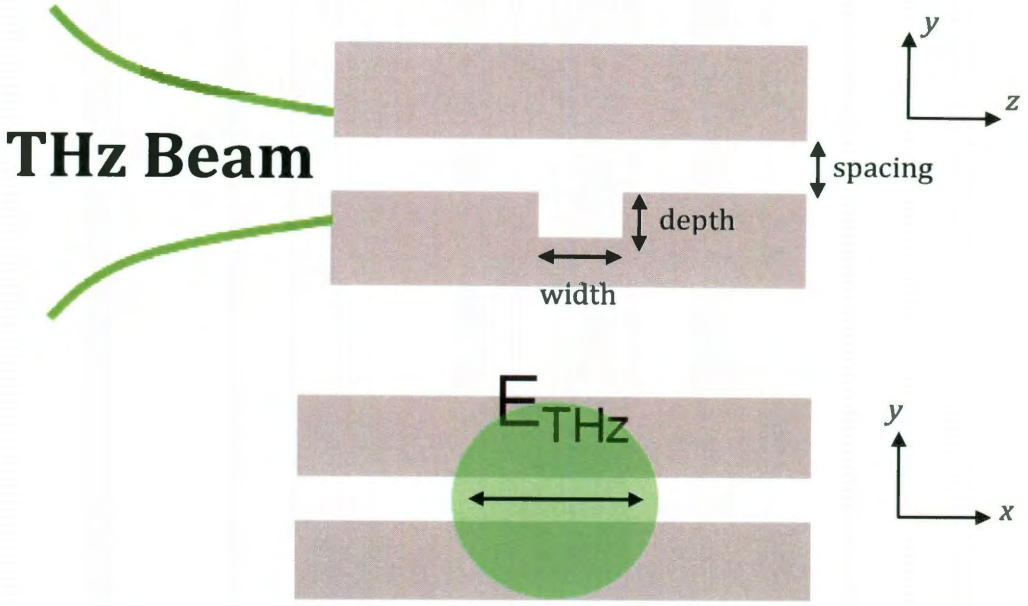

Figure 3-3 Diagram of the grooved parallel-plate waveguide showing geometric parameters and the orientation and direction of the incident electric field.

To excite the resonance, we illuminate this waveguide with terahertz radiation polarized parallel to the plates. This ensures that only TE modes are excited, not TM or TEM modes.

We begin our investigation of the resonance with finite element method simulation, as described in Section 1.2.2. We use a groove with a width of 460 μm and a depth of 412 μm as our default test geometry, based on a previous experimental geometry [1]. Figure 3-4 below shows the power transmission spectrum calculated for a 6.4 mm long waveguide of plate spacing 1 mm with this groove incorporated.

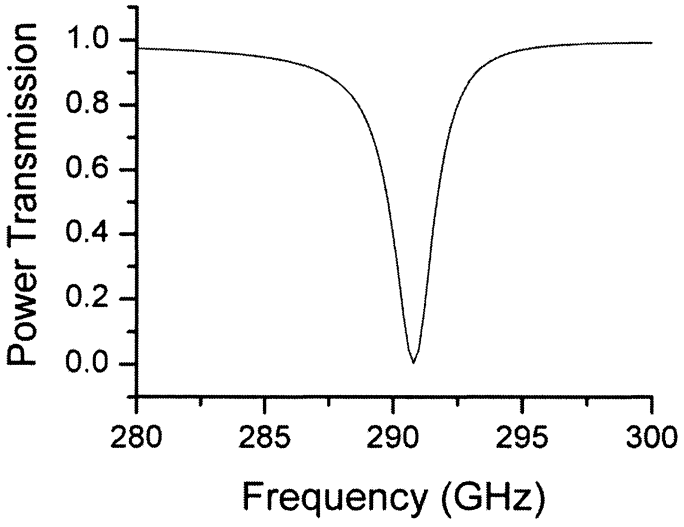

Figure 3-4 Simulated power transmission spectrum for PPWG with groove geometry 460 by 412 μm.

This spectrum shows the characteristic single high-extinction resonant feature at 290.8 GHz. To investigate the origin of this resonance, we extract images of the electric field patterns inside the waveguide for both grooved and ungrooved waveguides with propagation in TEM and TE modes, at frequencies on- and off-resonance. In Figure 3-5 below, the images on the left are for a TEM mode waveguide, while the images on the right show TE_1 propagation for a waveguide of the same geometry.

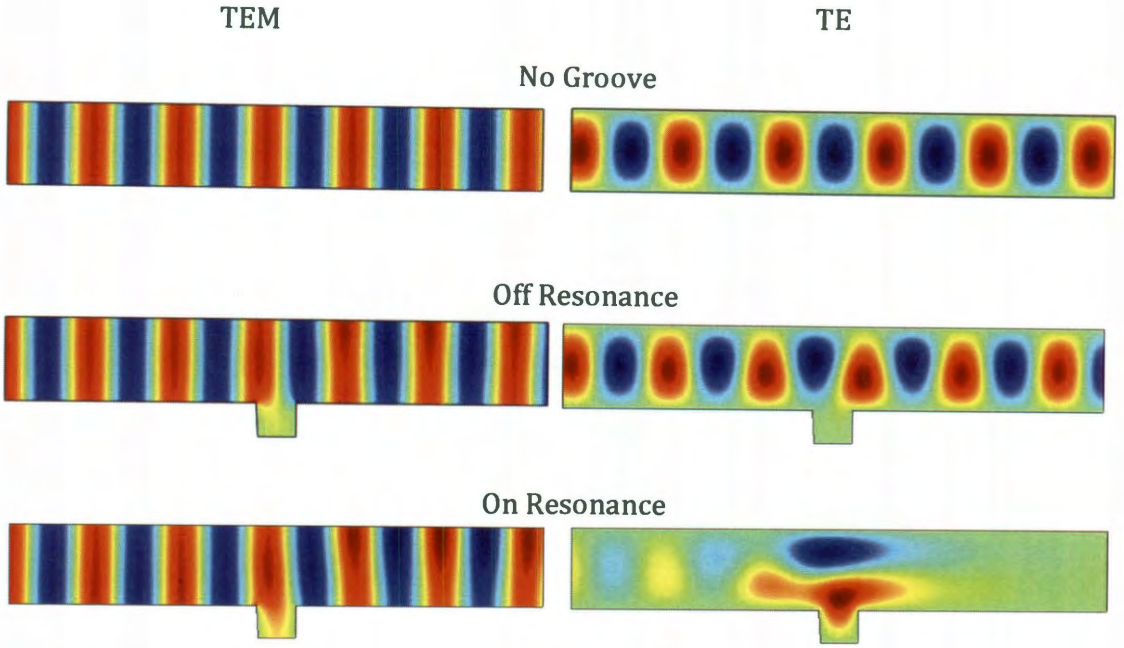

Figure 3-5 Simulated electric field patterns for TEM (left) and TE (right) mode waveguides. The TEM plots are of E_y, the TE plots are of E_x. Top row: waveguide with no groove. Middle: Grooved waveguides at 300 GHz, off resonance. Bottom: Grooved waveguides at 290.8 GHz, at resonance.

With no groove (Figure 3-5, top), both TEM and TE_1 modes propagate effectively. The uniform field distribution of the TEM mode and the sinusoidal distribution of the TE_1 mode are clearly visible. A single groove is then incorporated into both waveguides. At frequencies other than the resonance (in this case, 300 GHz), the groove has no strong effect on the transmission of either TEM or TE_1 mode radiation (Figure 3-5, middle). At the resonant frequency of 290.8 GHz, the TE_1 mode radiation is fully reflected by the groove, resulting in the transmission dip we identify as a resonant feature. In contrast, the TEM mode is merely perturbed slightly, with no significant decrease in power transmission.

The next step is to obtain experimental data of the resonance. We fabricate waveguides with grooves of varying widths and depths machined into polished aluminum plates. For each waveguide, the geometry of groove is listed in the discussion of that waveguide's resonant behavior. The waveguides were assembled by screwing the top and bottom plates together, with dielectric spacers fixing the plate separation at 1mm (± 5 μm). A photo of the waveguide is shown in Figure 3-6 below.

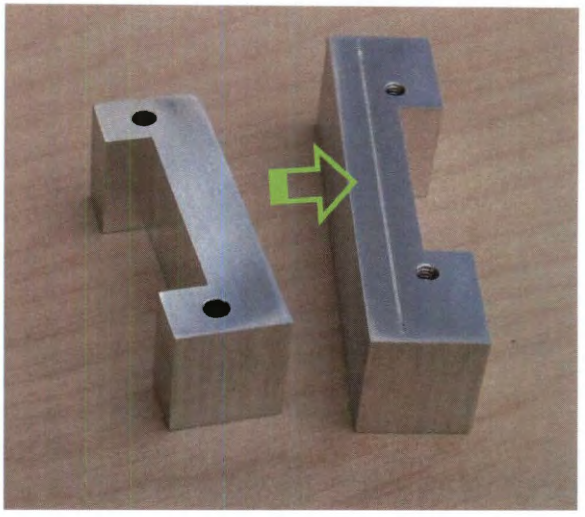

Figure 3-6 Photograph of the test waveguide. The propagation direction through the grooved plate is marked with a green arrow.

To obtain the frequency-dependent transmission spectra, we placed these waveguides in the conventional THz-TDS system as described in Section 1.2.1. The incident broadband radiation is weakly focused onto the input facet using a confocal lens setup, with an aperture limiting the size of the beam to 12 mm in diameter (Figure 3-7 below). To excite the TE propagation modes, the waveguide is oriented

with the plates parallel to the electric field direction. The radiation from the output end of the waveguide is collected and the time-domain waveform obtained. Because of the expectation of very narrow linewidths, we need the highest possible spectral resolution obtainable from a TDS system, and so we collected the waveforms with an extended time window of 1.6 ns, giving a spectra resolution of ~0.6 GHz. The 1.6 ns limit was due to a reflection in the system, which prevented the exploitation of the entire 2.6 ns available window [4].

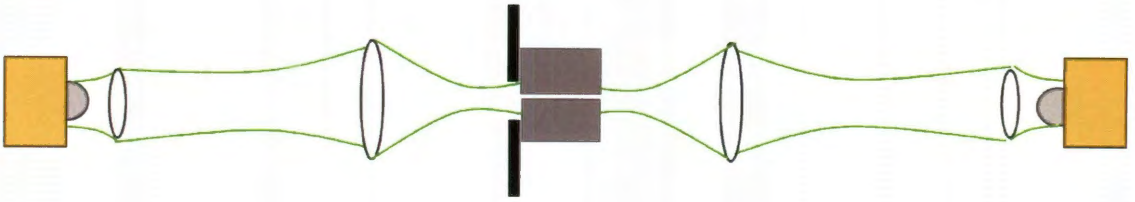

Figure 3-7 Diagram of experimental setup. The confocal lenses, aperture, and waveguide are shown. The electric field is polarized out of the plane of the page.

When time-domain waveforms are obtained for both grooved and un-grooved waveguides, these waveforms are Fourier transformed, then the spectra are divided and squared to give the power transmission spectrum. A sample time-domain waveform and FFT for a waveguide with a groove measuring 400 μm wide by 406 μm deep are plotted in Figure 3-8 below.

---

[4] Experimental note: to obtain this full window, a shorter fiber leading to the transmitter head is required, to push the signal earlier in the visible time window. In fact, a 4.55 m fiber pushes the signal outside the visible time window for the Long Scan, but it is visible in Rapid Scan mode for the T-ray 4000. To access this -280 to 0 ps section of the window, the program must be open before the system is turned on, then the window dragged as early as possible. Restarting both the system and program may be necessary.

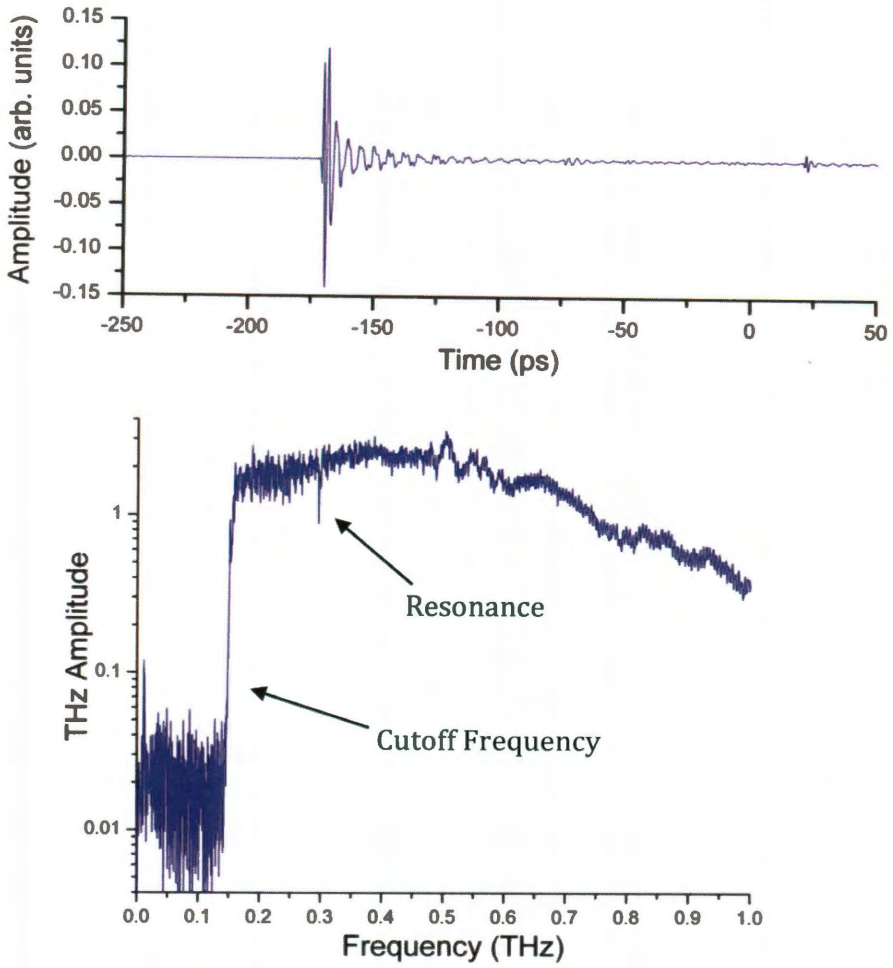

Figure 3-8 Time domain waveform (top) and frequency domain spectrum (bottom) of the waveguide with a groove 400 μm wide by 406 μm deep.

The plate spacing chosen for these experiments and simulations is 1mm, which has a cutoff frequency of 150 GHz, well inside the bandwidth of the incident time-domain waveform, resulting in a broadened and positively chirped output pulse, as illustrated by the experimental time-domain waveform in Figure 3-8. In the frequency domain, the cutoff is clearly visible. However this dispersion has little effect on the frequency-domain spectral measurements required by the sensing

applications of interest in this work, and by using a smaller separation than the 5 mm required for dispersionless propagation we can obtain stronger coupling to the cavity due to the increased energy density in the waveguide.

This strong coupling is reflected in the high extinction and narrow linewidth exhibited by the experimental power transmission spectrum (Figure 3-9). When a single groove with the geometry given above is incorporated into the waveguide, the resonant feature at 288 GHz exhibits 7 dB extinction and a 1.5 GHz linewidth. In the initial proposal of this grooved-PPWG geometry, the linewidth was among the narrowest ever reported [90]. This narrow linewidth is of particular interest, as it allows for increased sensitivity in sensing applications -- a narrow line width means smaller frequency shifts can be detected, therefore a higher sensitivity can be achieved. One such sensing application was previously demonstrated, in which simple straight chain alkanes were used to test the sensitivity of this resonance to a material's refractive index [1], which will be discussed in detail in Section 3.7.

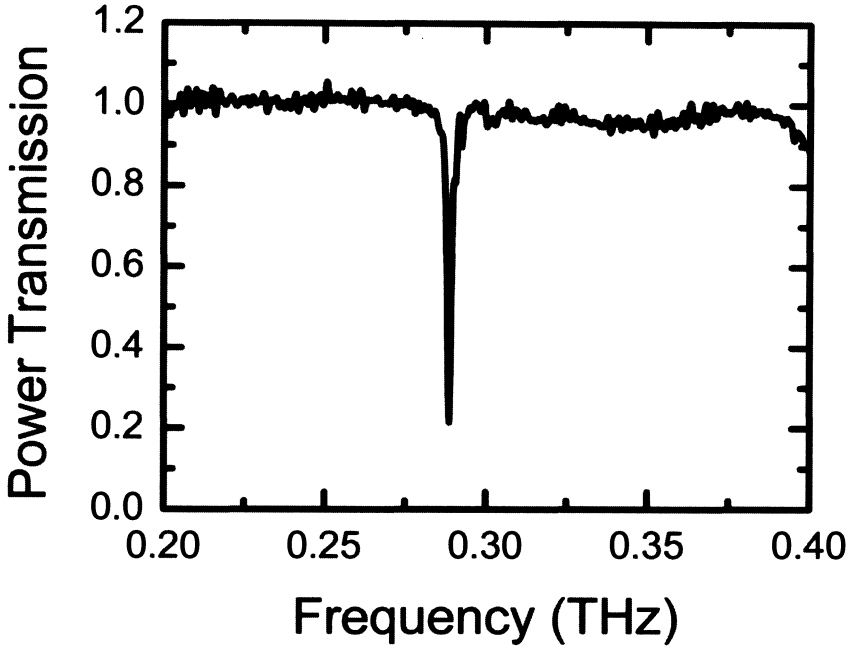

Figure 3-9 Experimental power transmission spectrum for a waveguide with a groove of width 400 μm and depth 412 μm.

The basic concept and sensing ability of this grooved PPWG resonant structure has been effectively demonstrated in these previous references. In this previous work, it was assumed that this groove performed as a simple rectangular resonant cavity, whose resonance arises from standing waves set up between the cavity walls, and whose resonant frequency is determined by the following equation:

$$f = \frac{c}{2}\sqrt{\left(\frac{m_1}{d_1}\right)^2 + \left(\frac{m_2}{d_2}\right)^2 + \left(\frac{m_3}{d_3}\right)^2} \qquad \textbf{[3-11]}$$

For the initial experimental geometry of 538 μm by 538 μm, this equation yields a resonant frequency of 279 GHz if the cavity is assumed to be one-dimensional with only the width of the groove affecting the resonant frequency (m_1 = 1, $m_2 = m_3 = 0$, d_1 = 538 μm). This value agreed well with the experimental value of 280 GHz, leading the authors to conclude that the simple rectangular groove did indeed function as a simple 1-D resonant cavity [90].

However, this theory was quickly refuted by later experiments. The next test waveguide had geometry 460 x 412 μm, which had an experimental resonant frequency of 291 GHz while the resonant cavity theory predicted 326 GHz for a 1D cavity and 488 GHz for a 2D cavity. Additionally, experimental tests of the dependence of the resonant frequency on the spacing between the plates demonstrate that the resonance does not arise solely from the cavity geometry. To investigate this dependence, we placed a waveguide with a single groove of 460 by 412 μm in an apparatus that continuously varies the waveguide plate separation. In this configuration, we observe a resonant dip that gradually red shifts with increasing plate separation (Figure 3-10, blue squares). The experimental apparatus, while it provides an accurate measurement of the relative change in plate spacing, does not allow for accurate determination of the absolute plate spacing, and so these values are calibrated using results from a finite element method simulation (black curve). The immediate conclusion from this data is that the resonance cannot arise solely from the cavity geometry, but from the waveguide structure as a whole.

A few additional observations can be also be made. As the plate spacing decreases, the resonant frequency decreases, while the cutoff frequency for the TE_1 simultaneously increases. At small plate spacings, the two begin to overlap and the resonance becomes undetectable. We also note that changing the plate spacing shifts the resonant frequency in a predictable, almost linear fashion, at a rate of roughly 150 GHz/mm. This implies that slight changes in plate spacing (on the order of 100 μm or less) can be used to compensate for fabrication errors when designing waveguide cavities to resonate at a specific frequency.

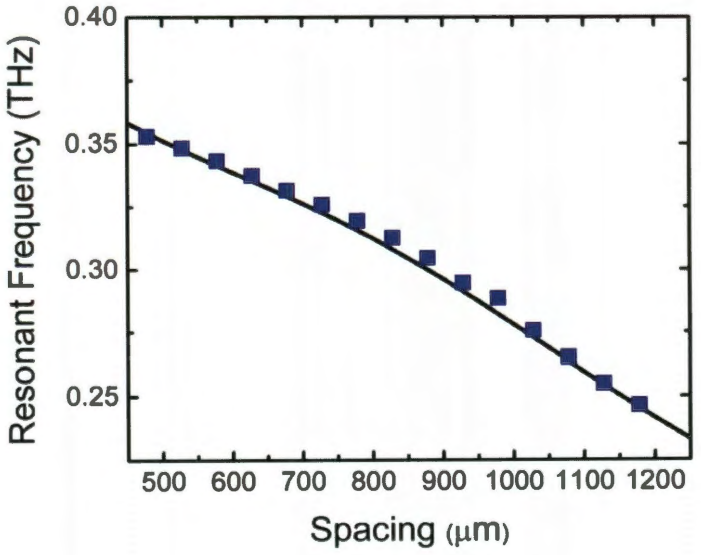

Figure 3-10 Resonant frequency versus waveguide plate separation. As the spacing between waveguide plates decreases, the dominant resonant feature shifts to higher frequencies. Experimental results (blue squares) are compared to results from FEM simulation (black curve) to calibrate the plate spacing.

Another proposed theoretical approach was a Fabry-Perot effect due to the difference in the effective refractive index of the grooved section of the waveguide. The refractive index of a TE_1-mode waveguide is given by the equation:

$$n_{eff} = \frac{c}{v_p} = \sqrt{1 - \left(\frac{f_c}{f}\right)^2} \qquad \textbf{[3-12]}$$

The cutoff frequency is a function of the plate spacing (Equation [3-7]), so the index of the ungrooved waveguide with a spacing of 1 mm will have one effective index, while the grooved section can be treated as a waveguide with a spacing of 1.412 mm and with a different effective index. There will therefore be reflections at the junctions between the grooved and ungrooved sections due to that index difference. Since these reflections are frequency-dependent like the effective indices, interference between these reflections could lead to extinction features in the transmission spectra.

However, a simple simulation test disproves this possibility. If it is only the effective index of the grooved section that is causing the resonance, then a waveguide with one groove of a given depth would have the same resonant frequency as a waveguide with two identical grooves of half that depth on the top and bottom plates (Figure 3-11). A simulation with this geometry clearly shows no visible resonance at all within 20 GHz of the predicted frequency.

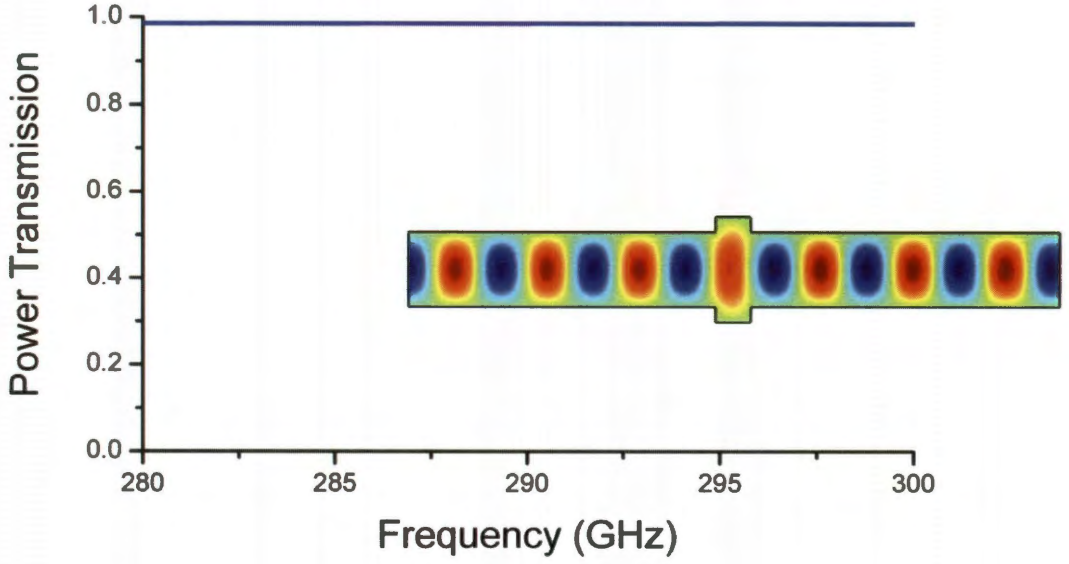

Figure 3-11 Simulated power transmission spectrum for a waveguide with two symmetric grooves of width 460 μm and depth 206 μm on the top and bottom plates. Inset: Electric field pattern inside this waveguide at 290.8 GHz.

While a simple refractive index model was ineffective, the basic idea of the groove as a section of the waveguide became important in developing the analytical explanation of the resonance through a technique known as mode-matching (discussed in detail in Section 3.5.) While the mode-matching analysis was being developed, the simulation results were supplemented by the collection of an extensive experimental data set. To obtain sufficient data to determine the dependence of the resonant frequency on the waveguide geometry, we fabricated a wide range of waveguides and measuring their transmission spectra experimentally. The results of this experimental study are discussed in the following section.

3.4. Experimental Study of the Groove Geometry

To provide a solid framework for the analytical understanding of the origins of this resonance, we required a thorough collection of quantitative experimental data. This led to the fabrication of parallel-plate waveguides with rectangular grooves of a wide range of geometries machined into them. These waveguides were fabricated from aluminum using standard machine shop techniques [5].

The fabricated waveguides fall into two categories: waveguides with grooves of a constant depth but varying width, and waveguides with grooves of a constant width but varying depth. Table 3-1 below lists the fabricated groove geometries, illustrating the wide variety of geometries included in this experiment. Additionally, waveguides with no grooves were fabricated to serve as the reference for calculating the power transmission. All the waveguides had propagation lengths of 5.9 mm with the groove centered midway between the entrance and exit facets. In the transverse direction, the waveguides were 3.2 cm. Compared to an input Gaussian beam of size 12 mm, this large transverse extent ensures that the waveguides are uniform across the entire beam and function as effectively two-dimensional structures.

---

[5] Experimental note: it is important to ensure that the edges of the waveguides are not blunted -- many machinists automatically round off any sharp metal edges on their pieces, but this will lead to problems with the coupling and propagation within the waveguide.

	Depth (μm)	Width (μm)
Set 1	25, 50, 100, 250, 500, 1000, 2500	460
Set 2	406	400, 790, 1500, 1980, 2515, 3000

Table 3-1 List of the groove geometries fabricated for experimental study.

As before, these waveguides are assembled by screwing the top and bottom plates together, with dielectric spacers fixing the plate separation at 1 mm (± 5 μm). They were then placed in the confocal THz-TDS setup described in Section 3.3 above and the data was analyzed as previously described to obtain the power transmission spectra for the various waveguide geometries.

The power transmission spectra for Set 1, waveguides with constant width but varying depth, all show the typical single dominant resonant dip as shown in Figure 3-9 above. As the groove grows shallower (i.e. depth decreases) this feature shifts to higher frequencies, with a corresponding narrowing of the linewidth. Figure 3-12 plots these trends, along with the quality-factor Q that is an expression of the energy concentration of the cavity and the sharpness of the resonance ($Q = f/\Delta f$). Grooves shallower than 100 μm have resonant dips with lower extinction, which allow accurate determination of the center frequency but not the line width, so these grooves are excluded from the linewidth and Q factor plots.

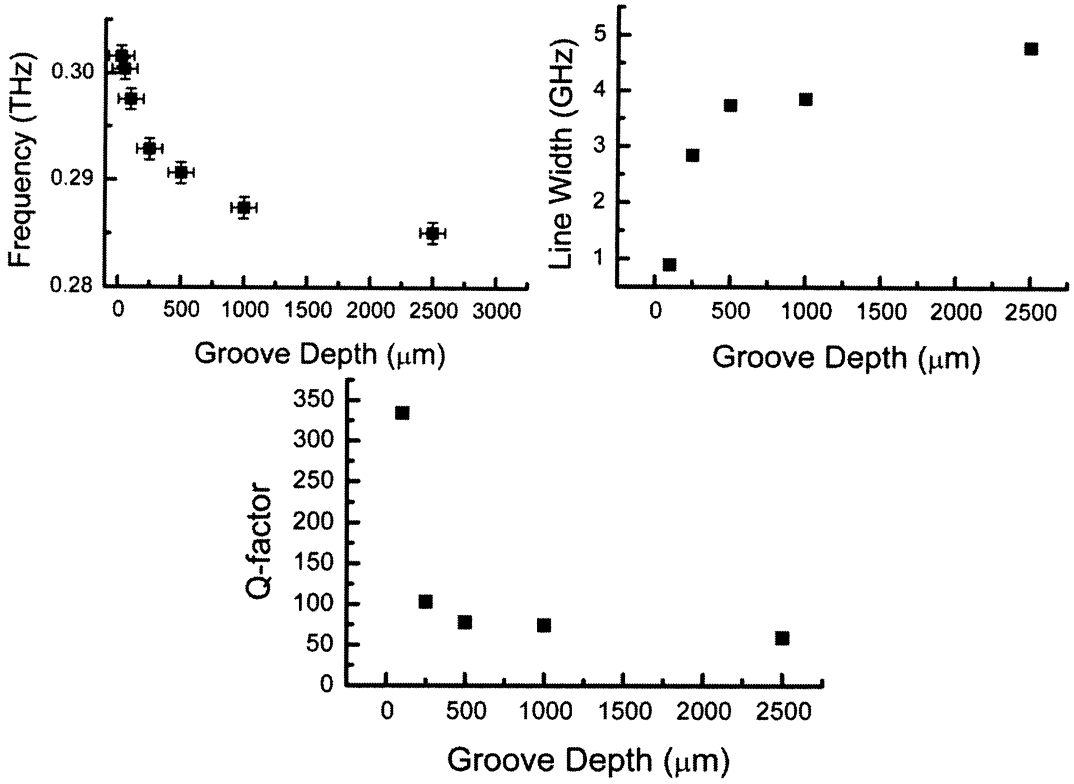

Figure 3-12 Resonant frequency, linewidth, and Q factor produced by rectangular grooves of 460 μm width and varying depth.

The trend observed here, with shallower cavities yielding higher frequencies, narrower resonances, and correspondingly higher Q is intuitively clear. It agrees qualitatively with the predictions of the simple rectangular standing-wave resonator model (as discussed in Section 3.3 above), but the quantitative predictions of that model are so inaccurate that they would barely be visible on these graphs.

The transmission spectra for Set 2, the waveguides with grooves with constant depth but varying width, show a far more complicated dependence on geometry. A collection of the transmission spectra is given in Figure 3-13 below.

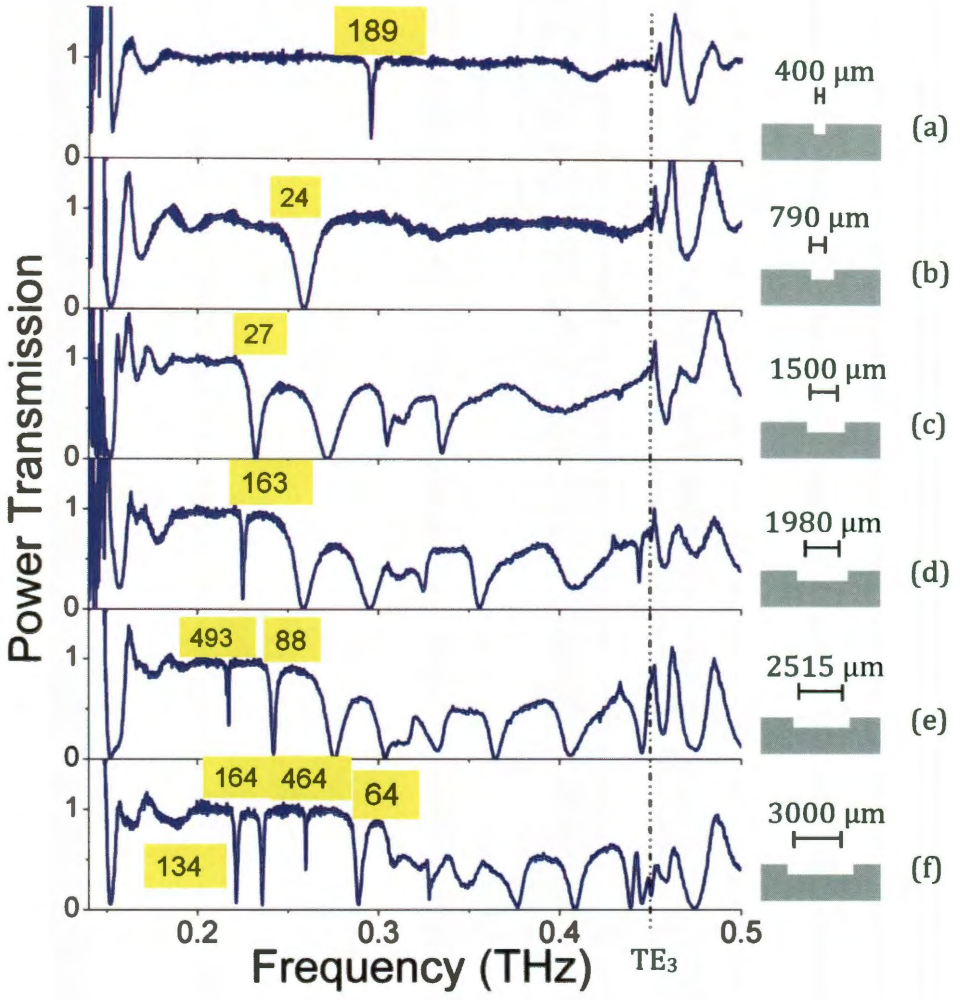

Figure 3-13 Power transmission spectra from PPWGs with rectangular grooves of 406 μm depth and varying width. The width of each groove and a sketch of the waveguide geometry are given to the right of each spectrum. The black dotted line marks the TE_3 cutoff frequency. The yellow boxes contain the Q value measured for the respective resonant feature.

In these spectra, the effect of the cutoff frequency at 150 GHz can clearly be seen, as can the start of multimode propagation above the cutoff for the TE_3 mode at 450 GHz. Between these two frequencies, single-mode TE_1 propagation occurs, and this is the area of primary interest for this work.

For the narrowest groove (Figure 3-13 (a)), there is a single dominant resonant feature as expected, located at 295 GHz. As the groove widens to 790 μm (Figure 3-13 (b)), it seems that this resonant feature both broadens and redshifts. Beyond this width additional resonant features appear, indicating the excitation of higher-order cavity modes. It also appears that several of these features have very narrow linewidths. To explore this quantitatively, the line widths were measured for most of the clearly distinguishable features in the spectra, and the resulting Q factors are presented beside the respective features.

Several of these Q factors are over 100, and the highest is nearly 500. A plot of the narrowest well-shaped feature, the feature marked with a Q of 464 for the waveguide with a 3000 μm by 406 μm groove, is shown in Figure 3-14 (red line). From this plot it appears that the line width is actually less than 0.5 GHz, much lower than the previous lowest-ever recorded THz line width for a resonator [1, 81, 90, 96]. However, this spectrum and most other spectra presented in this thesis have been zero-padded to improve resolution. Zero-padding is a signal processing technique in which a long series of zero values are added as additional data points to the end of a time domain signal prior to Fourier transforming. The effect of these zeros is to increase the spectral resolution of the frequency domain spectra, since

the frequency resolution is inversely proportional to the length of the time window. If the zeros are added after a long time window when the signal has decayed down to the noise floor, no artifacts will be introduced. However, while zero padding is a very useful technique, this increased resolution is artificial. To make claims about extremely narrow linewidths, we should instead depend on the data points present in the original scan. In Figure 3-14, the marked data points are those obtained by Fourier transforming with no zero padding or other manipulation beyond the inherent windowing. It is clear from these points that the linewidth is indeed very narrow (less than 1 GHz), but due to the resolution limit of the measurement technique we cannot be entirely confident of the exact value.

While there are many high-quality features evident in these spectra, there is no obvious trend in the frequencies or line widths, complicating the attempt to quantify the dependence on geometry. To understand this complex behavior, we use a mode-matching analysis based on classical waveguide theory. This analysis is discussed in detail in the following section.

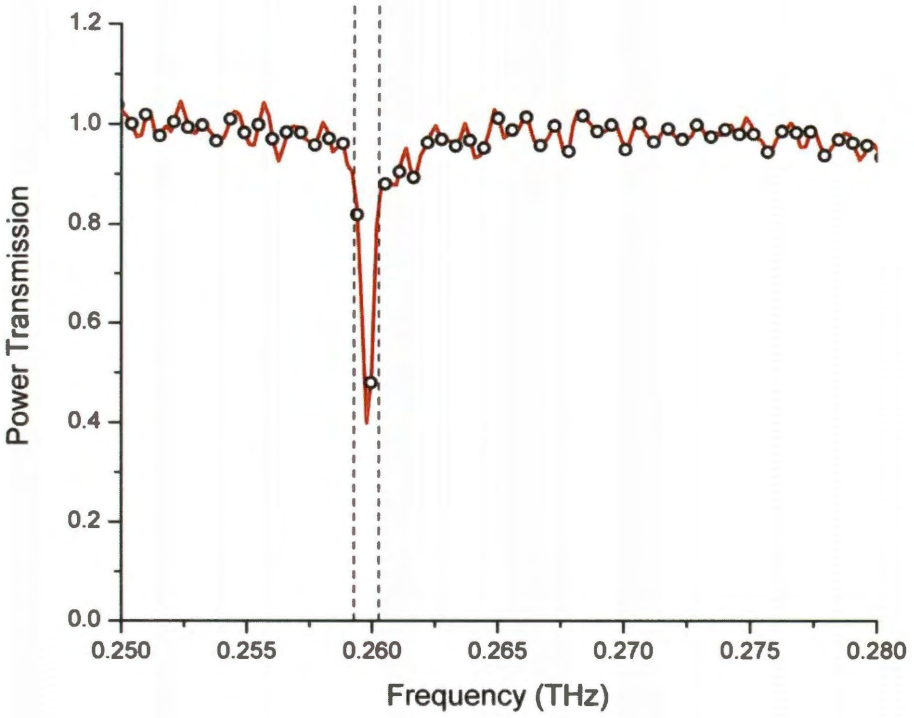

Figure 3-14 Power transmission plot for the highest-Q feature in the experimental data set. The open circles mark the original data points. The red line is the result when the original data has been zero-padded. Dotted lines mark a 1 GHz linewidth.

3.5. Mode-Matching Theory

3.5.1. Scattering Matrix

The mode-matching method is a form of analysis employing waveguide theory and the generalized scattering matrix technique to analyze transmission through waveguides with features such as changes in size, divisions, cavities, etc [88, 97-100]. The technique is discussed in detail in Ref. [97] and in Chapters 9 and

10 of Ref. [100]. In the case of a structure like the grooved waveguide we are investigating here, the groove is treated as if it is a section of PPWG with a different plate separation and with its own supported modes. An incoming wave propagates through the ungrooved section, and then at the junction the wave is either transmitted into the various modes of the wider grooved section or reflected back into the ungrooved section. The transmitted waves propagate through the grooved section, before being transmitted or reflected at the junction with the second ungrooved section. For example, in the illustration below, the A+ wave represents all of the incident propagating modes. These waves reach the junction and are reflected (A- modes) or transmitted (B+ modes) into the next section. The B+ modes propagate to the next junction, where they are again transmitted (C+) or reflected (B-). The transmitted waves continue to the next junction, while the reflected modes propagate back to the first junction and are transmitted or reflected again, and so on.

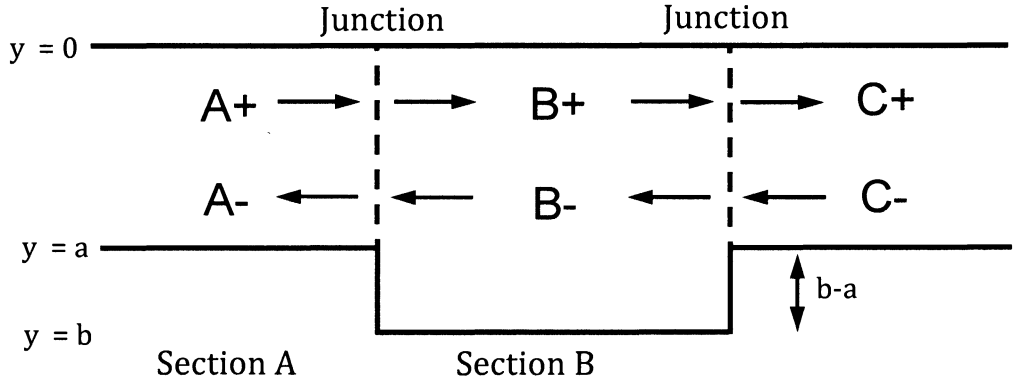

Figure 3-15 Diagram of the grooved waveguide for mode-matching analysis. Forward (+) and backward (-) propagating waves in each section are labelled.

Mathematically, this process is represented through a scattering matrix.

$$\begin{pmatrix} A^- \\ B^+ \end{pmatrix} = \begin{pmatrix} S_{11} & S_{12} \\ S_{21} & S_{22} \end{pmatrix} \cdot \begin{pmatrix} A^+ \\ B^- \end{pmatrix} \quad \textbf{[3-13]}$$

The scattering matrices for each junction and propagation section will combine (the mathematics of this are described in the next section) to create one overall scattering matrix that expresses how all the modes are transmitted and reflected through the waveguide as a whole.

$$\begin{pmatrix} A^- \\ C^+ \end{pmatrix} = \begin{pmatrix} U_{11} & U_{12} \\ U_{21} & U_{22} \end{pmatrix} \cdot \begin{pmatrix} A^+ \\ C^- \end{pmatrix} \quad \textbf{[3-14]}$$

Each of these variables – A+, B+, B-, etc. – is in fact a vector, representing the amplitudes of all the modes propagating in that waveguide section. For example, the electric field pattern in the initial waveguide section can be expressed as the sum of all the forward (+) and backward (-) propagating modes in Section A of the waveguide.

$$E_x = \sum_{n=1}^{K} (a_n^+ + a_n^-)\Phi_n \quad \textbf{[3-15]}$$

For the TE-mode waveguide we are discussing here, Φ simply represents the normalized modal fields of the TE propagating modes, given by the equation presented in Section 3.2 above:

$$\Phi_n = \sqrt{\frac{2}{a}} \sin\left(\frac{n\pi y}{a}\right) \qquad \textbf{[3-16]}$$

where a is the plate spacing in this particular section of the waveguide. (It would be b in Section B of the waveguide).

The variable A+ is simply the vector composed of the amplitudes a_n^+ of all these modes.

$$A^+ = \begin{pmatrix} a_1^+ \\ \vdots \\ a_n^+ \end{pmatrix} \qquad A^- = \begin{pmatrix} a_1^- \\ \vdots \\ a_n^- \end{pmatrix} \qquad \textbf{[3-17]}$$

We are primarily interested in frequencies for which there is single-mode TE_1 propagation in the ungrooved waveguide sections, so the incident wave can be represented as:

$$A^+ = \begin{pmatrix} 1 \\ 0 \\ 0 \\ 0 \\ \vdots \end{pmatrix} \qquad \textbf{[3-18]}$$

For most applications we can assume that there is only an incident wave from one direction, so B- is an empty vector, [0, 0, 0...].

With these values, we can use the scattering matrix S to solve Equation [3-13] to obtain values for the amplitudes of the various modes that are reflected (A-) or transmitted (B+).

Because A+, A-, etc. are vectors, each component of the scattering matrix is itself also a matrix. S_{11} is the matrix that relates the incident wave to the reflected wave, and each component of this matrix $S_{11}(m,n)$ represents the amplitude of the nth incident mode reflected into the mth mode. S_{21}, in turn, is the matrix that relates the incident wave to the transmitted wave. The transmission from the TE_1 mode of the ungrooved section to the TE_1 mode of the grooved section is expressed by the component $S_{21}(1,1)$.

$$A^- = S_{11}A^+ \qquad \textbf{[3-19]}$$

$$\begin{pmatrix} a_1^- \\ a_2^- \\ \vdots \\ a_n^- \end{pmatrix} = \begin{pmatrix} S_{11}(1,1) & \cdots & S_{11}(1,n) \\ \vdots & \ddots & \vdots \\ S_{11}(n,1) & \cdots & S_{11}(n,n) \end{pmatrix} \begin{pmatrix} a_1^+ \\ a_2^+ \\ \vdots \\ a_n^+ \end{pmatrix} \qquad \textbf{[3-20]}$$

The term "mode-matching technique" more accurately refers to the method used to obtain the actual elements of this scattering matrix S. Simply put, the amount of energy transferred from one mode to another by reflection or transmission is dependent on two things: the impedance mismatch between the

modes, and the amount of spatial overlap between the mode patterns. Modes with very similar electric field patterns will have a large spatial overlap and a correspondingly greater likelihood of coupling, while modes with very different patterns will have a smaller overlap. If there is a large impedance mismatch at a boundary, energy is more likely to be reflected, while a small impedance mismatch leads to increased transmission.

These intuitive relationships are expressed through the equations for the components of the scattering matrix S, which are defined as functions of several matrices: Y_1, Y_2, and M. These are derived from the equations specifying the continuity of the electric and magnetic fields at the junction, discussed in detail in Ref. [97].

Y_1 and Y_2 are impedance matrices for the modes of Section A and Section B, respectively. The impedance for each TE mode in the waveguide is given by:

$$Z = \frac{\omega\mu_0}{\beta_z} = \frac{\sqrt{\mu_0/\varepsilon_0}}{\sqrt{1-\left(f_c/f\right)^2}} \qquad \textbf{[3-21]}$$

where f_c is the cutoff frequency for that mode in that section of the waveguide, as described in Section 3.2 above.

These impedances can be arranged in a vector, just as the mode amplitudes were, and then used to generate the impedance matrix Y using the equation below.

Y is a diagonal matrix, where the (*m,m*) element is the inverse of the impedance of the *m*th mode in that particular section of the waveguide.

$$Y = \begin{pmatrix} {}^{1}/_{Z_1} & 0 & \cdots & 0 \\ 0 & {}^{1}/_{Z_2} & & \\ \vdots & & \ddots & \\ 0 & & & {}^{1}/_{Z_n} \end{pmatrix} \qquad \textbf{[3-22]}$$

The last required matrix, M, is the mode overlap matrix. Each (*m,n*) component of M represents the similarity in the electric field patterns between the *m*th reflected or transmitted mode and the *n*th incident mode. This is calculated from the overlap integral of the relevant mode patterns:

$$M(m,n) = \int_0^a \Phi_{1n}\Phi_{2m}\, dy \qquad \textbf{[3-23]}$$

For example, in the TE-mode waveguide we are discussing, the overlap integral for the *n*th mode in Section A transmitted into the *m*th mode of Section B takes the form:

$$M(m,n) = \sqrt{\frac{4}{ab}} \int_0^a \sin\left(\frac{n\pi y}{a}\right) \sin\left(\frac{m\pi y}{b}\right) dy \qquad \textbf{[3-24]}$$

The limits of integration are from the top plate of the waveguide ($y = 0$) to the bottom plate of the ungrooved section ($y = a$). The mode patterns in the ungrooved

waveguide are zero beyond $y= a$, so the region from $y=a$ to $y=b$ is irrelevant to the integral. Due to the simple form of the mode patterns in this case, analytical solutions to these overlap integrals are possible, but for more complex patterns, numerical integration is sometimes necessary.

In addition to these matrices, an additional matrix Y_x is calculated, where $Y_x = M' \cdot Y_2 \cdot M$. This matrix has no physical significance but is useful in simplifying later equations. (M′ is the transpose of the matrix M.)

From the impedance and mode overlap matrices, the scattering matrix can then be calculated using the following relationships:

$$S_{11} = (Y_x + Y_1)^{-1} \cdot (Y_1 - Y_x) \quad \textbf{[3-25]}$$

$$S_{12} = 2(Y_1 + Y_x)^{-1} \cdot M' \cdot Y_2 \quad \textbf{[3-26]}$$

$$S_{21} = M \cdot (I + S_{11}) \quad \textbf{[3-27]}$$

$$S_{22} = M \cdot S_{12} - I \quad \textbf{[3-28]}$$

And from this scattering matrix we can then pull out the individual elements that give the transmission or reflection into a particular mode of the waveguide. $S_{21}(1,1)$ for TE_1 transmission, $S_{11}(1,1)$ for TE_1 reflection, $S_{21}(2,1)$ for TE_1 to TE_3 transmission, etc.

3.5.2. Transmission Through the Entire Waveguide

The scattering matrix only describes the energy transfer at a junction, such as that between the grooved and ungrooved sections of the waveguide. In order to fully describe the entire waveguide, we need to consider the propagation of the waves between junctions, and also to include the scattering matrices from later junctions.

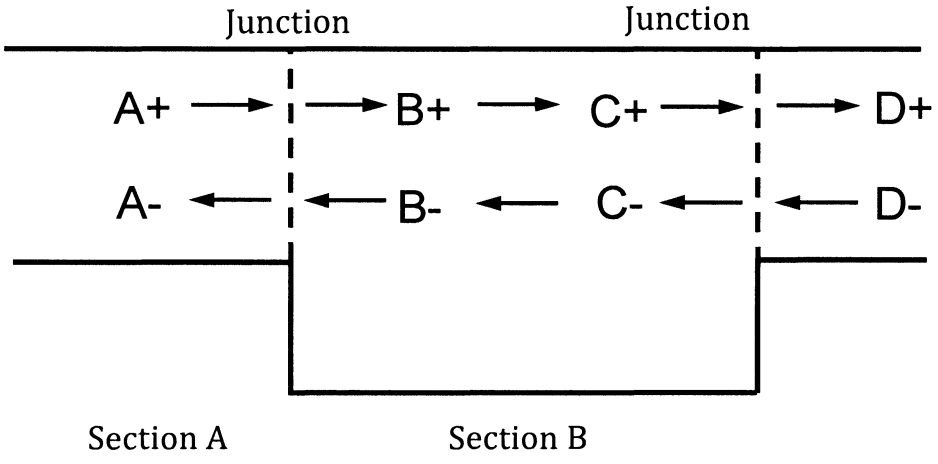

Figure 3-16 Diagram of the grooved waveguide, showing the modes before and after propagation through Section B of the waveguide (the groove itself).

The propagation of the various modes in a waveguide from one junction to the next is calculated with a transmission matrix. As before, the incident transmitted waves are considered as vectors of the amplitudes of all the modes.

$$\begin{pmatrix} B^- \\ C^+ \end{pmatrix} = \begin{pmatrix} T_{11} & T_{12} \\ T_{21} & T_{22} \end{pmatrix} \cdot \begin{pmatrix} B^+ \\ C^- \end{pmatrix} \quad \textbf{[3-29]}$$

The propagating waves will not change direction or change modes over a flat waveguide section, so the matrices T_{11} and T_{22} are zero, while T_{12} and T_{21} are identical diagonal matrices whose nonzero components are simply an expression of the change in phase due to propagation over the length of the waveguide section.

$$T_{12} = T_{21} = \begin{bmatrix} e^{i\beta_1 z} & 0 & \cdots & 0 \\ 0 & e^{i\beta_2 z} & & \\ \vdots & & \ddots & \\ 0 & & & e^{i\beta_n z} \end{bmatrix} \quad \textbf{[3-30]}$$

In this expression, β represents the phase constant in the z-direction for the given mode, $\beta_z = \sqrt{\left(\frac{2\pi}{\lambda}\right)^2 - \left(\frac{n\pi}{b}\right)^2}$, where b is the spacing of the waveguide section and λ is the wavelength, as described in Equations [3-4] to [3-6] in Section 3.2 above.

To combine the scattering and transmission matrices, we solve Equations [3-13] and [3-29] relating the overall input and output waves to obtain one overall transfer matrix as shown in Equation [3-14].

Solving these equations yields the following expressions for the transfer matrix:

$$U_{11} = S_{11} \quad \textbf{[3-31]}$$

$$U_{12} = S_{12} \cdot T_{12} \quad \textbf{[3-32]}$$

$$U_{21} = T_{21} \cdot S_{21} \quad \textbf{[3-33]}$$

$$U_{22} = T_{21} \cdot S_{22} \cdot T_{12} \quad \textbf{[3-34]}$$

These equations are true when combining a scattering matrix and a transmission matrix in which several of the elements are zero. It is also possible to obtain equations for a general case, in which two matrices of any sparsity can be combined to generate the overall transfer matrix.

$$\begin{pmatrix} E^- \\ F^+ \end{pmatrix} = \begin{pmatrix} W_{11} & W_{12} \\ W_{21} & W_{22} \end{pmatrix} \cdot \begin{pmatrix} E^+ \\ F^- \end{pmatrix} \quad \textbf{[3-35]}$$

$$\begin{pmatrix} F^- \\ G^+ \end{pmatrix} = \begin{pmatrix} V_{11} & V_{12} \\ V_{21} & V_{22} \end{pmatrix} \cdot \begin{pmatrix} F^+ \\ G^- \end{pmatrix} \quad \textbf{[3-36]}$$

$$\rightarrow \begin{pmatrix} E^- \\ G^+ \end{pmatrix} = \begin{pmatrix} U_{11} & U_{12} \\ U_{21} & U_{22} \end{pmatrix} \cdot \begin{pmatrix} E^+ \\ G^- \end{pmatrix} \quad \textbf{[3-37]}$$

$$U_{11} = W_{11} + W_{12}(I - V_{11}W_{22})^{-1}V_{11}W_{21} \quad \textbf{[3-38]}$$

$$U_{12} = W_{12}(I - V_{11}W_{22})^{-1}V_{12} \quad \textbf{[3-39]}$$

$$U_{21} = V_{21}(I - W_{22}V_{11})^{-1}W_{21} \quad \textbf{[3-40]}$$

$$U_{22} = V_{21}(I - W_{22}V_{11})^{-1}W_{22}V_{12} + V_{22} \quad \textbf{[3-41]}$$

This procedure is referred to as the "star product" of the W and V matrices. Additional scattering or transmission matrices can be added in the same way, for example by taking the star product of the matrix U above and the scattering matrix for the next junction. This process continues for each groove, junction or other feature until finally an overall transfer matrix U is obtained.

This overall transfer matrix expresses the overall transmission and reflection of various modes for the waveguide as a whole. $U_{21}(1,1)$ gives the transmission of the TE_1 mode through the entire waveguide, $U_{11}(1,1)$ gives the TE_1 reflection, and so forth. These values are dependent on frequency, and so the procedure above must be repeated for a wide range of frequencies to obtain a picture of the resonant behavior of the grooved waveguide. Figure 3-17 below plots of the $U_{21}(1,1)$ and $U_{11}(1,1)$ matrix elements, showing the transmission and reflection versus frequency for the TE_1 mode in a basic grooved waveguide geometry.

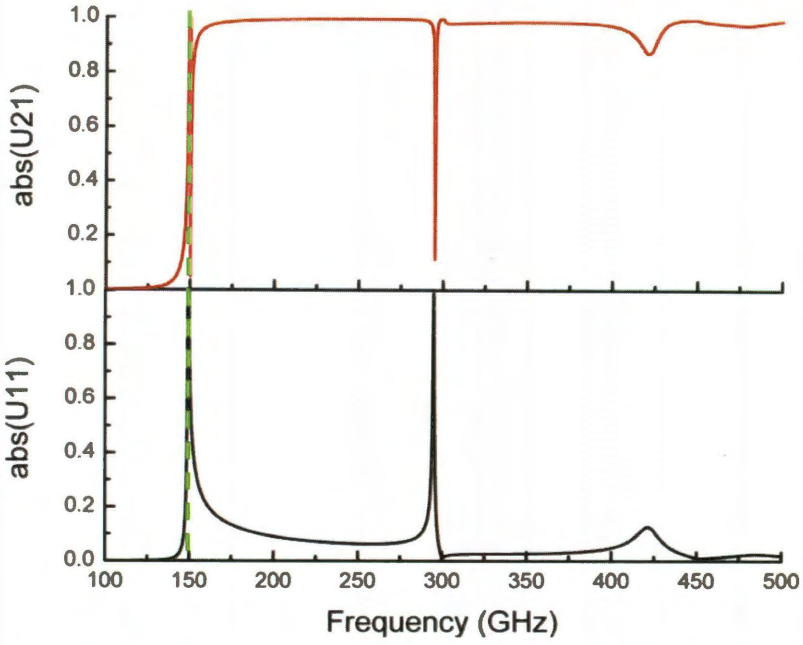

Figure 3-17 Plot of the absolute values of the $U_{21}(1,1)$ (top) and $U_{11}(1,1)$ (bottom) matrix elements. The green dashed line indicates the TE_1 cutoff frequency.

It is clear from this figure that the dip in the transmission plot is matched by a spike in the reflection plot, indicating that the resonance arises from the TE_1 mode being reflected back.

In practice, this process can be automated as a MATLAB script to calculate the transfer matrix for any given geometry. An annotated copy of the MATLAB code is included in Appendix A.

3.5.3. Comparison to Experiment

Once the mode-matching technique has been used to model the grooved waveguide, we can compare the results to the experimental data given in Section 3.4

above. As stated above, in the frequency range between the cutoffs for the TE_1 (150 GHz) and TE_3 (450 GHz) modes, propagation in the waveguide is assumed to be single-mode, and so it is the TE_1-to-TE_1 transmission element of the transfer matrix that we plot for comparison ($U_{21}(1,1)$). This element is amplitude transmission and so must be squared for comparison to the power transmission experimental plots.

Figure 3-18 below shows just such a comparison between experimental data and mode-matching results for Set 2, the waveguides with constant depth and varying width. In the single-mode propagation regime, the agreement between theory and experiment is excellent. Mode-matching analysis successfully reproduces all the many resonant features with their corresponding linewidths, along with some very fine features that are not fully resolvable in the experimental data.

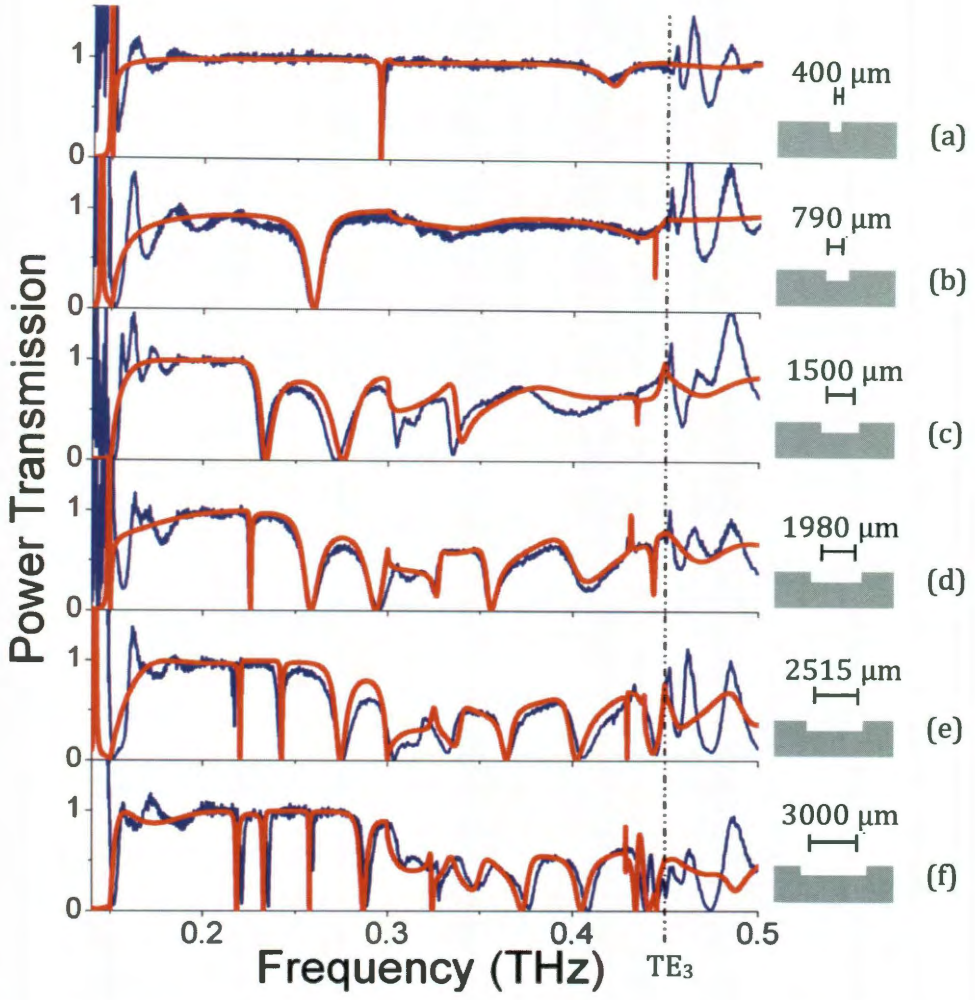

Figure 3-18 Power transmission spectra from PPWGs with rectangular grooves of 406 μm depth and varying width. Blue curves are experimental results and red curves are the results from mode-matching analysis, showing excellent agreement. The width of each groove and a sketch of the waveguide geometry are given to the right of each spectrum. The black dotted line marks the TE_3 cutoff frequency.

Due to the outstanding agreement observed here, we confidently conclude that mode-matching analysis is an effective analytical model for explaining the origin of the resonances from the grooved waveguide.

When the results of mode-matching analysis are compared to the experimental data for Set 1, the waveguides with constant width but varying depth, mode-matching also produces the single dominant resonant features observed experimentally. When the resonant frequencies, linewidths, and quality factors are compared quantitatively (Figure 3-19), reasonably good agreement is observed between theory and experiment.

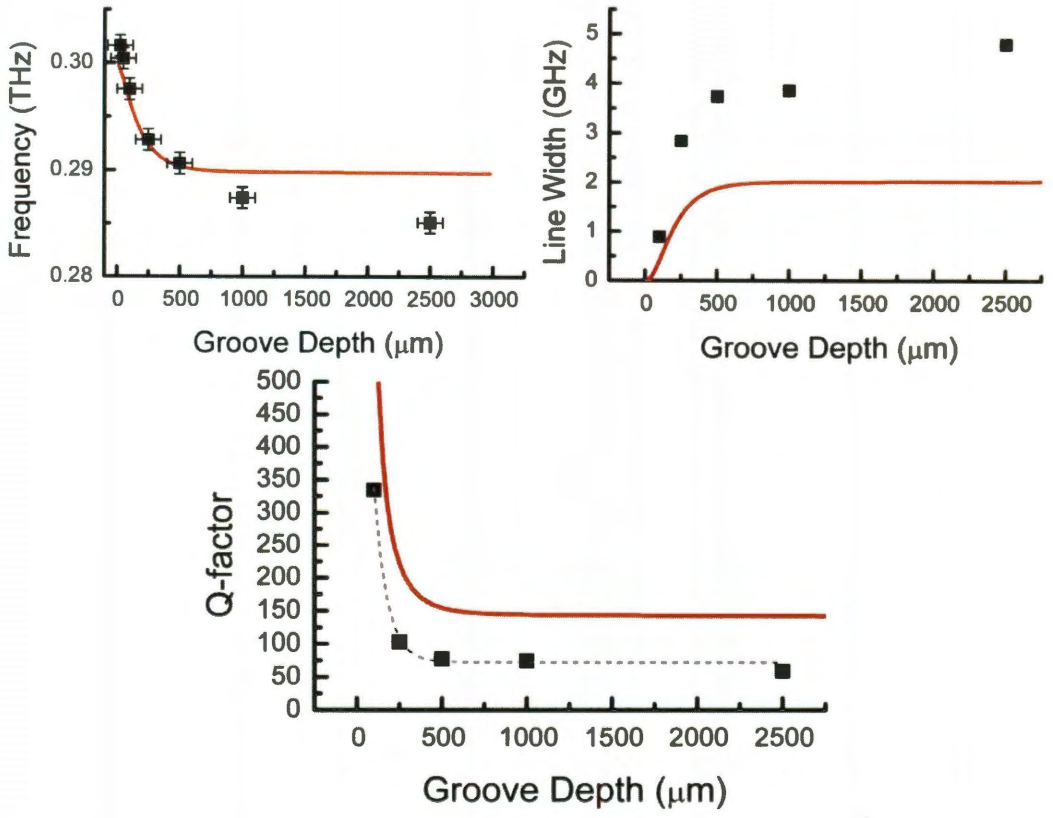

Figure 3-19 Resonant frequency, linewidth, and Q factor produced by rectangular grooves of 460 μm width and varying depth. Black squares are experimental data. The red lines are the results from mode-matching analysis. The black dotted line in the bottom figure is an exponential fit to the experimental data.

The resonant frequencies agree very well for depths shallower than 1000 μm but become less accurate as the groove deepens. Also, in order to obtain even this level of accuracy, a very large number of modes were required in the calculation. For most of the results given above such as Figure 3-18, only 4-6 modes in both grooved and ungrooved waveguide sections were required to obtain very accurate results; for the plot above, over 100 modes were required to reach convergence.

This reflects the fact that for very deep grooves, the model of the groove as a waveguide section becomes less accurate. FEM simulation images of the electric field at the resonant frequency for two groove depths illustrate this well (Figure 3-20). For a groove with a depth of 412 μm, the field fully penetrates the groove (inset). But for a groove with a depth of 2500 μm, the electric field does not come close to reaching the bottom of the groove, making the assumption required by mode-matching analysis – the assumption that the wave propagates in this section as though it were a waveguide of width 2500 μm – invalid.

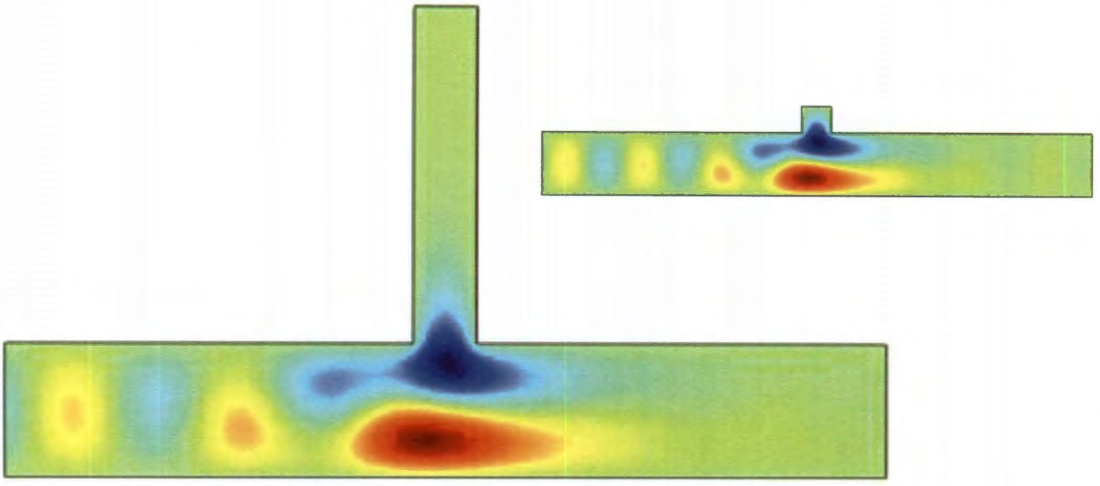

Figure 3-20 FEM simulation images of the electric field pattern at the resonant frequency in a waveguide with a groove of dimensions 460 x 2500 μm. It is clear that the field does not fully penetrate the groove. Inset: the field pattern for a waveguide with a groove of dimensins 460 x 412 μm for comparison.

The line width and quality factors as shown in Figure 3-19 also suffer from a lack of quantitative agreement, though the trends agree well qualitatively. Most likely this is due to losses in the cavity that are not considered in the theory, or imperfections in the fabrication, or simply the lack of spectral resolution necessary to truly characterize very narrow resonances. The predicted linewidths are all ≤ 2 GHz, which is difficult to resolve with a system with a maximum resolution of 0.6 GHz.

The final comparison to theory is the variation in waveguide spacing (Figure 3-21). As with the waveguides of varying depth, the mode-matching results agree well for the original waveguide geometry, but become less accurate as the geometry varies. As the simulation image in Figure 3-22 below illustrates, again the model of

the groove as a waveguide section becomes less accurate as the junction between sections represents an increasingly abrupt change in effective plate spacing.

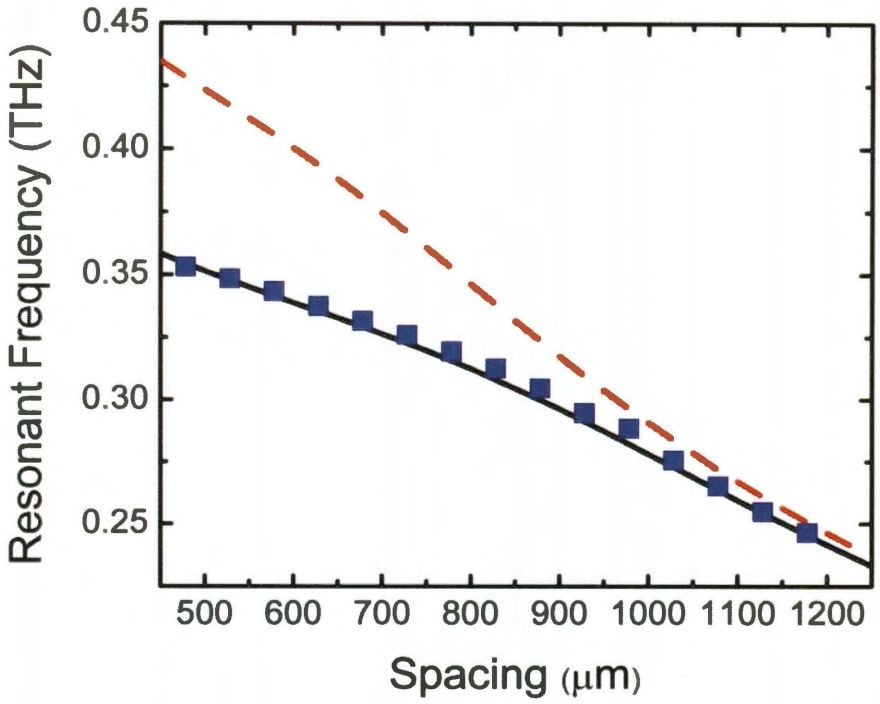

Figure 3-21 Resonant frequency versus waveguide plate separation. As the spacing between waveguide plates decreases, the dominant resonant feature shifts to higher frequencies. Comparison of experimental results (blue squares) to results from FEM simulation (solid black curve) and mode-matching analysis (dotted red curve).

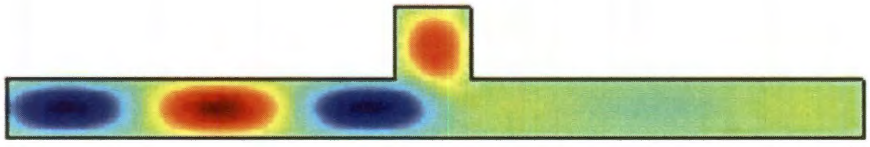

Figure 3-22 FEM simulation of the electric field pattern at resonance for a waveguide with a plate spacing of 450 μm, illustrating the abruptness of the junction between waveguide sections.

The conclusion drawn from these comparisons is that the mode-matching analysis is an effective model for the grooved waveguide, provided the underlying assumption that the groove can be treated as a waveguide section with its own propagating modes is a valid one. For more abrupt junctions or extreme geometries, an alternate model (or finite element method simulation) would be required.

As a final note, while mode-matching analysis provides an accurate method for computing the transmission spectra for grooved waveguides along with a useful physical model for understanding the resonant features (as the result of the combination of various reflections and transmissions at junctions between waveguide sections), it is possible that a more directly physical interpretation of these resonances may be developed. For example, the asymmetric appearance of several of the resonant features in Figure 3-18 seems to indicate Fano resonances. Fano resonances result from the interference between a discrete resonance and the modes of a continuum and are characterized by an asymmetric line shape [101-104]. In the case of the grooved parallel-plate waveguide, this could be interpreted as interaction between the waveguide modes and the cavity resonance, or possibly as the broad resonance of a wide groove interacting with higher-order cavity modes within that groove. Interpreting the experimental transmission spectra through the Fano resonance paradigm may provide a fruitful avenue for future work in understanding the origins of the resonant behavior of the grooved parallel-plate waveguide.

3.6. Two Grooves

With the previous work establishing the grooved waveguide as a microfluidic sensor with high sensitivity [1], an obvious next step is to expand the sensor to multichannel operation by the inclusion of two or more grooves with independent resonances. If the resonances are well separated in frequency and the grooves are well separated spatially on the waveguide, each groove should respond independently to a liquid fill with a shift in its own (and only its own) resonant frequency. In this way, each groove acts as a separate sensing channel for multiplexing applications, and the design and performance of one such sensor is described in Section 3.6.1 below.

In contrast, if grooves are not sufficiently separated spatially and/or if the resonances are not separated in frequency, coupling between grooves will occur. While it precludes the use of each groove as a separate channel, this coupling does lead to an interesting resonant splitting effect with its own potential applications, discussed in Section 3.6.2 below.

3.6.1. Multichannel Sensor

The initial work in developing the multichannel sensor was performed through finite element method simulation. Each geometry was modeled, the resonant frequency or frequencies were determined, and an image of the electric

field at resonance was obtained, to verify that each resonance arises only from one groove to ensure independent multichannel operation.

In designing the multichannel sensor, we selected grooves with resonances that were well separated in frequency as determined from the width-parameter tests described in Section 3.4 above. Based on Figure 3-13, we chose one groove of width 460 μm and depth 412 μm (resonance at 290.8 GHz) and a second groove of width 700 μm and depth 412 μm (resonance at 266.4 GHz) as being sufficiently separate resonances. To prevent coupling, the two grooves were separated by 2.08 mm in a waveguide of total length 8.5 mm.

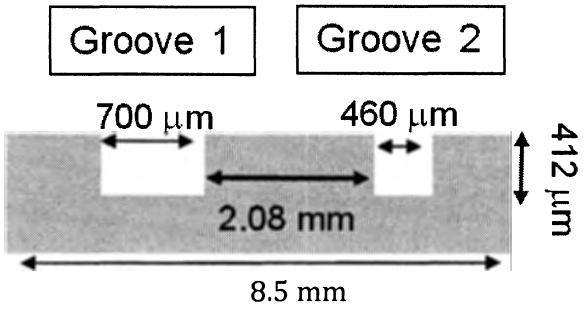

Figure 3-23 Diagram of the multichannel waveguide geometry.

The simulated power transmission spectra in Figure 3-24 below show the resonant response of a waveguide containing only the first groove (red), a waveguide containing only the second groove (green), and the two-groove waveguide containing both (blue), illustrating that both resonant responses are present without any significant coupling effects.

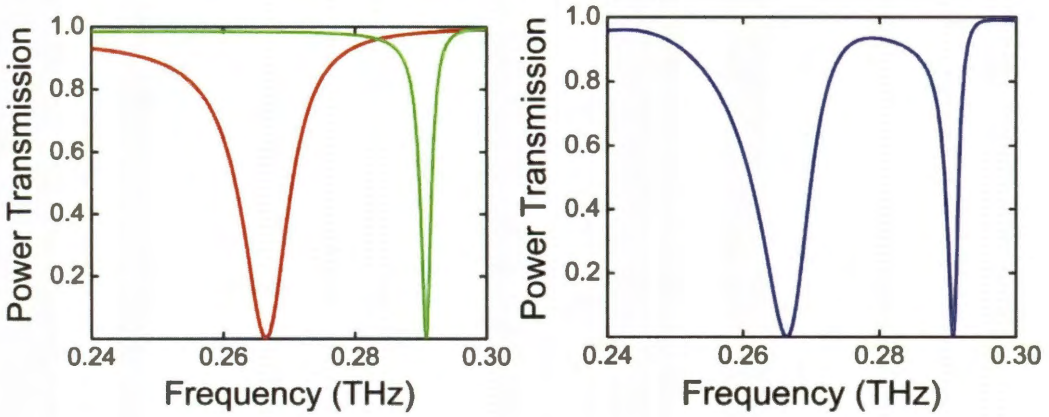

Figure 3-24 Power transmission spectra from FEM simulation of the response of (left) a waveguide with one 460 x 412 μm groove (green curve) superimposed with that of a waveguide with one 700 x 412 μm groove (red curve) , and (right) a waveguide with both grooves. The superimposition of the two resonant responses with no coupling between grooves is clear.

The independence of these resonances can be confirmed by looking at the electric field pattern within the grooves at each resonant frequency. At the 266.4 GHz resonance, the electric field is concentrated heavily in the 700 μm groove, with no contribution from the 460 μm groove. At the 290.8 GHz resonance, the reverse is true, with an electric field pattern that shows that only the 460 μm groove is contributing to the resonance. This confirms that the two groove resonances are independent, and supports the possibility of a multichannel sensing application.

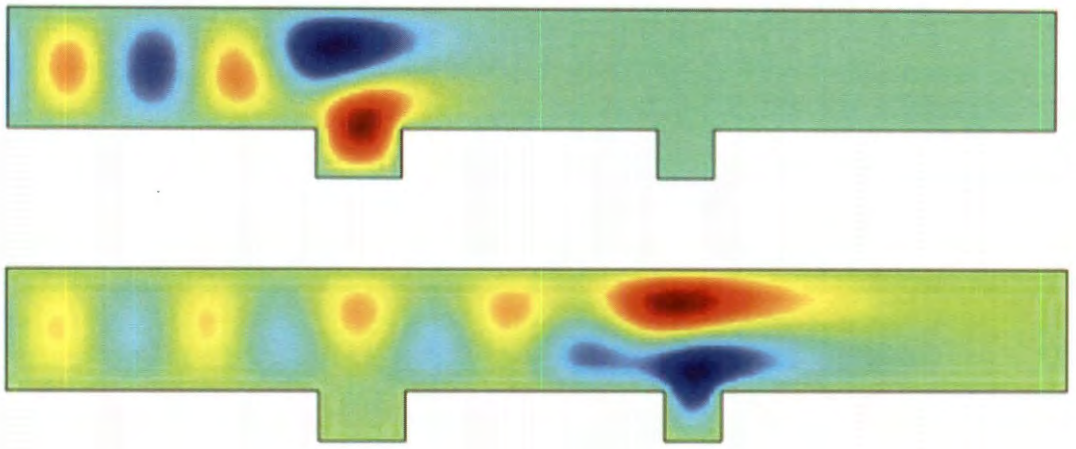

Figure 3-25 FEM plots of the electric field pattern inside the two-groove waveguide at resonant frequencies 266.4 GHz (top) and 290.8 GHz (bottom), showing how each resonance clearly arises from only one groove.

This design was fabricated and the transmission was measured experimentally, using the procedure detailed previously in Section 3.3. The experimentally measured power transmission (Figure 3-26 below, red line) matches the simulations excellently, with only a slight difference in the predicted resonant frequencies (265.0 GHz and 290.2 GHz). This is due to the imprecision inherent to machine fabrication, which we estimate gives a final geometry for the grooves of 711 by 406 μm and 457 by 406 μm. For comparison, mode-matching analysis was used to generate a prediction of the power transmission for this experimental geometry (Figure 3-26, blue line) with excellent agreement. The resonant frequencies and linewidths are compared quantitatively in Table 3-2.

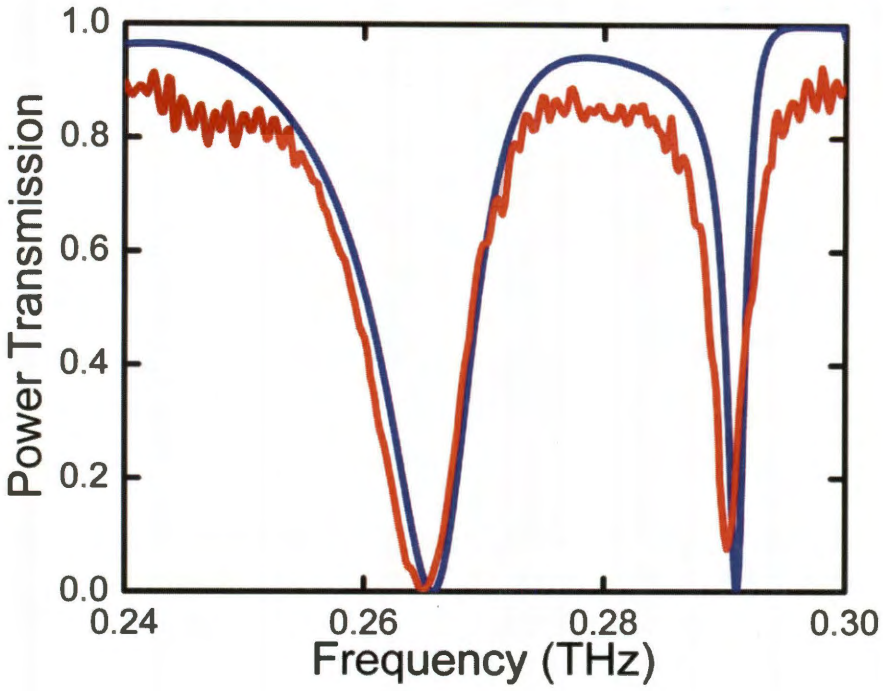

Figure 3-26 Power transmission of the multichannel waveguide, both experimental (red) and from mode-matching analysis (blue).

	Frequency 1	Linewidth 1	Q1	Frequency 2	Linewidth 2	Q2
Experiment	265.0	8.3	32	290.2	3.3	88
Mode-Matching	265.7	9.0	29	291.0	1.9	153

Table 3-2 Quantitative comparison of resonant frequencies (in GHz), linewidths (in GHz) and quality-factors for the experimental and mode-matching analysis results for the multichannel waveguide.

Over the course of several experimental data sets, we observe that the resonant frequencies are consistent, with a standard deviation $\sigma_1 = 1.65$ GHz for the first resonance and $\sigma_2 = 1.17$ GHz for the second resonance. Therefore the experiment and mode-matching results agree to within experimental error.

This error is due to slight variations in the plate spacing when the waveguide is disassembled and reassembled between data sets. As Section 3.3 shows, small variations in the plate spacing will shift the resonant frequencies. A variation of ~1 GHz corresponds to a spacing variation of a few microns.

These results support the prediction from simulation and mode-matching analysis that two grooves may be incorporated into a waveguide with no coupling, indicating that this waveguide design has potential as a multichannel sensor. This application is discussed in detail in Section 3.7 Liquid Filling.

3.6.2. Resonant Splitting

Above were discussed the results when the two grooves are independent, well-separated spatially and with well-separated resonant frequencies. If those two conditions are not met, the two grooves will not be independent. Instead, they exhibit coupling, which can have an interesting effect on the observed resonant behavior of the grooves, and in some cases can produce a distinct resonant splitting effect.

For example, we consider the case where the two grooves have the same geometry. If two grooves of geometry 460 x 412 μm are included on an 8.5 mm long waveguide, the shape of the resonant feature is distorted, even with 3 mm separating the grooves (Figure 3-27). The electric field pattern at the primary resonant frequency (290.6 GHz, top image) shows some energy concentration in the

second groove, indicating an interaction or coupling between resonant cavities despite the large separation. One effect of this coupling is a tiny secondary peak or shoulder in the transmission spectrum at 291.4 GHz (marked with an arrow, bottom image). The electric field pattern at this frequency shows that energy is concentrated almost evenly in the two grooves, with a small predominance in the second groove, indicative of coupling between the two.

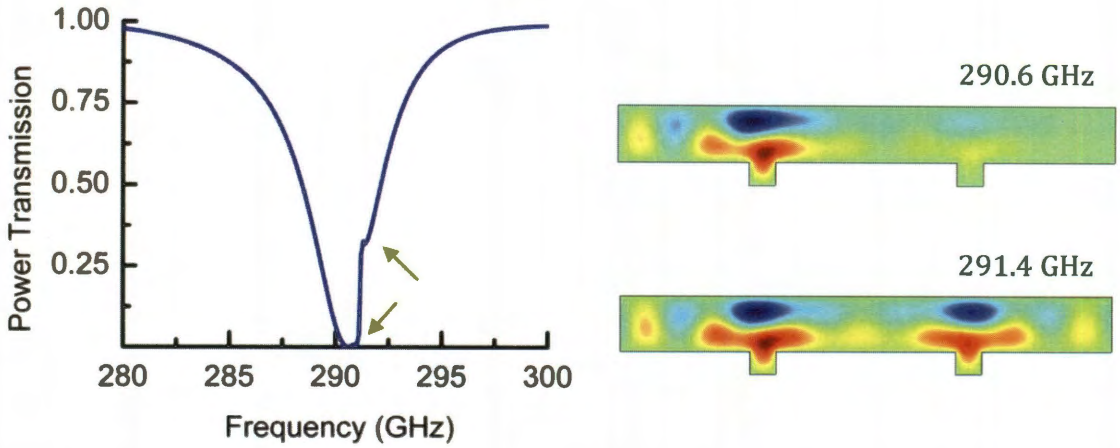

Figure 3-27 Power transmission and electric field patterns from FEM simulation for a two-groove waveguide with 3 mm separation between the grooves. The field patterns are obtained at the primary resonant frequency (290.6 GHz) and the secondary peak (291.4 GHz) marked with arrows in the transmission spectrum.

A series of simulations were performed with the separation between the two grooves gradually decreasing (Figure 3-28 below). It is clear that as separation decreases, the coupling grows stronger, and the power transmission evolves in a complicated way. At longer separations, there is one prominent resonant feature, with a secondary shoulder or peak indicating a second resonance (Figure 3-28 (b)).

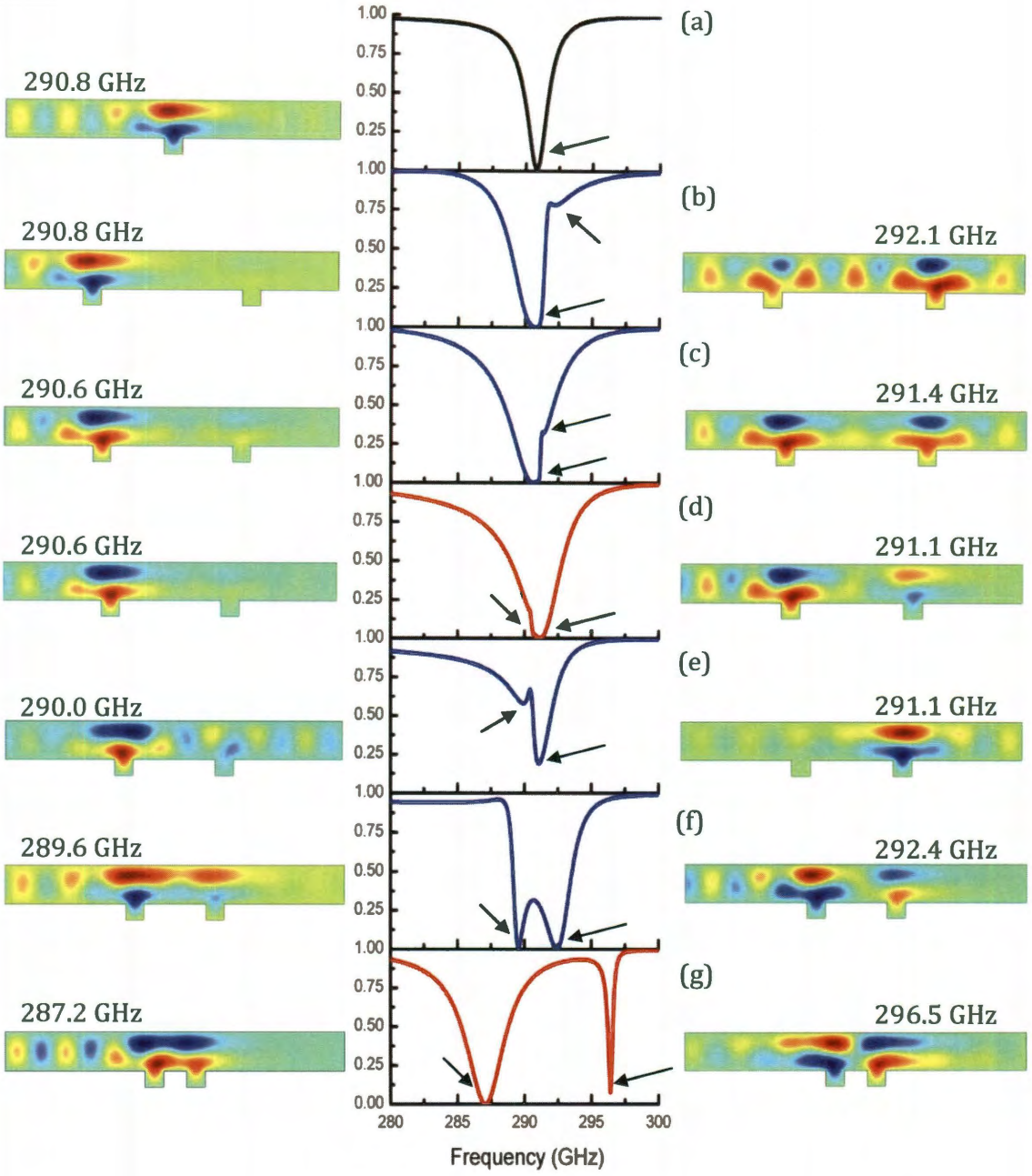

Figure 3-28 Power transmission spectra from FEM simulation for a series of two-groove waveguides with varying separations between the grooves. The electric field patterns at two interesting frequencies are plotted to the left and right of the spectra, with the respective frequencies above each image. These frequencies are indicated with arrows in the spectra. The separation between grooves for each spectrum are: (a) one groove only, (b) 3.58 mm separation, (c) 3.08 mm, (d) 2.58 mm, (e) 2.08 mm, (f) 1.54 mm, and (g) 0.58 mm.

The electric field pattern at both the primary resonance and secondary feature are plotted beside each transmission spectrum. It seems as though the primary resonance arises mostly from a single groove (either the first or second), while the secondary shoulder pattern shows energy confinement in both grooves.

As the separation grows smaller, this primary-resonance-secondary-shoulder pattern evolves into two distinct resonant features (Figure 3-28 (e), (f), (g)). The electric field patterns for these resonances show a conclusive coupling between the grooves, with both grooves involved fairly equally in both resonances.

The geometry in which the grooves are separated by 0.58 mm is of particular interest (Figure 3-28 (g)). The power transmission shows two distinct resonances with significantly different linewidths. The low-frequency resonance has a frequency of 287.1 GHz and a linewidth of 3.5 GHz, giving a quality-factor of 82, while the high-frequency resonance has a frequency of 296.4 GHz and a linewidth of 0.4 GHz, with a quality-factor of 741. This is significantly higher than the Q-factor for the original resonance (Figure 3-28 (a)), 153. This high quality resonance may be of particular interest in sensing applications, since increased Q allows for increased sensitivity.

The electric field patterns of these two resonances are also interesting. At both resonant frequencies, energy is confined almost equally in both grooves. However, the electric field has the same polarity in both grooves for the lower-frequency resonance, while the field has opposite polarity in the two grooves for the higher-frequency resonance. This bears a strong resemblance to the bonding and

anti-bonding modes observed in coupled plasmonic systems [105, 106], leading to comparisons to other coupled plasmonic systems such as whispering gallery mode resonators [107, 108] or photonic molecules [109].

Because of this, we initially hypothesized that the plasmonic coupling between the grooves had led to a resonant splitting effect, in which the original resonance has split into bonding and antibonding modes as shown in the above figure. However, while the "resonant splitting" terminology may be useful, a plasmonic explanation for the splitting is not necessary, due to the fact that mode-matching analysis provides an adequate theoretical explanation for the phenomenon. Below is a comparison of the power transmission predicted by simulation and mode-matching analysis for this geometry, with obviously outstanding agreement (Figure 3-29), indicating that the origin of the resonant splitting is not plasmonic but due to the frequency-dependent reflection within the waveguide structure described by mode-matching.

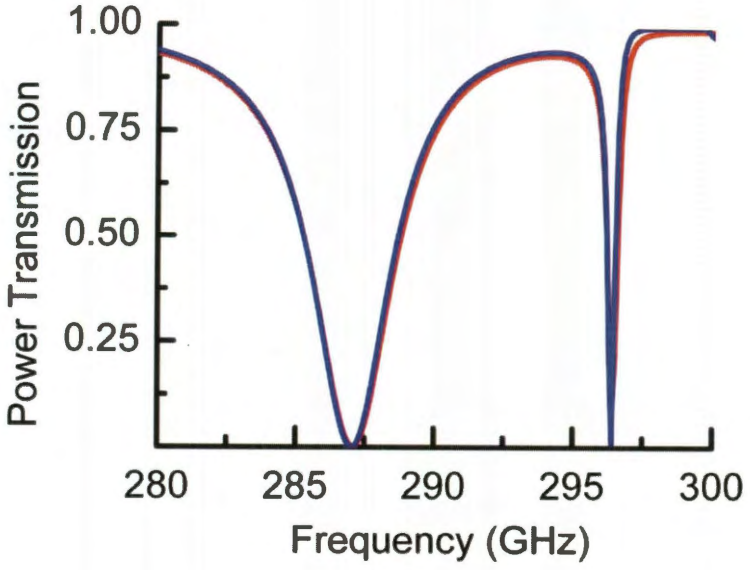

Figure 3-29 Comparison of simulation (red) and mode-matching analysis (blue) power transmission spectra for the "resonant splitting" geometry in which the two grooves are separated by 0.58 mm.

Despite the lack of a plasmonic origin for the resonant splitting, this two-groove-waveguide geometry is still of considerable interest for experimental applications, due to the coupling between the grooves and the potential of a high-Q resonance that (a) has high extinction (in contrast to the very shallow grooves discussed in Section 3.4, which had high Q but low extinction) and (b) is not part of a very complex transmission spectrum (in contrast to the high-Q lines exhibited by the very wide grooves discussed in Section 3.4.)

To confirm this coupling experimentally, we fabricated a waveguide with the geometry based on this two-groove geometry, with two 460 x 412 μm grooves 0.58mm apart (as shown in Figure 3-28 in detail and discussed above). A diagram of the design and a photograph of the fabricated waveguide are shown below.

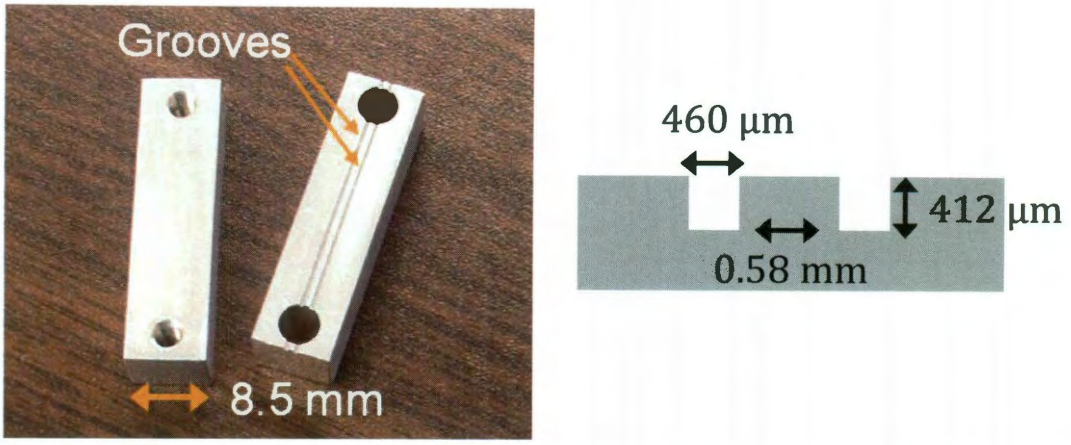

Figure 3-30 Diagram of the waveguide geometry and photograph of the fabricated waveguide.

This waveguide was placed in the time-domain terahertz spectroscopy setup described in Section 3.3. The experimental power transmission spectrum (Figure 3-31) looks very like the simulation and analytical results, showing both the low-frequency "bonding" resonance and the high-frequency "anti-bonding" resonance. The bottom plot provides a closer look at the high-frequency peak, showing its very narrow linewidth of ~1 GHz.

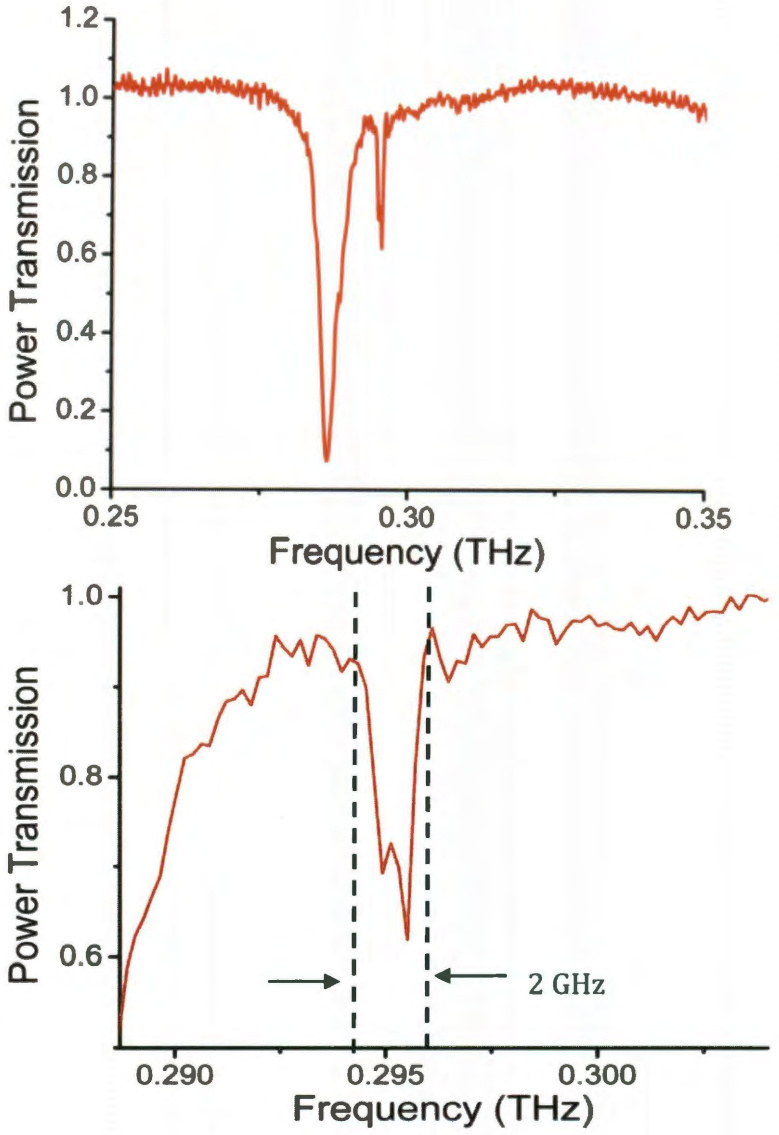

Figure 3-31 Experimental power transmission spectrum. (Top) The frequency range of interest, showing the split resonance. (Bottom right) The higher-frequency resonance, showcasing its narrow linewidth.

A comparison to the mode-matching results over the entire range of TE_1 single-mode propagation from the TE_1 to TE_3 cutoff frequencies (Figure 3-32) shows excellent agreement between experiment and theory, reproducing the two primary resonant features as well as the higher order mode at 401 GHz. Below the figure is a table (Table 3-3) with a quantitative comparison of the frequency, linewidth, and quality factor for the two split resonances. The slight differences between experiment and mode-matching analysis are most likely due to the imperfections in machining that cause the experimental geometry to vary from that used in the analysis.

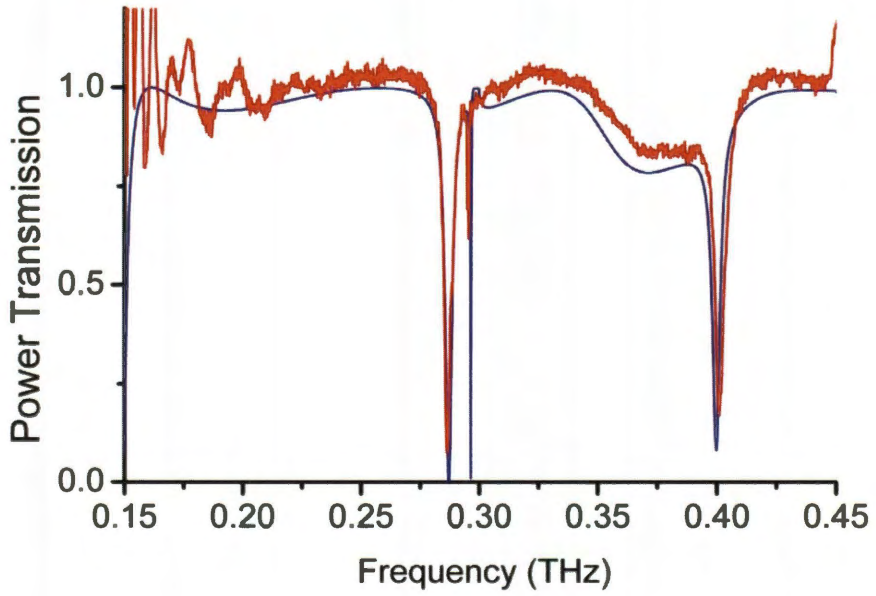

Figure 3-32 Comparison of the experimental (red) and mode-matching analysis (blue) power transmission over the entire range of TE_1 single-mode propagation (150 to 450 GHz) for the two-grooved waveguide.

	Frequency 1	Linewidth 1	Q1	Frequency 2	Linewidth 2	Q2
Experiment	286.3	2.75	104	295.5	1	295
Mode-Matching	287.0	3.41	84	296.4	0.31	956

Table 3-3 Quantitative comparison of resonant frequencies (in GHz), linewidths (in GHz) and quality-factors for the experimental and mode-matching analysis results for the resonant splitting waveguide.

We also performed a spacing test, similar to that performed with the single-groove waveguides (Section 3.3 above), to confirm the dependence of the resonances on plate spacing along with their tunability. Figure 3-33 below shows the shift in the resonant frequencies that occur due to altering the plate spacing. As before, the simulation data is used to calibrate the spacing measurements. The relationship between the plate spacing and the resonant frequency reflects the tunability, or the ability to compensate for errors in fabrication by making changes to the plate spacing to obtain the desired frequency. This relationship is well-fitted by a second-order polynomial for both resonances (blue curves). The tunabilities for the two resonances are roughly equal, approximately 0.25 GHz/μm (250 GHz/mm).

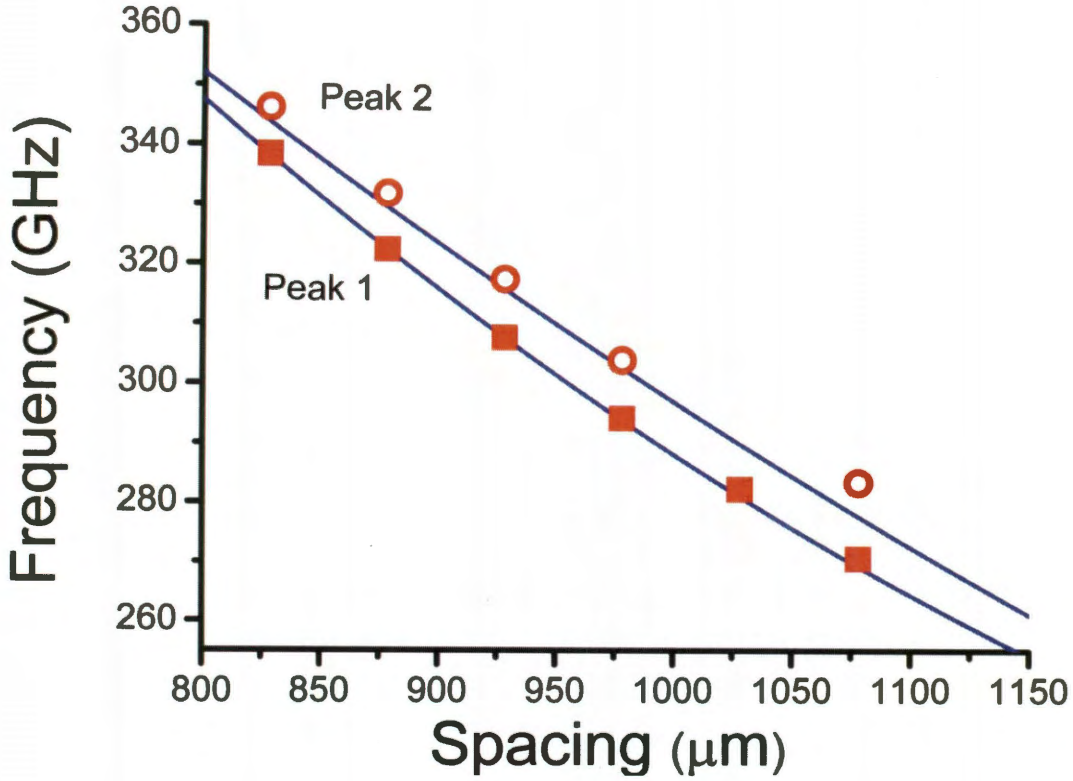

Figure 3-33 Plot of the resonant frequencies of the two peaks as the plate spacing increases. Peak 1 is the lower-frequency resonance, Peak 2 is the higher-frequency resonance. Red squares and circles are the experimental data, while the blue lines represent polynomial fits.

With several different two-groove geometries -- both those with independent channels and those that exhibit resonant splitting -- characterized experimentally and through simulation and mode-matching analysis, the next step is to perform proof-of-concept tests for the capabilities of these designs as microfluidic sensors. This is accomplished by filling the groove with a variety of liquids with different refractive indices, as done for the single-groove waveguide in Ref. [1]. A full

discussion of the liquid filled grooves – experiment, simulation, and theory for single- and multiple-groove waveguides – is given in the next section.

3.7. Liquid Filling

Microfluidic sensing is an area of considerable interest at a wide range of frequencies, with potential applications in security, industry, academia, and medicine driving the search for compact and highly sensitive sensors. These sensors can be optimized to identify unknown materials, to detect the presence of particular materials, or to measure the concentration or contamination of a sample, among other uses. To accomplish these myriad goals, microfluidic sensors employ a similarly wide range of sensing methods: fluorescence, absorbance, chemiluminescence, and refractive index sensing being just a few [110, 111].

Refractive index sensing is of particular interest because of its numerous advantages over other methods. It is noninvasive, simple to implement, and does not require labels or chromophores for detection. Refractive index measurements are a function of concentration rather than mass or volume, giving it an advantage for analyzing small volumes of analytes [112].

The two most common detection methods for refractive index sensing are interferometry and resonant sensors. Interferometric systems are based on the difference in path length along one leg of the interferometer when an analyte is introduced. They provide very high resolutions in terms of the minimum detectable

change in refractive index, but are also complicated to implement and are primarily capable of measuring differences in index rather than an absolute measurement [113, 114]. Resonant sensors, in contrast, measure the change in resonant behavior when an analyte is introduced to a system, either as a change in the extinction ratio or more frequently as a shift in the resonant frequency. Resonant sensors have been implemented with a wide range of geometries, such as optical ring resonators [112], photonic crystals [115, 116], or microsphere resonators [117].

The majority of these designs operate at visible or infrared frequencies. In the terahertz, refractive index sensing is an undeveloped field. Many of the resonators mentioned in Section 3.1 have been implemented to sense thin dielectric layers, but the independent variable is the layer thickness rather than the index [79, 83-86]. Aside from the grooved parallel-plate waveguide, the only other demonstrated terahertz resonator-based refractive index sensor is one proposal based on coupled-resonator photonic crystal waveguides, which is still only implemented in simulation [20]. In contrast, the grooved PPWG design has been confirmed experimentally as a high sensitivity sensor for detecting the refractive index of the material filling the groove [1]. In this section, work is presented expanding the capability of this sensor to multichannel sensing and alternate multi-groove geometries are considered to improve the performance.

The underlying principle of the grooved waveguide as a microfluidic sensor centers on the response of the resonant frequency to the presence of a liquid filling the groove. This was thoroughly established by both experiment and simulation in

Ref. [1] through the investigation of a series of test molecules: simple straight-chain alkanes from octane (C_8H_{18}, referred to as C8 for simplicity) through hexadecane ($C_{16}H_{34}$, referred to as C16), which have well-established refractive indices in the terahertz range [118]. These indices are listed in Table 3-4 below. Only alkanes from octane to hexadecane are used because heavier alkanes are solids at room temperature, while lighter alkanes evaporate too quickly for reliable measurements.

	Formula	**Refractive Index**
C8	C_8H_{18}	1.3919
C9	C_9H_{20}	1.3997
C10	$C_{10}H_{22}$	1.4056
C11	$C_{11}H_{24}$	1.4108
C12	$C_{12}H_{26}$	1.4154
C13	$C_{13}H_{28}$	1.4196
C14	$C_{14}H_{30}$	1.4224
C15	$C_{15}H_{32}$	1.4256
C16	$C_{16}H_{34}$	1.4285

Table 3-4 List of refractive indices of the straight-chain alkanes at terahertz frequencies.

When the groove is filled by a dielectric liquid such as a straight-chain alkane, the resonant frequency shifts by an amount proportional to the refractive index of

the liquid. Figure 3-34 below is an example, showing the shift in the resonant frequency for the range of straight-chain alkanes.

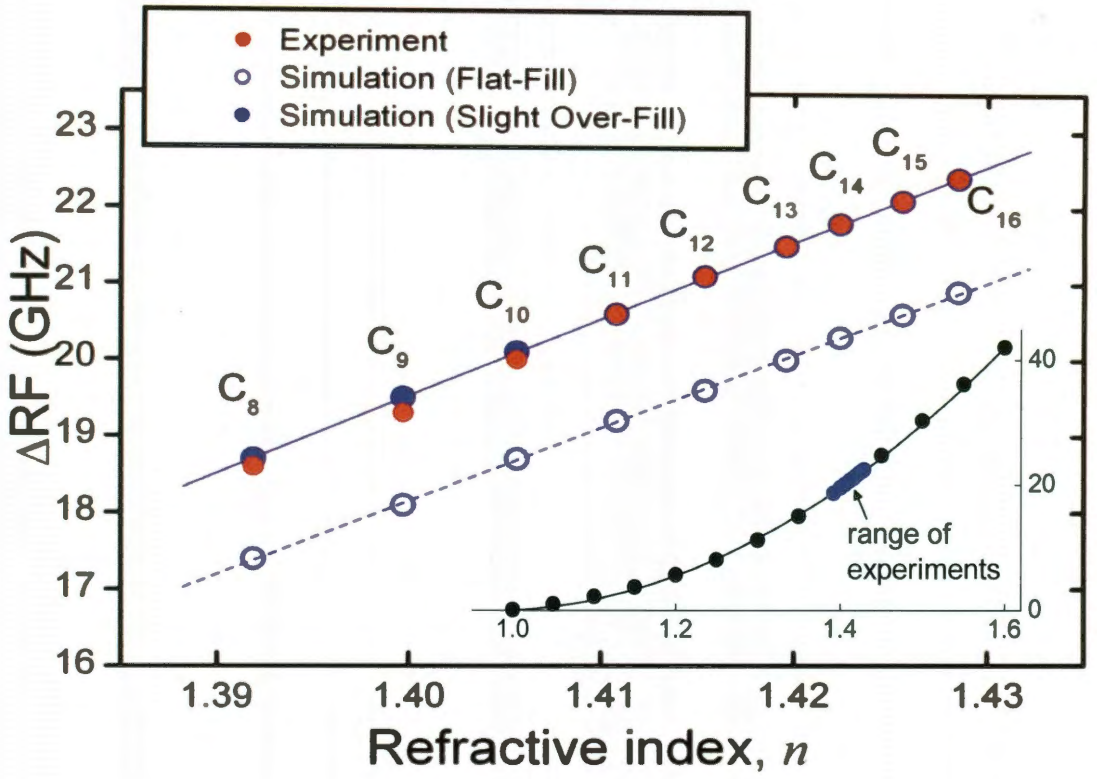

Figure 3-34 Plot of the shift in the resonant frequency versus refractive index for a range of straight-chain alkanes. Solid red circles are experimental data, while the blue circles are the results from simulation. Open circles represent the case of an exact fill, while the solid circles represent the case of a slight over-fill of 9 μm. The blue lines are linear fits of the data. Inset: The shift in resonant frequency versus refractive index over a wide range of indices. From Ref. [1].

Simulation results indicate that this linear relationship is true only for small ranges of refractive indices; the overall trend is of a quadratic dependence of resonant frequency on refractive index (inset to Figure 3-34). In additional, simulation results also demonstrated the importance of the accuracy of the filling

mechanism. The experimental measurements (red circles) were inconsistent with simulation results that assumed a perfect fill, in which the liquid comes to the top of the groove with no overfilling (blue open circles). An overfill of 9 μm is required to agree with experimental data (blue solid circles), indicating that any sensing applications must be able to control the fill volume with high precision.

A more thorough understanding of the effects of a dielectric filling in the groove on the resonant frequency can be obtained by extending the mode-matching analysis described above in Section 3.5.

3.7.1. Mode Matching for a Dielectric-filled Groove

The mode-matching technique has essentially the same form when applied to a waveguide with a dielectric-filled groove as to a waveguide with an empty groove (or even an ungrooved waveguide): it calculates the reflection and transmission into various modes of the waveguide sections, based on the impedances and the overlap of the mode patterns. To incorporate a dielectric filling into the waveguide, those impedances and mode patterns must be recalculated to reflect the influence the fill has on the electric field inside the waveguide.

The mode patterns and impedances in the ungrooved sections are unchanged from the original TE_1 equations (Equations [3-19] and [3-21] in Section 3.5 above). The grooved waveguide section can be treated as essentially a TE_1 waveguide partially filled with a dielectric, and its mode patterns can be derived from those of a

partially-filled rectangular waveguide whose transverse dimension is extended to infinity. This approach has been used previously to study TEM mode parallel-plate waveguides that are completely filled with a silicon slab [119].

The analytic solution of a partially-filled PPWG requires the use of hybrid TE modes, as pure TE modes no longer satisfy the boundary conditions due to the influence of the dielectric. Hybrid TE modes are field configurations that combine TE and TM modes in order to satisfy these boundary conditions. The mathematics of hybrid TE modes, particularly for partially-filled rectangular waveguides, are discussed in detail in Ref. [91].

A diagram of the cross-section of the grooved waveguide is shown below. For this analysis, the relevant parameters are the plate spacing *b* and the height of the liquid fill *h* relative to the bottom plate. The zero of the y-axis is set to be the top plate of the waveguide to match the previous mode-matching formalism [6].

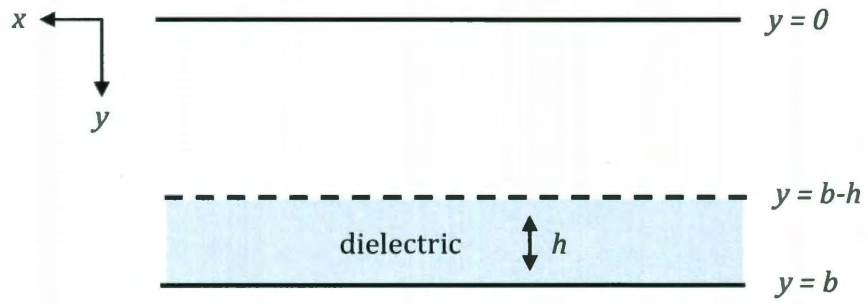

Figure 3-35 Diagram of the cross-section of a grooved waveguide with a dielectric fill.

[6] The equations in Ref. 91 (Balanis, *Advanced Engineering Electromagnetics)* are constructed with $y = 0$ at the bottom of the dielectric fill. The coordinates must be transformed to compare the equations directly to those in this thesis.

The hybrid mode solutions for this waveguide are derived from the fundamental expressions for electric and magnetic field components for TE modes:

$$E_x = \frac{1}{\varepsilon}\frac{\partial F_y}{\partial z} \qquad H_x = -j\frac{1}{\omega\mu\varepsilon}\frac{\partial^2 F_y}{\partial x \partial y}$$

$$E_y = 0 \qquad H_y = -j\frac{1}{\omega\mu\varepsilon}\left(\frac{\partial^2}{\partial y^2} + \beta^2\right)F_y \qquad \textbf{[3-42]}$$

$$E_z = -\frac{1}{\varepsilon}\frac{\partial F_y}{\partial x} \qquad H_z = -j\frac{1}{\omega\mu\varepsilon}\frac{\partial^2 F_y}{\partial y \partial z}$$

In these equations, F_y is the y component of the vector potential and satisfies the scalar wave equation. The general form of F_y is given below:

$$F_y = [C_1 \cos\beta_x x + D_1 \sin\beta_x x] \qquad \textbf{[3-43]}$$

$$\times \left[C_2 \cos\beta_y y + D_2 \sin\beta_y y\right] A e^{-j\beta_z z}$$

For partially-filled dielectric waveguide, the fields for the dielectric-filled portion and the free space portion have different vector potentials, so two different expressions for F_y are required ($F_y{}^d$ and $F_y{}^0$ respectively).

$$F_y^d = \left[C_1^d \cos\beta_{xd}x + D_1^d \sin\beta_{xd}x\right] \times \left[C_2^d \cos\beta_{yd}(b-y) + D_2^d \sin\beta_{yd}(b-y)\right]A^d e^{-j\beta_z z} \quad \textbf{[3-44]}$$

$$F_y^0 = \left[C_1^0 \cos\beta_{x0}x + D_1^0 \sin\beta_{x0}x\right] \times \left[C_2^0 \cos\beta_{y0}y + D_2^0 \sin\beta_{y0}y\right]A^0 e^{-j\beta_z z} \quad \textbf{[3-45]}$$

The various phase constants above are related by the following equations:

$$\beta_d{}^2 = \omega^2\mu_d\varepsilon_d = \beta_{xd}{}^2 + \beta_{yd}{}^2 + \beta_z{}^2 \quad \textbf{[3-46]}$$

$$\beta_0{}^2 = \omega^2\mu_0\varepsilon_0 = \beta_{x0}{}^2 + \beta_{y0}{}^2 + \beta_z{}^2 \quad \textbf{[3-47]}$$

In particular, the phase constants in the z-direction (β_z) are the same for both portions, necessary so that two parts of the electric field propagate together.

To obtain the hybrid mode solutions, we apply a set of boundary conditions to these equations. Initially we use the boundary conditions specified in Ref. [91] for the dielectric-filled rectangular waveguide of height b and width a, which we will later adapt to the dielectric-filled parallel-plate waveguide by setting a equal to infinity.

The boundary conditions for the longitudinal electric and magnetic field components are:

$$E_z^d(x = 0) = E_z^d(x = a) = 0 \quad \textbf{[3-48]}$$

$$E_z^0(x = 0) = E_z^0(x = a) = 0 \quad \textbf{[3-49]}$$

$$E_z^d(y = b) = 0 \quad \textbf{[3-50]}$$

$$E_z^0(y = 0) = 0 \quad \textbf{[3-51]}$$

$$E_z^d(y = b - h) = E_z^0(y = b - h) \quad \textbf{[3-52]}$$

$$H_z^d(y = b - h) = H_z^0(y = b - h) \quad \textbf{[3-53]}$$

The boundary conditions for the transverse electric and magnetic field components are given below:

$$E_y^d(x = 0) = E_y^d(x = a) = 0 \quad \textbf{[3-54]}$$

$$E_y^0(x = 0) = E_y^0(x = a) = 0 \quad \textbf{[3-55]}$$

$$E_x^d(y = b) = 0 \quad \textbf{[3-56]}$$

$$E_x^0(y = 0) = 0 \quad \textbf{[3-57]}$$

$$E_x^d(y = b - h) = E_x^0(y = b - h) \quad \text{[3-58]}$$

$$H_x^d(y = b - h) = H_x^0(y = b - h) \quad \text{[3-59]}$$

These conditions ensure that the electric fields are normal to the metal sides of the waveguide and that the relevant electric and magnetic field components are continuous at the surface of the dielectric.

Using these boundary conditions we can refine the expressions for F_y and obtain the solutions for the electric and magnetic field components. We start with the boundary conditions for longitudinal components, specifically Equation [3-49].

$$E_z^0(x = 0) = 0$$

$$E_z^0 = -\frac{1}{\varepsilon_0}\frac{\partial F_y^0}{\partial x}$$

$$E_z^0 = -\frac{1}{\varepsilon_0}\beta_{x0}[-C_1^0 \sin\beta_{x0}x + D_1^0 \cos\beta_{x0}x]$$

$$\times \left[C_2^0 \cos\beta_{y0}y + D_2^0 \sin\beta_{y0}y\right]A^0 e^{-j\beta_z z}$$

$$E_z^0(x=0)$$

$$= -\frac{1}{\varepsilon_0}\beta_{x0}[-C_1^0 \sin 0 + D_1^0 \cos 0]$$

$$\times \left[C_2^0 \cos \beta_{y0} y + D_2^0 \sin \beta_{y0} y\right] A^0 e^{-j\beta_z z}$$

$$= 0$$

$$\longrightarrow D_1^0 = 0$$

Similarly,

$$E_z^0(x=a) = 0$$

$$E_z^0(x=a)$$

$$= -\frac{1}{\varepsilon_0}\beta_{x0}[-C_1^0 \sin \beta_{x0} a]$$

$$\times \left[C_2^0 \cos \beta_{y0} y + D_2^0 \sin \beta_{y0} y\right] A^0 e^{-j\beta_z z} = 0$$

$$\longrightarrow \beta_{x0} = \frac{m\pi}{a}$$

The same procedure with Equation [3-48] yields identical expressions for β_{xd} and D_1^d.

Boundary condition [3-50] can be handled similarly.

$$E_z^d(y = b) = 0$$

$$E_z^d = -\frac{1}{\varepsilon_d}\frac{\partial F_y^d}{\partial x}$$

$$E_z^d = -\frac{1}{\varepsilon_d}\beta_{xd}\left[-C_1^d \sin \beta_{xd} x\right]$$

$$\times \left[C_2^d \cos \beta_{yd}(b - y) + D_2^d \sin \beta_{yd}(b - y)\right]$$

$$\times A^d e^{-j\beta_z z}$$

$$E_z^d(y = b) = -\frac{1}{\varepsilon_d}\beta_{xd}\left[-C_1^d \sin \beta_{xd} x\right]$$

$$\times \left[C_2^d \cos 0 + D_2^d \sin 0\right]A^d e^{-j\beta_z z} = 0$$

$$\longrightarrow C_2^d = 0$$

The boundary condition [3-51] yields the same result. We choose this step to extend the rectangular waveguide to the parallel-plate waveguide by setting a equal to infinity. This in turn reduces β_x to zero and simplifies the potential F_y. We also simplify by combining the constants into one amplitude term.

$$F_y^d = A^d \sin \beta_{yd}(b-y)e^{-j\beta_z z} \quad \textbf{[3-60]}$$

$$F_y^0 = A^0 \sin \beta_{y0} y e^{-j\beta_z z} \quad \textbf{[3-61]}$$

At this point, we move from the longitudinal fields to the transverse fields, evaluating the boundary conditions for E_x, E_y, H_x, etc. Many of these conditions (Equations [3-54] to [3-57]) are already fulfilled by the equations in their current form. Equation [3-58] leads to a relationship between the amplitudes of the fields in the dielectric and free-space regions of the waveguide.

$$E_x^d(y = b-h) = E_x^0(y = b-h)$$

$$\frac{1}{\varepsilon_d}\frac{\partial F_y^d}{\partial z}\bigg|_{y=b-h} = \frac{1}{\varepsilon_0}\frac{\partial F_y^0}{\partial z}\bigg|_{y=b-h}$$

$$\frac{-j\beta_z A^d}{\varepsilon_d}\sin \beta_{yd}(h) = \frac{-j\beta_z A^0}{\varepsilon_0}\sin \beta_{y0}(b-h)$$

$$\longrightarrow A^0 = \frac{\varepsilon_0}{\varepsilon_d}\frac{\sin \beta_{yd} h}{\sin \beta_{y0}(b-h)} A^d \quad \textbf{[3-62]}$$

The last boundary condition left to consider is Equation [3-53].

$$H_z^d(y = b-h) = H_z^0(y = b-h)$$

$$-j\frac{1}{\omega\mu_d\varepsilon_d}\frac{\partial^2 F_y^d}{\partial y\partial z}\bigg|_{y=b-h} = -j\frac{1}{\omega\mu_0\varepsilon_0}\frac{\partial^2 F_y^0}{\partial y\partial z}\bigg|_{y=b-h}$$

$$\frac{1}{\mu_d\varepsilon_d}\beta_{yd}A^d\cos\beta_{yd}h = \frac{-1}{\mu_0\varepsilon_0}\beta_{y0}A^0\cos\beta_{y0}(b-h) \quad \textbf{[3-63]}$$

We can remove the amplitude terms by dividing Equation [3-63] by Equation [3-62].

$$\frac{\beta_{yd}}{\mu_d}\cot\beta_{yd}h = \frac{-\beta_{y0}}{\mu_0}\cot\beta_{y0}(b-h) \quad \textbf{[3-64]}$$

By substituting the phase constant identities (Equations [3-46] and [3-47]) we can obtain a single transcendental equation that is only a function of β_z.

$$\frac{\sqrt{\omega^2\mu_d\varepsilon_d - {\beta_z}^2}}{\mu_d}\cot\left(h\sqrt{\omega^2\mu_d\varepsilon_d - {\beta_z}^2}\right) \quad \textbf{[3-65]}$$

$$= \frac{-\sqrt{\omega^2\mu_0\varepsilon_0 - {\beta_z}^2}}{\mu_0}\cot\left(\sqrt{\omega^2\mu_0\varepsilon_0 - {\beta_z}^2}(b-h)\right)$$

To obtain the phase constants for the modes of this waveguide, we solve this transcendental equation numerically. Both real and imaginary solutions should be found to account for both propagating and attenuating modes. This process is nontrivial and is demonstrated in the annotated MATLAB code in Appendix A.

Once we have determined the phase constants, we have complete equations for the electric field pattern within the partially dielectric-filled parallel-plate waveguide.

$$E_x^d = \frac{-j\beta_z A^d}{\varepsilon_d} \sin \beta_{yd}(b-y) e^{-j\beta_z z} \quad \textbf{[3-66]}$$

$$E_x^0 = \frac{-j\beta_z A^0}{\varepsilon_0} \sin(\beta_{y0} y) e^{-j\beta_z z} \quad \textbf{[3-67]}$$

To obtain the normalized modal field patterns Φ^d and Φ^0, we replace the constant expression $-j\beta_z A^d / \varepsilon_d$ with a normalization factor N, where N is obtained by integrating the electric field intensity over the entire height of the waveguide.

$$N = \frac{1}{\sqrt{\frac{h}{2} - \frac{\sin 2\beta_{yd} h}{4\beta_{yd}} + \left(\frac{\sin \beta_{yd} h}{\sin \beta_{y0}(b-h)}\right)^2 \left(\frac{b-h}{2} - \frac{\sin \beta_{y0}(b-h)}{4\beta_{y0}}\right)}} \quad \textbf{[3-68]}$$

Thus the normalized modal field patterns Φ^d and Φ^0 can be expressed as:

$$\Phi^d = N \sin \beta_{yd}(b - y) \quad \text{[3-69]}$$

$$\Phi^0 = N \left(\frac{\sin \beta_{yd} h}{\sin \beta_{y0}(b - h)} \right) \sin \beta_{y0} y \quad \text{[3-70]}$$

For mode-matching analysis, in addition to these modal field patterns we also require expressions for the impedance. For a parallel-plate waveguide, the impedance can be expressed as a ratio of the transverse electric and magnetic fields:

$$\mathrm{Z} = \frac{E_x}{H_y} \quad \text{[3-71]}$$

We can evaluate this using the expressions derived above.

$$E_x^d = \frac{1}{\varepsilon_d} \frac{\partial F_y}{\partial z} = \frac{-j\beta_z A^d}{\varepsilon_d} \sin\left(\beta_{yd}(b - y)\right) e^{-j\beta_z z} \quad \text{[3-72]}$$

$$H_y^d = \frac{-j}{\omega \mu_d \varepsilon_d} \left(\frac{\partial^2}{\partial y^2} + \beta^2 \right) F_y$$

$$= \frac{-jA^d}{\omega \mu_d \varepsilon_d} (\beta^2 - {\beta_{yd}}^2) \sin\left(\beta_{yd}(b - y)\right) e^{-j\beta_z z} \quad \text{[3-73]}$$

$$\longrightarrow Z_d = \frac{\omega \mu_d}{\beta_z} \quad \text{[3-74]}$$

The expression for impedance reduces to the same as that for the empty waveguide (Equation [3-21]). The same result is obtained for the impedance of the free-space portion of the dielectric-filled waveguide.

Now that we have expressions for both the modal field pattern and the impedance, we can use the β_z solutions to Equation [3-65] to evaluate these expressions for various modes of the waveguide. Figure 3-36 below shows the resulting mode patterns for an example grooved waveguide with a dielectric liquid filling the groove.

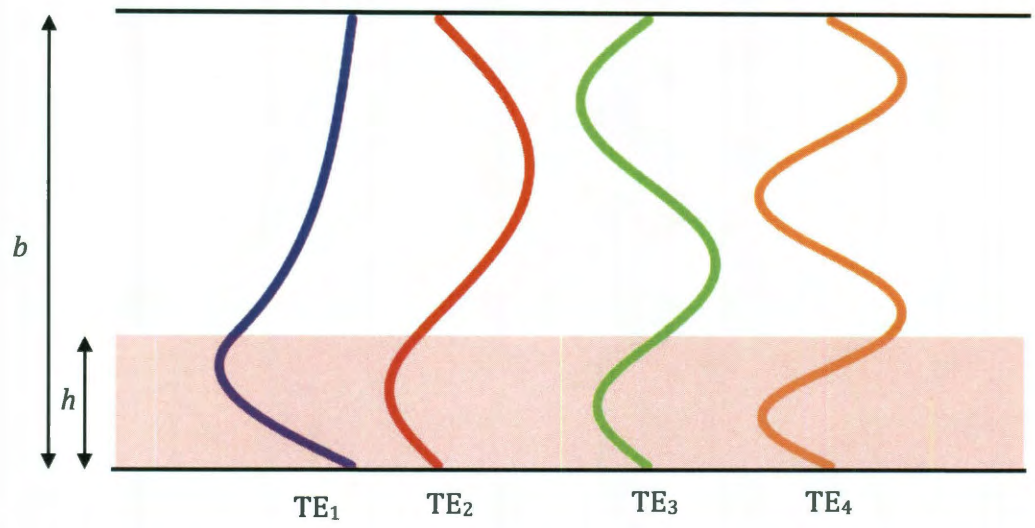

Figure 3-36 Electric field patterns for the TE_1 to TE_4 modes of the partially dielectric-filled parallel-plate waveguide. The dielectric in this case is C14, for a waveguide of spacing 1.409 mm and has a 412 μm high fill. The mode patterns are obtained at 270 GHz but have only a small freqeuency dependence.

These mode patterns clearly show that the general shapes of the modes are similar to the TE modes of the empty waveguide (Figure [3-2] in Section 3.2), but there is a concentration of the propagating energy in the dielectric portion, as one

might expect. The patterns above are calculated at 270 GHz; unlike the TE modes of the empty waveguide there is a frequency dependence in the modal patterns, but the effect is small and is due to the frequency dependence of the phase constant β_z.

The mode patterns above and the impedances in Equation [3-74] can then be used to perform mode-matching analysis as described in Section 3.5. The only difference occurs when calculating the mode overlap matrix *M* (Equation [3-23]). Both the dielectric and free-space portions of the waveguide must be considered in the integral:

$$M(m,n) = \int_0^{b-h} \Phi_{1n}\Phi_{2m}^0\, dy + \int_{b-h}^{a} \Phi_{1n}\Phi_{2m}^d\, dy \qquad [3\text{-}75]$$

where Φ_{1n} is modal field pattern for the *n*th mode of the ordinary TE waveguide and Φ_{2m} is the pattern for the *m*th mode of the partially liquid-filled waveguide described here. Since the field patterns for the liquid-filled waveguide are also defined in terms of sine functions, there is still an analytical evaluation of *M*.

In Equation [3-75] above, there is assumed to be a slight overfill, i.e. $b\text{-}h < a$. In this case the integral must be completed in two parts, one calculating the overlap between the empty waveguide and the free-space portion of the dielectric-filled waveguide ($y=0$ to $y=b\text{-}h$) and another calculating the overlap between the empty waveguide and the dielectric portion ($y=b\text{-}h$ to $y=a$). If the groove is instead underfilled ($b\text{-}h > a$), only the first integration is necessary.

We can use this mode-matching analysis to consider the performance of the grooved parallel-plate waveguide as a microfluidic sensor and to explore the potential of a two-grooved sensor.

For example, a waveguide with a groove of 457 by 406 μm filled with materials with a wide range of refractive indices can be analyzed with mode-matching analysis (Figure 3-37), yielding a quadratic dependence of the resonant shift on the index, as predicted by simulation in Figure 3-34.

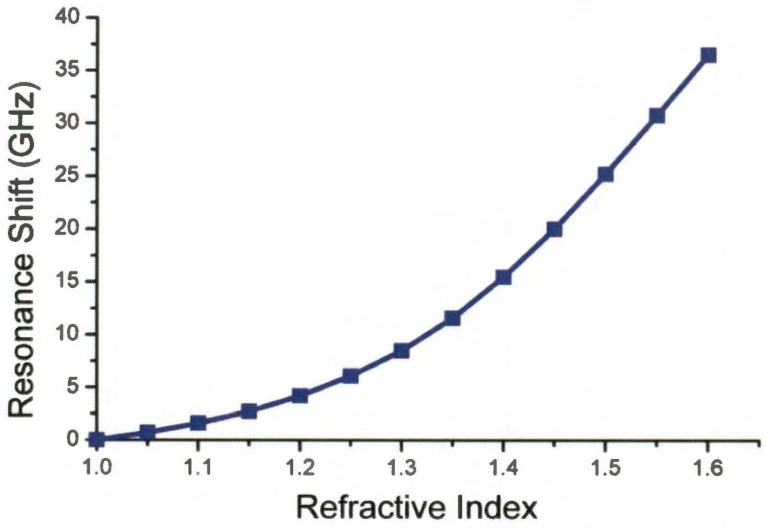

Figure 3-37 Plot of the shift in the resonant frequency for a groove of dimensions 457 by 406 μm when filled exactly to the top by dielectrics of varying refractive index.

These resonance shifts were calculated with the groove perfectly filled by the dielectric – 406 μm of liquid in a 406 μm deep groove. We can also use mode-matching analysis to investigate the dependence of the resonant shift on the filling level in the groove (*h* in Figure 3-35). By starting with an empty groove and calculating the resonant frequency for the groove containing C14 (index $n = 1.4224$)

at a series of fill heights from 0 μm to 406 μm, and continuing to overfill to 600 μm, we can create a curve that we can later use to calibrate the relationship between the fill height and the volume in the groove, which is more easily controlled experimentally (Figure 3-38).

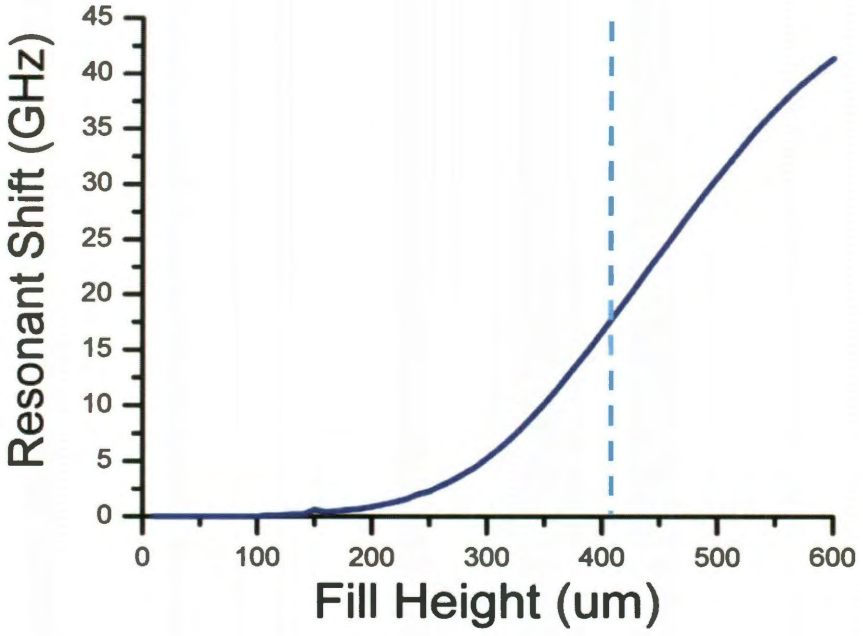

Figure 3-38 Plot of the shift in resonant frequency versus the height of the C14 filling the groove. A light blue dashed line marks the height of a perfect fill, 406 μm.

This curve indicates that there is a minimum fill height necessary to produce a measurable shift in the resonant frequency. It also indicates a roughly linear dependence on fill height once this minimum level has been reached. This linear dependence continues far beyond the point of perfect filling, which is experimentally unrealistic – the groove would begin to overflow at some point and the response would saturate. As it stands, this curve will be quite useful for

calibration. Experimental fills are measured in volume, rather than fill height, and by filling the groove with a particular volume and matching its response to a point on the curve in Figure 3-38 above, the relationship between fill height and volume can be determined and the sensor calibrated for future experiments.

Another curve that will be useful for matching to experiment is the dependence of the resonant shift on the plate spacing. Previous figures have demonstrated the dependence of the resonant frequency of the empty waveguide on the plate spacing (Figure 3-10 in Section 3.3, Figure 3-21 in Section 3.5.3, and Figure 3-33 in Section 3.6.2). It follows that the resonant frequency when the groove is filled would also depend on the spacing. However, mode-matching analysis allows us to determine whether the *shift*, the difference in those two frequencies, also depends on the plate spacing. The result is plotted in Figure 3-39 below over the range of plate spacings for which mode-matching has been shown to be accurate.

This figure demonstrates the importance of accurate determination of the plate spacing, because it will have a tremendous effect on the resonant shift observed for a particular refractive index.

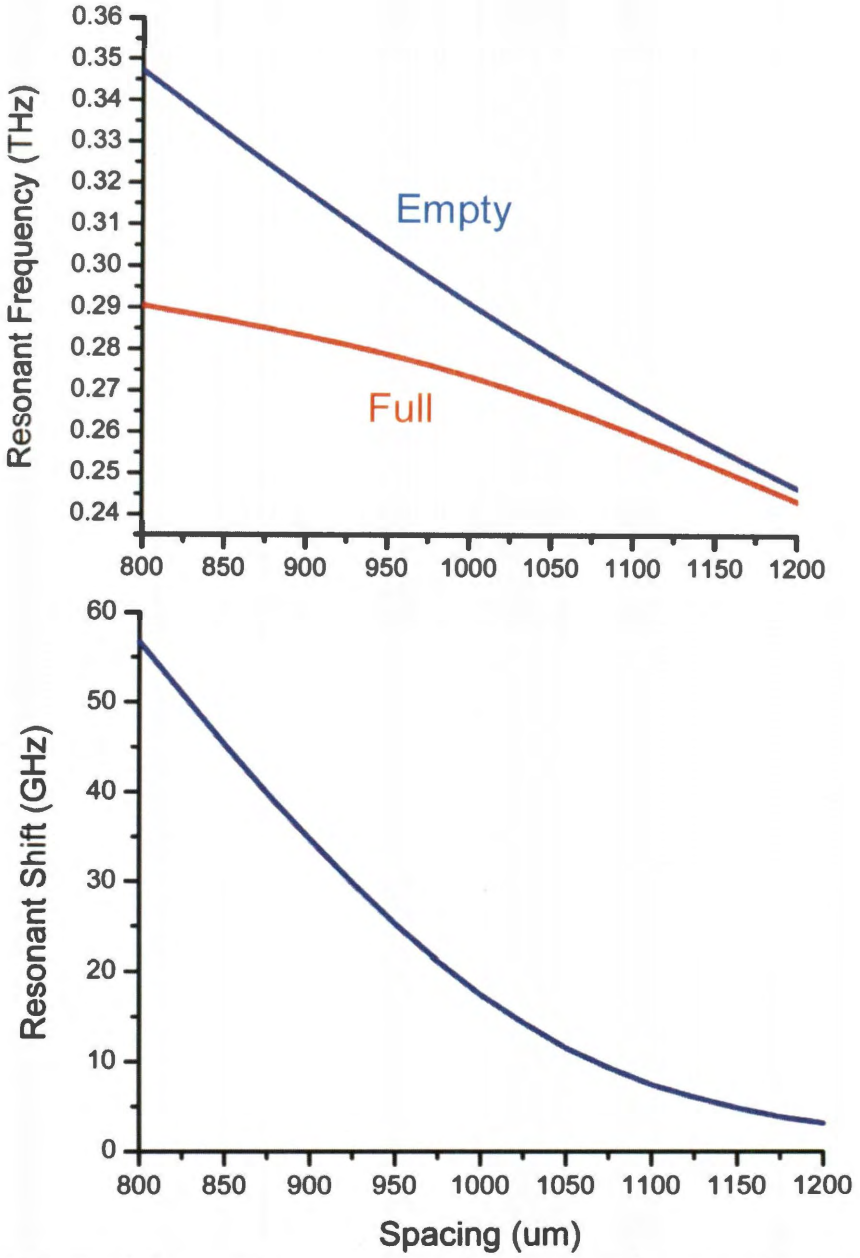

Figure 3-39 (Top) Resonant frequency vs. plate spacing for an empty groove (blue) and a groove filled with C14 (red). The difference between these two is the resonant shift. (Bottom) Resonant shift vs. plate spacing.

These results illustrate the value of mode-matching analysis for characterizing of the grooved parallel-plate waveguide microfluidic sensor. It can also be used to characterize PPWG sensors with two grooves, either in independent multichannel operation or with operation based on the resonant splitting of two similar grooves.

3.7.2. Multichannel Liquid Filling

The multichannel sensor design – two grooves, one of dimensions 711 by 406 μm and the other 457 by 406 μm -- was presented earlier in Section 3.6.1 and the lack of coupling between the two grooves was established through simulation and experiment. To prove multichannel operation, we must demonstrate that this independence extends to the resonant shifts observed when the grooves are filled.

Initially, we demonstrate the possibility using mode-matching analysis. By filling one groove with a range of materials (such as straight-chain alkanes) and filling the other groove with a constant material (C14), we can show that each resonance only depends on the material in the respective groove with no crosstalk between them. These results are shown below in Figure 3-40, with the resonant shift plotted against the varying refractive index.

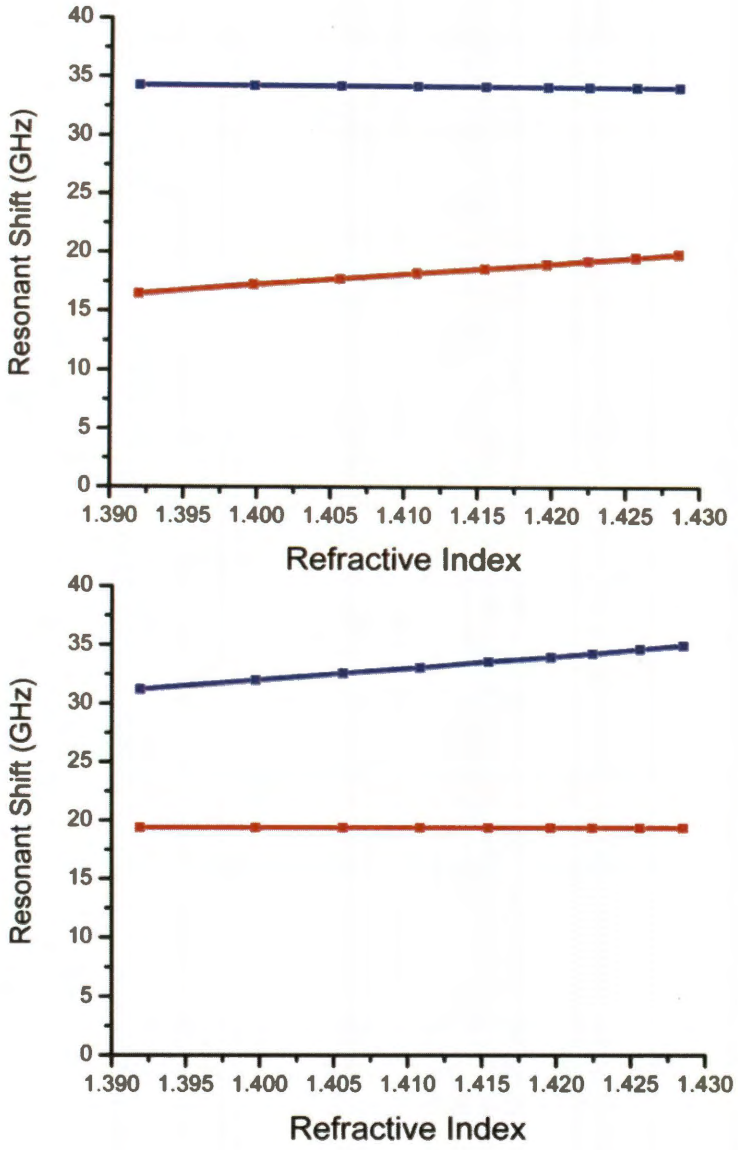

Figure 3-40 (Top) Mode-matching analysis of the multichannel waveguide in which Groove 1 (711 by 406 μm) is filled with C14 and Groove 2 (457 by 406 μm) is filled with a range of alkanes. The resonant shifts of both grooves relative to the empty waveguide are plotted vs. the varying index in Groove 2. (Bottom) Similar, but with the varying index in Groove 1.

These results clearly show that each groove is independent, as the filling material in one groove has no effect on the resonance arising from the other.

With mode-matching analysis supporting the independent sensing operation of two grooves in the multichannel waveguide design, we conducted experimental tests to confirm this by independently measuring the shift of each resonant frequency caused by filling the grooves with a series of straight-chain alkanes.

These experimental tests were performed with the time-domain THz spectroscopy setup described in previous Section 3.3. The waveguide was fabricated with the geometry described in Section 3.6.1 and illustrated in Figure 3-23 (actual fabrication geometry of Groove 1 is 711 by 406 μm and Groove 2 is 457 by 406 μm). However, a special design is required to accommodate the liquid filling. In previous experiments, the waveguides were essentially a two-dimensional design, extended out to several centimeters in the transverse direction in order to exceed the width of the input beam. The grooves in these waveguides are open channels, which cannot be filled with liquid without leakage from the ends. There is also no convenient way to introduce the liquid into the grooves due to them being covered by the top plate of the waveguide.

To correct these problems, a waveguide design such as the one shown below is employed:

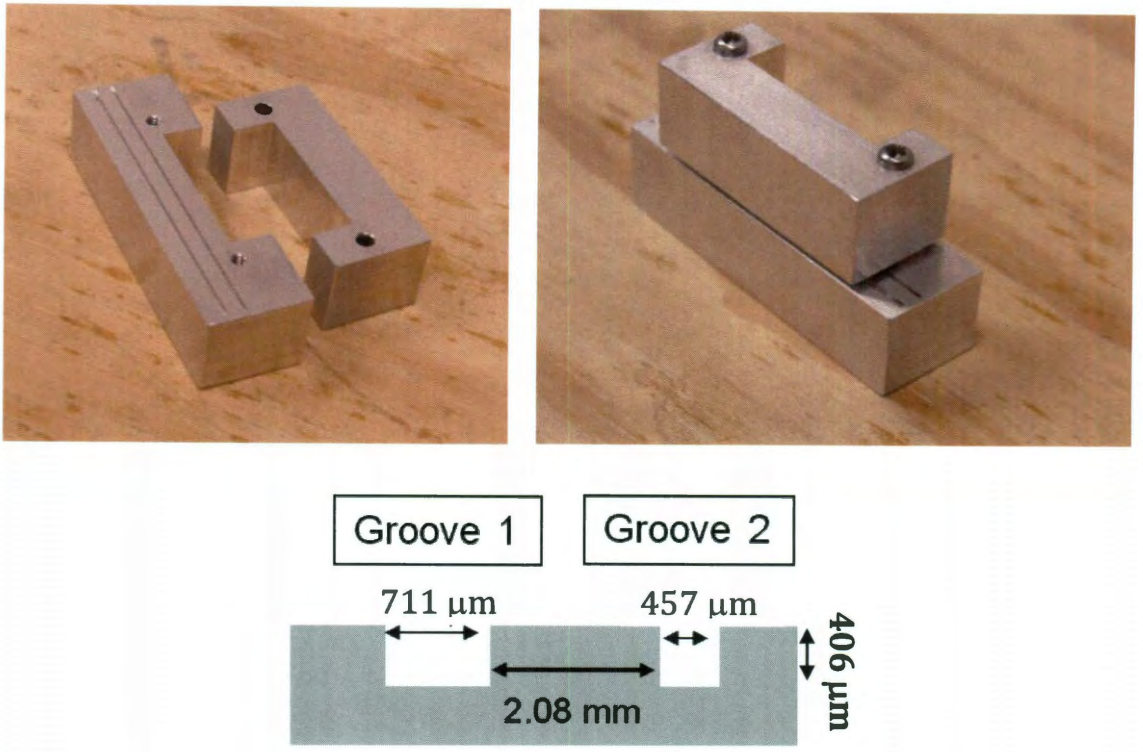

Figure 3-41 Photographs and diagram of the multichannel waveguide geometry. Note the grooves that do not extend across the entire waveguide, and the bottom plate that exceeds the width of the top plate for ease of access to the grooves.

The grooves are of constant depth across the width of the propagation region of the waveguide, but they grow shallower and disappear at the edges of the waveguide beyond the region of propagation. This alteration turns the grooves into effective fluid channels. Also, the bottom plate of the waveguide extends a significant distance beyond the top plate, allowing easy access to the channel for filling.

The filling is accomplished through the use of high-precision microliter syringes. While previous experiments involved a complicated laser leveling system to ensure a consistent fill volume [1], in this experiment we relied upon high-precision syringes to give a consistent, repeatable fill volume to within 0.05 μL, very small compared to the total volume of the grooves (~10 μL each). In order to find a maximum fill level, the grooves were gradually filled with C14 by increments of 0.25 μL for Groove 1 and 0.1 μL for Groove 2 (Figure 3-42). As the volume of liquid in the groove increased, there was initially no change in the resonant behavior until a certain minimum filling level was obtained (approximately 6 μL for Groove 1 and 3 μL for Groove 2), at which point the resonance begins shifting to lower frequencies. The degree of this resonant shift increases in a roughly linear fashion until the groove begins to overflow and the response saturates. In order to ensure reproducibility and avoid over-filling, we choose a consistent volume just below the point of overflow/saturation of 11.5 μL for Groove 1 and 8.5 μL for Groove 2 for all further data sets.

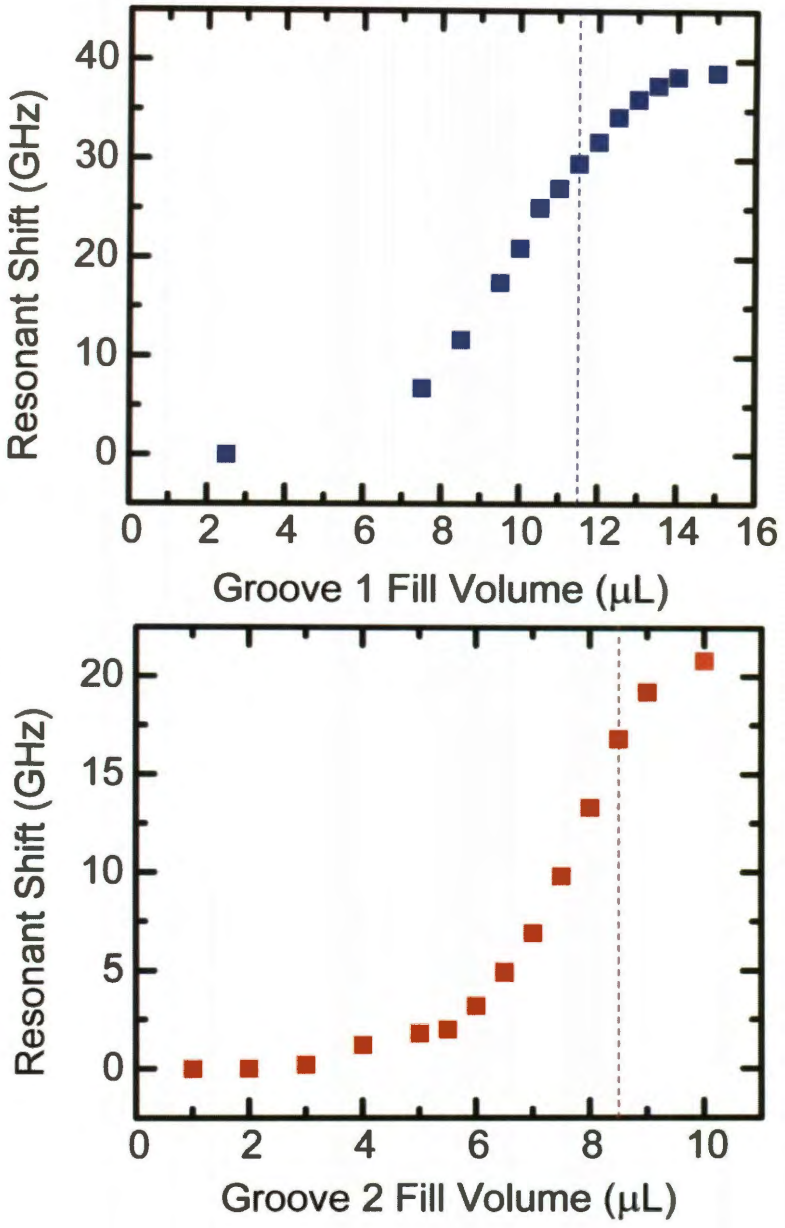

Figure 3-42 Plots of the shift in the resonant frequency for Groove 1 (top) and Groove 2 (bottom) as they are filled with C14. The dashed lines mark the optimum fill levels for the maximum resonant shift without overflow.

To avoid cross-contamination of fluids, a designated syringe was used for each liquid, and then cleaned after use. Between each data set the waveguide was disassembled and cleaned using hexane (C_6H_{14}) to remove any residue. Because this cleaning technique requires the waveguide to be disassembled, we must compensate for small variations in the plate spacing that occur when the waveguide is reassembled and reinserted into the setup. To do this, a scan is taken with the waveguide empty before each liquid fill trial. Then the syringe is inserted into the grooves and the liquid is injected. The resonance shift caused by the liquid is calculated from the difference in frequency for a particular resonant feature in the filled vs. unfilled groove data sets.

Once the ideal filling volumes have been determined, the next step is to test the independence of the two channels and refractive-index dependence of the shifts in resonant frequency due to liquid filling. Data sets were obtained for several combinations of two fluids in the two grooves, using various alkanes. To begin with, we select two alkanes as test materials: C10 and C14. These are heavy enough that evaporation is not a concern, and their resonance shifts are different enough to be easily distinguishable.

When both grooves are filled with C14, both resonances change by a considerable amount relative to the empty waveguide (Figure 3-43). The resonant shifts are marked with arrows to illustrate clearly how this is measured experimentally.

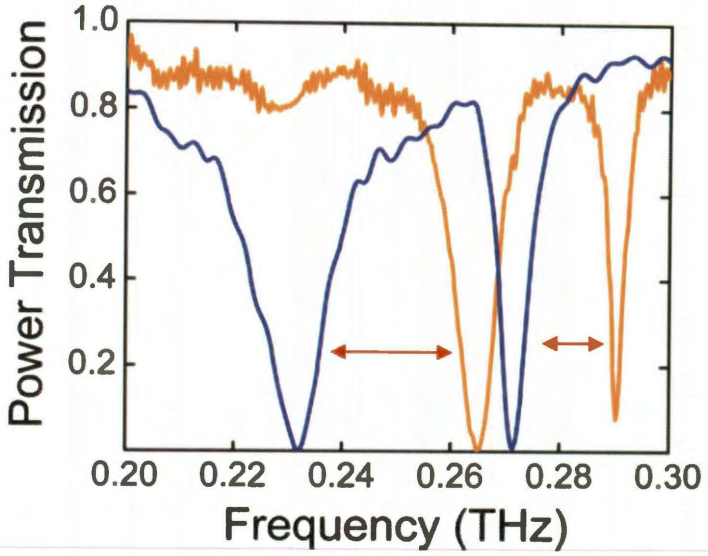

Figure 3-43 Experimental power transmission spectra for the empty waveguide (orange) and the waveguide with both grooves filled with C14 (blue). The resonant shifts are marked with red arrows.

As the next test, transmission spectra were compared for three filling scenarios: (1) C14 in both grooves (Figure 3-44 blue curves) (2) C10 in Groove 1 and C14 in Groove 2 (Figure 3-44 (top), red) and (3) C14 in Groove 1 and C10 in Groove 2 (Figure 3-44(bottom), red). In Figure 3-44, each experimental data set differs only in the filling material of one of the grooves, while each pair of transmission spectra differs only in the frequency of the resonance arising from that groove. This clearly demonstrates the independent nature of the resonances. When the same groove is filled with C14 in two different experimental sets, the resonances overlap with very little variation. Table 3-5 illustrates this independence quantitatively by comparing the shifts in resonant frequency for each groove and for each alkane fill. The small offset visible in the overlap of the spectra in Figure 3-44

is a result of the differences in the resonances for the empty PPWG as discussed earlier – the resonance *shifts* are almost identical.

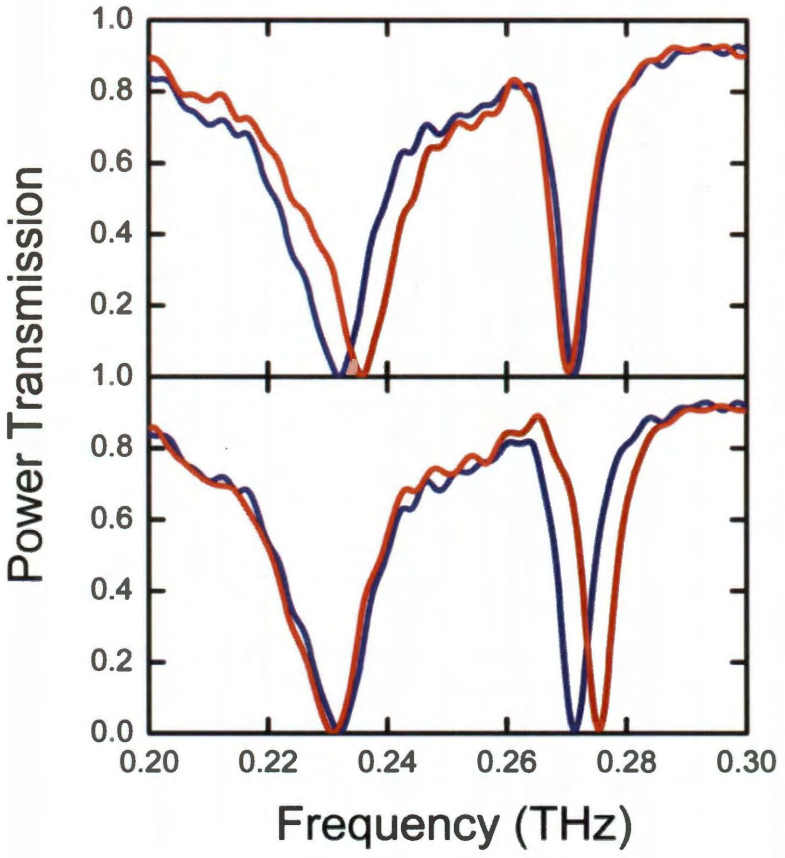

Figure 3-44 Power transmission spectra for the PPWG with alkanes filling both grooves. In both plots, blue curves represent the transmission when both grooves are filled with C14. (top) Red curve: Groove 1 filled with C10, Groove 2 filled with C14. (bottom) Red curve: Groove 1 filled with C14, Groove 2 filled with C10.

Material in Groove 1	Freq. Shift of Resonance 1 (GHz)	Material in Groove 2	Freq. Shift of Resonance 2 (GHz)
C10	30.3	C14	20.4
C14	35.0	C14	20.5
C14	35.7	C10	16.6

Table 3-5 Frequency shifts for the spectra presented in Figure 3-44

To extend this test, we expand our test liquids to include the full range of alkanes from C8-C16. For one series of data sets, Groove 1 was filled with a substance from the C8-C16 alkanes, while C14 filled Groove 2. By using a consistent substance in one groove, its resonant peak could be monitored to see if it was affected by the filling fluid in the other groove. The same method was applied in a second series of data sets with the constant material, C14, in Groove 1 and the range of C8-C16 in Groove 2. Figure 3-45 summarizes these results. We observe that for the groove with the variable liquid filling, the shift in the resonant frequency increases as the refractive index increases, whereas the frequency shift from the groove with a consistent filling material stays constant.

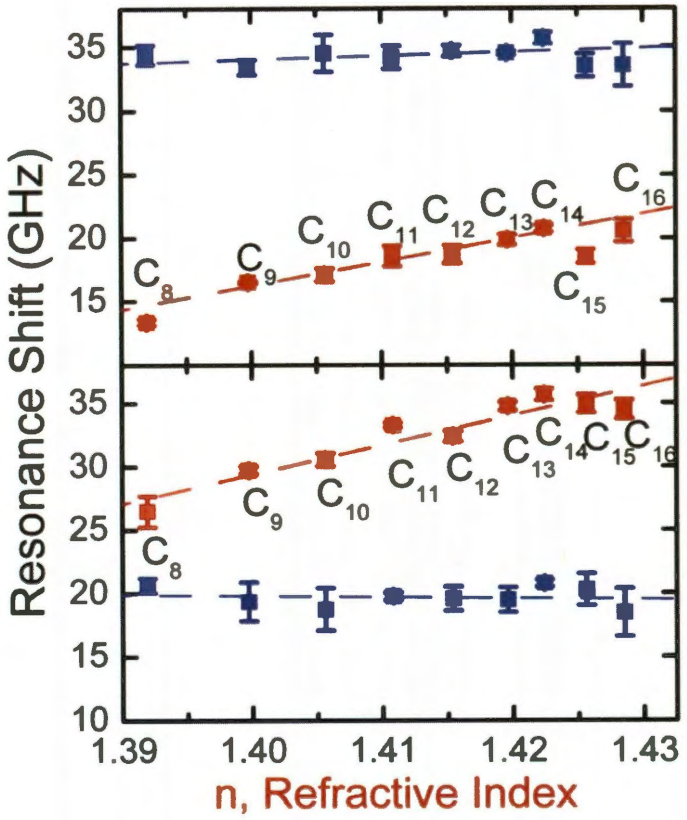

Figure 3-45 Plots of the shift in resonant frequency caused by liquid filling in the grooves vs. refractive index of the liquid. (Top) Groove 1 is consistently filled with C14 while Groove 2 is filled with varying alkanes, and the shifts of both resonances are plotted versus the index of the material in Groove 2. (Bottom) Groove 2 is consistently filled with C14 while the material in Groove 1 varies and the shifts are plotted versus the index of the material in Groove 1. The dotted lines indicate linear fits of the data.

We note that the two grooves have somewhat different sensitivities to small changes in the refractive index of the filling liquid. In particular, the frequency shifts are higher for Groove 1 (the larger groove) than for Groove 2, although both grooves display a roughly linear relationship between resonant shift and refractive index. Similar to our earlier work [1], this type of sensor has a high sensitivity as expressed in the resonance shift per refractive index unit (RIU). Using linear fits (dashed lines),

for the range of index values spanned by the liquid alkanes the sensitivity is $\Delta f/\Delta n$ = 225 GHz/RIU for Groove 1 and $\Delta f/\Delta n$ = 170 GHz/RIU for Groove 2. Converting frequency into wavelength gives a sensitivity of $\Delta\lambda/\Delta n$ = $1.21\text{x}10^6$ nm/RIU for Groove 1, and $\Delta\lambda/\Delta n$ = $6.77\text{x}10^5$ nm/RIU for Groove 2. These values are slightly higher than the measurement of $3.7\text{x}10^5$ nm/RIU for the single-channel sensor, indicating no loss in sensitivity due to multiplexing [1]. These values are more than an order of magnitude higher than the previous highest (theoretical) value reported, that of a photonic-crystal-based THz microfluidic sensor [20]. From these sensitivities and the standard deviations of the experimental data (Figure 3-45, error bars), we estimate the minimum detectable RI difference to be $\Delta n \sim 10^{-2}$ RIU, while the theoretical resolution as limited by the spectral resolution of the time-domain THz system (0.6 GHz) would be on the order of 10^{-3} RIU.

We compare this experimental sensitivity to that predicted by mode-matching analysis using the techniques described in Section 3.7.1 above. To do this we must first calibrate the height of the fill in each groove – while we know the volume to high accuracy, we need to translate this into a height in microns. We do this by averaging all data sets with C14 in Groove 1 to obtain the most precise measurement for the resonant shift (34.3 GHz), and then by obtaining the predicted shift for a wide range of fill heights (from empty at 0 μm to a perfect fill of 406 μm to an overfill of 500 μm) and matching the resonant response, using plots similar to that in Figure 3-38. For the 711 x 406 μm groove, a fill height of 354 μm is required to match the 34.3 GHz resonant shift, meaning that a fill of 11.5 μL leads to a slight

underfill of the groove. The same procedure is done for Groove 2, requiring a slight overfill of 419 μm to match the 19.4 GHz resonant shift. With these fill heights, we perform mode-matching analysis with all the various material fills in the two grooves to match the experimental data sets and plot the results in Figure 3-46 (solid green lines.) The sensitivities predicted by mode-matching analysis are slightly lower, 103 GHz/RIU for Groove 1 and 94 GHz/RIU for Groove 2, but the general trends agree reasonably well with the experimental data.

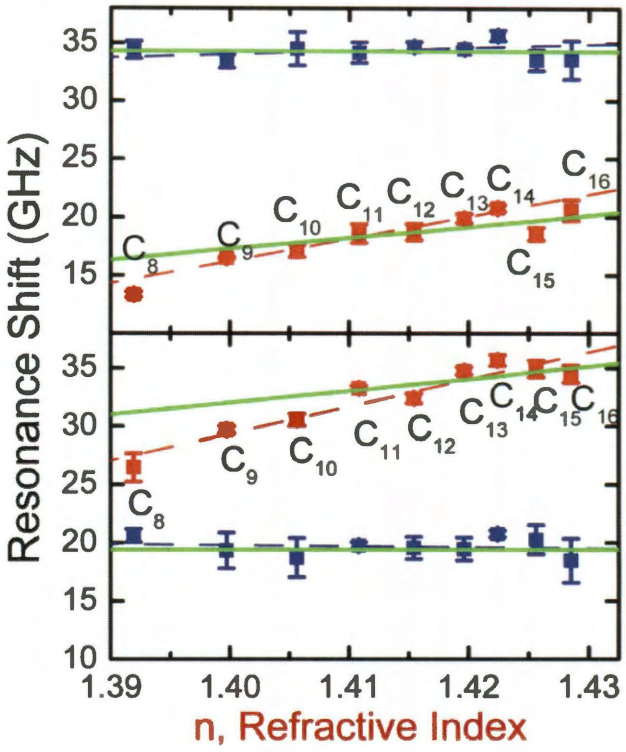

Figure 3-46 Plots of the shift in resonant frequency caused by liquid filling in the grooves vs. refractive index of the liquid. Squares are experimental data, dashed lines are linear fits to the data, and the solid green lines are the results from mode-matching analysis.

In order for this system to serve as a useful microfluidic sensor, several experimental issues remain to be addressed. The relationships of resonance shift to varying refractive index in the plots above are not precisely linear to within the error bars though they show a clear linear trend, while the "unchanging" resonance does exhibit some fluctuation between the different data sets. These fluctuations in the data could have occurred due to several factors. Since the waveguide is disassembled after each data set for cleaning, it may not be reassembled in exactly the same manner, causing slight variations in the plate spacing and alignment which correspond in turn to slight variations in the observed resonant shift. The effects of evaporation must also be taken into consideration for the lighter alkanes C8, C9, and C10. To minimize evaporation effects a shorter time window was sometimes employed, but this limited the spectral resolution of the measured transmission spectra. In addition, the fill volume must be controlled very carefully and small variations could result in considerable fluctuation in the resonant shift for near-full volumes.

These factors will all be important for any industrial or experimental implementation of the PPWG multichannel sensor geometry, particularly the repeatability of the fill volume. Many of these issues could be avoided by including an enclosed liquid channel in the structure, for example with a thin Teflon cap covering the resonator to prevent evaporation and provide a well-defined fill volume, and improvements in the repeatability of this system are an obvious goal for further work on multichannel sensing using a grooved PPWG.

3.7.3. Resonant Splitting Sensor

We also consider the performance of a sensor based on the resonant splitting design presented in Section 3.6.2, with two grooves of identical 460 by 412 μm geometry separated by 0.58 mm (diagram in Figure 3-30). Because the resonance features of this design arise from both grooves equally, the potential of this sensor is less intuitively obvious than that of the multichannel design. Here we use mode-matching analysis to test the response of the sensor to dielectric materials in one or both grooves.

First, we analyze the case where only one groove at a time is filled with a dielectric while the other is empty. Figure 3-47 below shows the power transmission for three such examples, in which both grooves are empty (blue), in which one groove is filled with a material with an index of 1.3 (red), and in which one groove is filled with a material of index 1.45 (green). The results are identical regardless of which groove it is being filled.

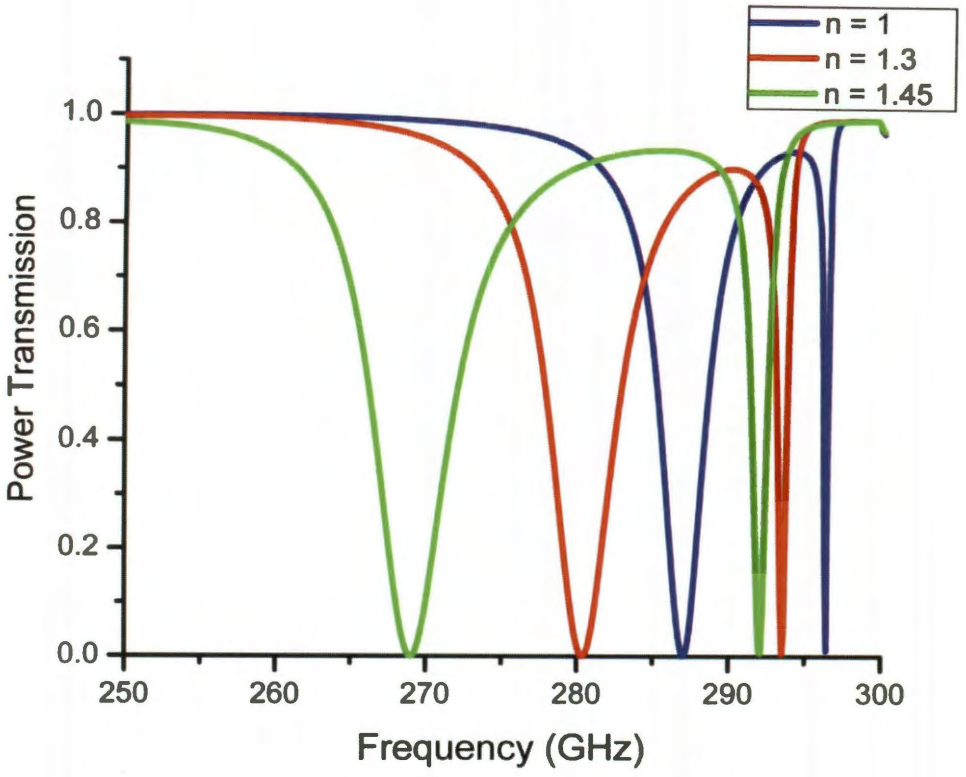

Figure 3-47 Power transmission spectra from mode-matching analysis for the resonant-splitting waveguide sensor. Curves are for the case in which both grooves are empty (blue), one groove is filled with a material of index 1.3 (red), and one groove is filled with a material of index 1.45 (green).

The curves indicate that both resonances shift to lower frequencies when one groove is filled, but with a stronger dependence in the lower-frequency resonant feature. This result can be explored by plotting the resonant frequencies of both features over the range of refractive indices filling the groove (Figure 3-48). The high-frequency resonance demonstrates a linear relationship with the refractive index, while the low-frequency resonance has a quadratic relationship similar to that of the single groove.

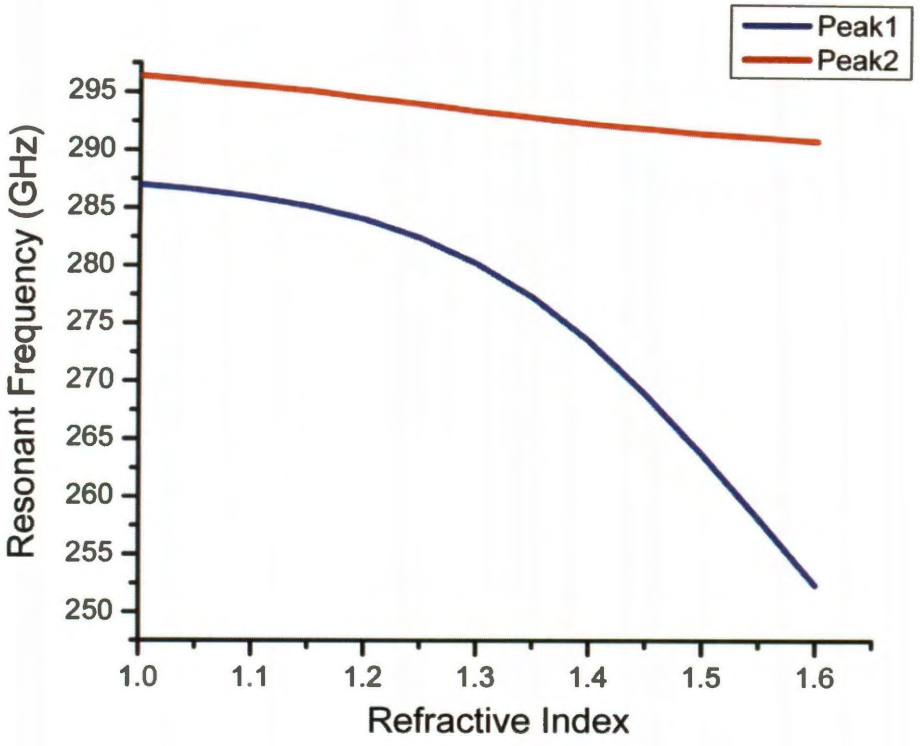

Figure 3-48 Resonant frequency of the lower-frequency resonance (blue) and the higher-frequency resonance (red) when one groove is filled with materials with a range of refractive indices.

To fully compare the performance to the experimental tests of the single groove and multichannel waveguides, we also obtain results from mode-matching analysis specifically for the straight-chain alkane test materials. The shifts in the resonant frequencies of both peaks when one groove is filled with each alkane in turn are plotted in Figure 3-49 below.

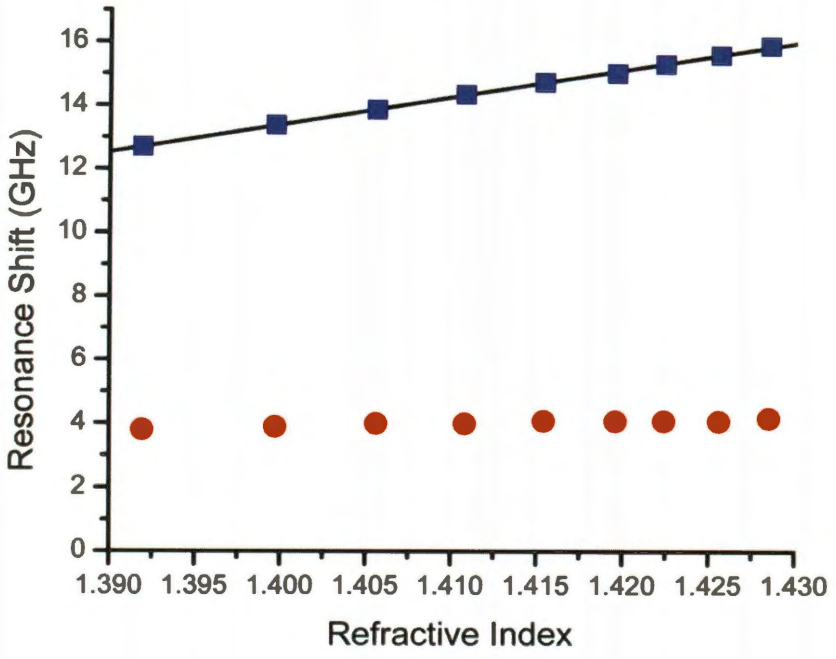

Figure 3-49 Plot of the shift in frequency vs. refractive index for both the low-frequency (blue squares) and high-frequency (red circles) resonances when one groove is filled with a series of alkanes. The black line is a linear fit of the shift in the low-frequency resonance.

A linear fit of the resonant shifts for the lower-frequency resonance yields an estimate for the sensitivity of the resonant-splitting waveguide with one groove filled: 89 GHz/RIU.

It is also possible to employ the resonant-splitting waveguide as a sensor with both grooves filled, either with the same or with different materials. We first consider the case where both grooves are filled with the same material, with a wide range of refractive indices. Figure 3-50 plots the power transmission spectra for both grooves empty (blue), filled with a material of index 1.3 (red), and filled with a material of index 1.45 (green.)

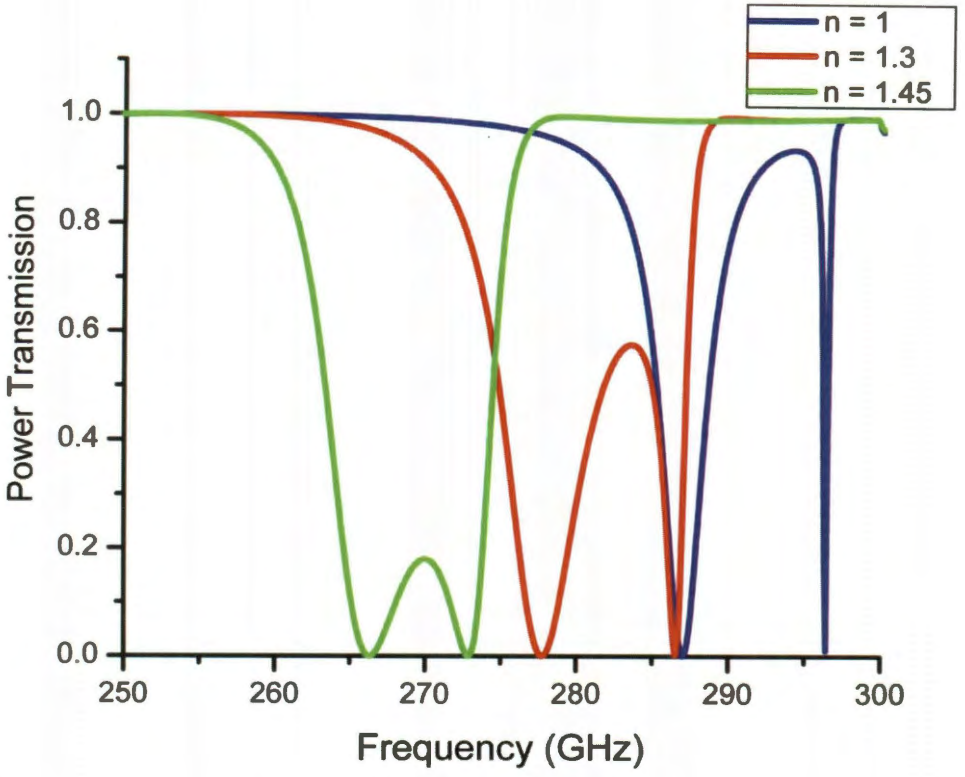

Figure 3-50 Power transmission spectra from mode-matching analysis for the resonant-splitting waveguide sensor. Curves are for the case in which both grooves are empty (blue), both grooves are filled with a material of index 1.3 (red), and both grooves are filled with a material of index 1.45 (green).

As before, both resonances shift due to the dielectric filling. However, in this case it is the higher-frequency resonance that exhibits a stronger dependence on the refractive index, causing the two resonances to increasingly overlap for higher indices. This relationship is clearly visible in the plot of both resonant frequencies versus the refractive index filling both grooves (Figure 3-51). Contrary to the situation where only one groove was filled, when both grooves are filled both resonances show a quadratic dependence on the refractive index, with the higher-frequency resonance exhibiting a stronger dependence.

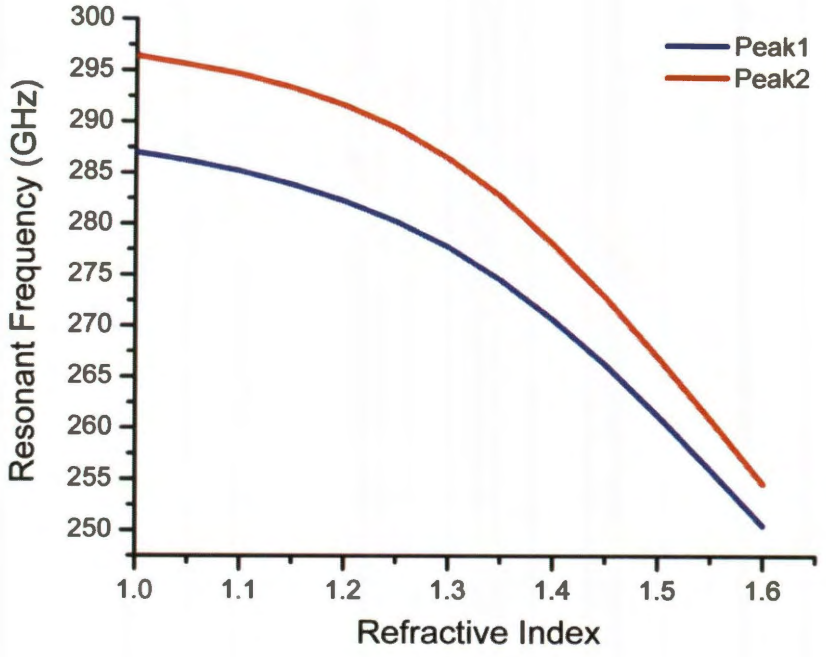

Figure 3-51 Resonant frequency of the lower-frequency resonance (blue) and the higher-frequency resonance (red) when both grooves are filled with materials with a range of refractive indices.

We again consider the specific case of the straight-chain alkanes. When both grooves are filled with the same alkane, both resonances exhibit a roughly linear dependence on refractive index, with a slightly steeper relationship for the higher-frequency resonance. The shifts in the resonant frequencies of both peaks when both grooves are filled with each alkane in turn are plotted in Figure 3-52 below.

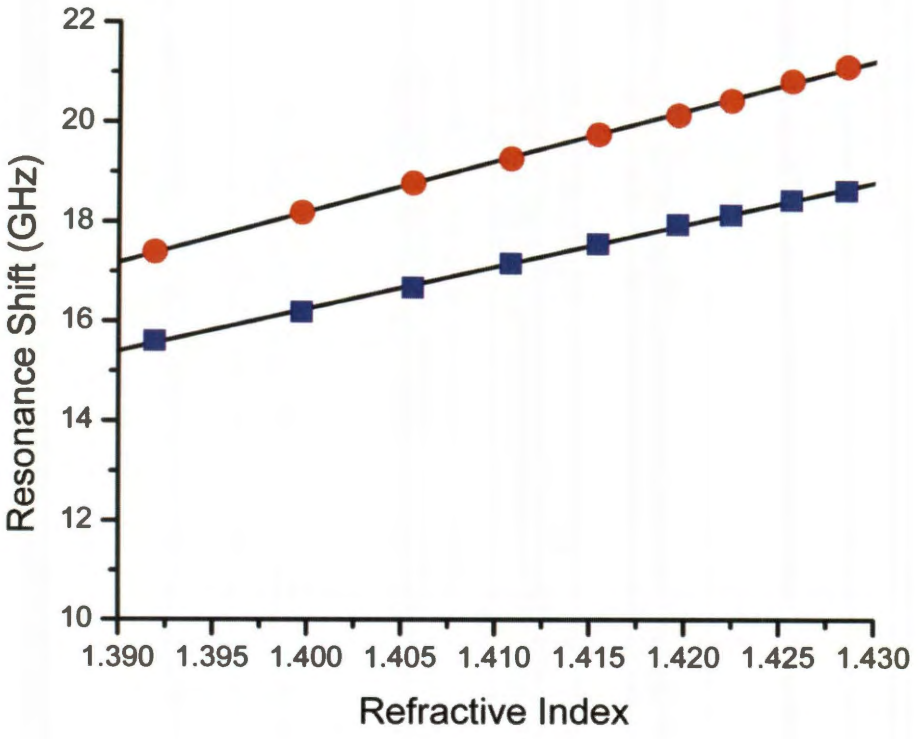

Figure 3-52 Plot of the shift in frequency vs. refractive index for both the low-frequency (blue squares) and high-frequency (red circles) resonances when both grooves are filled with a series of alkanes. The black lines are linear fits.

Linear fits of the resonant shifts for both resonances yield an estimate for the sensitivity of the resonant-splitting waveguide with both grooves filled with the same material: 86 GHz/RIU for the low-frequency resonance and 103 GHz/RIU for the high-frequency resonance.

The sensitivities obtained for the resonant-splitting waveguide sensor are on the order of the sensitivities predicted by mode-matching analysis for the multichannel design and significantly lower than those observed experimentally for the multichannel sensor. However, this is balanced by the increased resolution of the system. The resolution of a resonant sensor is determined in part by the

smallest change in resonant frequency that is measurable, which is in turn a function of the linewidth of the resonance – the narrower the resonance, the smaller the change that can be detected, and so the smaller a change in refractive index that can be measured. While the resonant-splitting sensor may not have has only a 103 GHz/RIU sensitivity compared to the 225 GHz/RIU sensitivity observed for the 711 by 406 μm groove, the linewidth for that particular resonant feature is only 1 GHz as compared to 8.3 GHz, so the refractive index resolution will in fact be several times greater.

As a result, we conclude that the resonant-splitting waveguide design has significant potential as a sensor. Further work would obviously include experimental verification of its performance, optimization of the two-groove design, and adaptation towards real-world implementation similar to that required of the multichannel waveguide sensor.

Chapter 4

Conclusions

In this dissertation, the properties and capabilities of the metal wire waveguide and parallel-plate waveguide were investigated using a combination of experimental data, finite element method simulation, and mode-matching analysis.

For the metal wire waveguide, the large beam extent was shown to result in increased coupling over a range of geometries. End-to-end coupling of wire waveguide sections was shown to be significant, even at very large separations between the two sections, and could be improved by the inclusion of a lens in the gap. The wire waveguide also exhibits a high tolerance for angular offsets between waveguide sections. A mirror was demonstrated as an effective high-transmission method for 90° directional changes. Long gradual bends were also investigated for achieving directional changes, with optimal transmission observed at a radius of

curvature on the same order as the spatial extent of the propagating beam. As a result, the formalism for the bending loss on a curved wire waveguide was refined. These results have implications for future applications of wire waveguides, in terms of optimizing coupling and achieving directional changes by incorporating a mirror or by choosing the optimal bending radius.

The superfocusing of terahertz radiation at the end of a tapered wire waveguide was also investigated through experiment and simulation. The axial component of the electric field was demonstrated to have three-dimensional subwavelength confinement ($\lambda/100$). The presence of the measuring probe was determined to have a significant effect on the measured confinement, which has significant implications for the use of the tapered wire as a near-field imaging probe. Future near-field imaging implementations should also consider the use of the axial field component, due to its superior confinement characteristics in comparison to the radial component.

The grooved TE-mode parallel-plate waveguide was also studied in depth. Experimental data provided a framework for determining the origin of the observed resonant behavior of the waveguide. Mode-matching analysis proved to be a powerful technique for analyzing the behavior of the grooved PPWG, including when the groove is filled with a dielectric for sensing applications. Designs of the PPWG with two grooves were studied, both in coupled and non-coupled configurations. When the two grooves are not coupled, they act as independent channels for microfluidic sensing. When the grooves are coupled, splitting of the

resonance can be observed. Both the coupled and non-coupled two-groove geometries were proposed as high-sensitivity microfluidic sensors. The multichannel (non-coupled) design was experimentally demonstrated to have two independent sensing channels. The resonant splitting (coupled) design was shown through mode-matching analysis to have comparable sensitivity and high resolution. Future work with the grooved parallel-plate waveguide includes improving the repeatability of the experimental procedure, improving the sensitivity and resolution, expanding the range of testing materials, and moving towards real-world sensing applications.

References

1. Mendis, R., et al., *Terahertz Microfluidic Sensor Based on a Parallel-Plate Waveguide Resonant Cavity.* Appl. Phys. Lett., 2009. **95**: p. 171113.

2. Beard, M.C., G.M. Turner, and C.A. Schmuttenmaer, *Terahertz Spectroscopy.* J. Phys. Chem. B, 2002. **106**: p. 7146-7159.

3. Markelz, A.G., A. Roitberg, and E.J. Heilweil, *Pulsed Terahertz Spectroscopy of DNA, Bovine Serum Albumin and Collagen between 0.1 and 2.0 THz.* Chem. Phys. Lett., 2000. **320**(1-2): p. 42-48.

4. Davies, A.G., et al., *Terahertz Spectroscopy of Explosives and Drugs.* Materials Today, 2008. **11**(3): p. 18-26.

5. Beard, M.C., G.M. Turner, and C.A. Schmuttenmaer, *Subpicosecond Carrier Dynamics in Low-Temperature Grown GaAs as Measured by Time-Resolved Terahertz Spectroscopy.* J. Appl. Phys., 2001. **90**: p. 5915.

6. Grischkowsky, D., et al., *Far-Infrared Time-Domain Spectroscopy with Terahertz Beams of Dielectrics and Semiconductors.* J. Opt. Soc. Am. B, 1990. **7**(10): p. 2006-2015.

7. Schmuttenmaer, C.A., *Exploring Dynamics in the Far-Infrared with Terahertz Spectroscopy.* Chem. Rev., 2004. **104**: p. 1759-1779.

8. Chan, W.L., J. Deibel, and D.M. Mittleman, *Imaging with Terahertz Radiation.* Rep. Prog. Phys., 2007. **70**: p. 1325-1379.

9. Zhan, H., et al., *The Metal-Insulator Transition in VO_2 Studied Using Terahertz Apertureless Near-Field Microscopy.* Appl. Phys. Lett., 2007. **91**: p. 162110.

10. Zhong, H., et al., *Nondestructive Defect Identification with Terahertz Time-of-Flight Tomography.* IEEE Sens. J., 2005. **5**(2): p. 203-208.

11. Jackson, J.B., et al., *Terahertz Imaging for Non-Destructive Evaluation of Mural Paintings.* Opt. Commun., 2008. **281**(4): p. 527-532.

12. Jackson, J.B., et al., *Terahertz Pulse Imaging for Tree-Ring Analysis: A Preliminary Study for Dendrochronology Applications.* Meas. Sci. Technol., 2009. **20**: p. 075502.

13. Zhong, Z., et al., *Terahertz Time-Domain Measurement of Ballistic Electron Resonance in a Single-Walled Carbon Nanotube.* Nature Nanotechnology, 2008. **3**: p. 201-205.

14. Jansen, C., et al., *The Impact of Reflections from Stratified Building Materials on the Wave Propagation in Future Indoor Terahertz Communication Systems.* IEEE Trans. Antennas Propag., 2008. **56**(5): p. 1413-1418.

15. Frankel, M.Y., et al., *Terahertz Attenuation and Dispersion Characteristics of Coplanar Transmission Lines.* IEEE Trans. Microwave Theory Tech., 1991. **39**(6): p. 910-916.

16. Gallot, G., et al., *Terahertz Waveguides.* J. Opt. Soc. Am. B, 2000. **17**(5): p. 851-863.

17. Jamison, S.P., R.W. McGowan, and D. Grischkowsky, *Single-Mode Waveguide Propagation and Reshaping of Sub-Ps Terahertz Pulses in Sapphire Fibers.* Appl. Phys. Lett., 2000. **76**(15): p. 1987-1989.

18. Han, H., et al., *Terahertz Pulse Propagation in a Plastic Photonic Crystal Fiber.* Appl. Phys. Lett., 2002. **80**: p. 2634.

19. Kurt, H. and D.S. Citrin, *Photonic Crystals for Biochemical Sensing in the Terahertz Region.* Appl. Phys. Lett., 2005. **87**: p. 041108.

20. Kurt, H. and D.S. Citrin, *Coupled-Resonator Optical Waveguides for Biochemical Sensing of Nanoliter Volumes of Analyte in the Terahertz Region.* Appl. Phys. Lett., 2005. **87**: p. 241119.

21. Bingham, A.L. and D.R. Grischkowsky, *Terahertz 2-D Photonic Crystal Waveguides.* IEEE Microw. Wirel. Compon. Lett., 2008. **18**(7): p. 428-430.

22. Wang, K. and D.M. Mittleman, *Metal Wires for Terahertz Wave Guiding.* Nature, 2004. **432**: p. 376-379.

23. Wang, K., A. Barkan, and D.M. Mittleman, *Propagation Effects in Apertureless Near-Field Optical Antennas.* Appl. Phys. Lett., 2004. **84**(2): p. 305-307.

24. Wang, K. and D.M. Mittleman, *Guided Propagation of Terahertz Pulses on Metal Wires.* J. Opt. Soc. Am. B, 2005. **22**(9): p. 2001-2008.

25. Mendis, R. and D. Grischkowsky, *Undistorted Guided-Wave Propagation of Subpicosecond Terahertz Pulses.* Opt. Lett., 2001. **26**(11): p. 846-848.

26. Zhan, H., R. Mendis, and D.M. Mittleman, *Superfocusing Terahertz Waves Below $\lambda/250$ Using Plasmonic Parallel-Plate Waveguides.* Optics Express, 2010. **18**(9): p. 9643-9650.

27. Liu, J., et al., *A Tapered Parallel-Plate-Waveguide Probe for THz Near-Field Reflection Imaging.* Appl. Phys. Lett., 2012. **100**: p. 031101.

28. Melinger, J.S., et al., *Guided-Wave Terahertz Spectroscopy of Molecular Solids.* J. Opt. Soc. Am. B, 2009. **26**(9): p. A79-A89.

29. Zhang, J. and D. Grischkowsky, *Waveguide Terahertz Time-Domain Spectroscopy of Nanometer Water Layers.* Opt. Lett., 2004. **29**(14): p. 1617-1619.

30. Awad, M. and R.A. Cheville, *Transmission Terahertz Waveguide-Based Imaging Below the Diffraction Limit.* Appl. Phys. Lett., 2005. **86**: p. 221107.

31. Deibel, J.A., et al., *Enhanced Coupling of Terahertz Radiation to Cylindrical Wire Waveguides.* Optics Express, 2006. **14**(1): p. 279-290.

32. Deibel, J.A., et al., *Finite-Element Method Simulations of Guided Wave Phenomena at Terahertz Frequencies.* Proc. IEEE, 2007. **95**(8): p. 1624-1640.

33. Astley, V., et al., *Bending and Coupling Losses in Terahertz Wire Waveguides.* Opt. Lett., 2010. **35**(4): p. 553-555.

34. Astley, V., R. Mendis, and D.M. Mittleman, *Characterization of Terahertz Field Confinement at the End of a Tapered Metal Wire Waveguide.* Appl. Phys. Lett., 2009. **95**: p. 031104.

35. Jeon, T.-I., J. Zhang, and D. Grischkowsky, *THz Sommerfeld Wave Propagation on a Single Metal Wire.* Appl. Phys. Lett., 2005. **86**: p. 161904.

36. Wächter, M., M. Nagel, and H. Kurz, *Frequency-Dependent Characterization of THz Sommerfeld Wave Propagation on Single-Wires.* Optics Express, 2005. **13**(26): p. 10815-10822.

37. Wang, K. and D.M. Mittleman, *Dispersion of Surface Plasmon Polaritons on Metal Wires in the Terahertz Frequency Range.* Phys. Rev. Lett., 2006. **96**: p. 157401.

38. Valk, N.C.v.d. and P.C. Planken, *Effect of a Dielectric Coating on Terahertz Surface Plasmon Polaritons on Metal Wires.* Appl. Phys. Lett., 2005. **87**: p. 071106.

39. Walther, M., M.R. Freeman, and F.A. Hegmann, *Metal-Wire Terahertz Time-Domain Spectroscopy.* Appl. Phys. Lett., 2005. **87**: p. 261107.

40. Liang, H., S. Ruan, and M. Zhang, *Terahertz Surface Wave Propagation and Focusing on Conical Metal Wires.* Optics Express, 2008. **16**(22): p. 18241-18248.

41. Awad, M., M. Nagel, and H. Kurz, *Tapered Sommerfeld Wire Terahertz near-Field Imaging.* Appl. Phys. Lett., 2009. **94**: p. 051107.

42. Shvets, G., et al., *Guiding, Focusing, and Sensing on the Subwavelength Scale Using Metallic Wire Arrays.* Phys. Rev. Lett., 2007. **99**: p. 053903.

43. Guillet, J.-P., et al., *Continuous-Wave Scanning Terahretz Near-Field Microscope.* Microwave and Opt. Tech. Lett., 2011. **53**(3): p. 580-582.

44. Stratton, J.A., *Electromagnetic Theory*1941, New York: McGraw-Hill.

45. Goubau, G., *Surface Waves and Their Application to Transmission Lines.* J. Appl. Phys., 1950. **21**: p. 1119-1128.

46. King, M.J. and J.C. Wiltse, *Surface-Wave Propagation on Coated or Uncoated Metal Wires at Millimeter Wavelengths.* IRE Trans. Antennas Propag., 1962. **10**: p. 246-254.

47. Wang, K., *Novel Devices and Systems for Terahertz Spectroscopy and Imaging (Phd Thesis)*, 2006, Rice University: Houston.

48. Ashcroft, N.W. and N.D. Mermin, *Solid State Physics* 1976: Brooks/Cole.

49. Sobel, F., F.L. Wentworth, and J.C. Wiltse, *Quasi-Optical Surface Waveguide and Other Components for the 100- to 300-Gc Region.* IRE Trans. Microwave Theory Tech., 1961. **9**: p. 512-518.

50. Stockman, M.I., *Nanofocusing of Optical Energy in Tapered Plasmonic Waveguides.* Phys. Rev. Lett., 2004. **93**(13): p. 137404.

51. Deibel, J.A., et al., *Frequency-Dependent Radiation Patterns Emitted by THz Plasmons on Finite Length Cylindrical Metal Wires.* Optics Express, 2006. **14**(19): p. 8772-8778.

52. Nazarov, M., et al., *THz Surface Plasmon Jump between Two Metal Edges.* Opt. Commun., 2007. **277**: p. 33-39.

53. Ruffin, A.B., et al., *Direct Observation of the Gouy Phase Shift with Single-Cycle Terahertz Pulses.* Phys. Rev. Lett., 1999. **83**(17): p. 3410-3413.

54. Marcatili, E.A.J. and S.E. Miller, *Improved Relations Describing Directional Control in Electromagnetic Wave Guidance.* Bell Syst. Tech. J., 1969. **48**: p. 2161-2188.

55. Keilmann, F., *FIR Microscopy.* Infrared Phys. Technol., 1995. **36**(1): p. 217-224.

56. Maier, S.A., et al., *Local Detection of Electromagnetic Energy Transport Below the Diffraction Limit in Metal Nanoparticle Plasmon Waveguides.* Nature Mater., 2003. **2**: p. 229-232.

57. Yatsui, T., M. Kourogi, and M. Ohtsu, *Plasmon Waveguide for Optical Far/Near-Field Conversion.* Appl. Phys. Lett., 2001. **79**: p. 4583.

58. Krenn, J.R., et al., *Non-Diffraction-Limited Light Transport by Gold Nanowires.* Europhys. Lett., 2002. **60**(5): p. 663-669.

59. Pile, D.F. and D.K. Gramotnev, *Adiabatic and Nonadiabatic Nanofocusing of Plasmons by Tapered Gap Plasmon Waveguides.* Appl. Phys. Lett., 2006. **89**: p. 041111.

60. Janunts, N.A., et al., *Excitation and Superfocusing of Surface Plasmon Polaritons on a Silver-Coated Optical Fiber Tip.* Opt. Commun., 2005. **253**: p. 118-124.

61. Verhagen, E., A. Polman, and L.K. Kuipers, *Nanofocusing in Laterally Tapered Plasmonic Waveguides.* Optics Express, 2008. **16**(1): p. 45-57.

62. Maier, S.A., et al., *Terahertz Surface Plasmon-Polariton Propagation and Focusing on Periodically Corrugated Metal Wires.* Phys. Rev. Lett., 2006. **97**: p. 176805.

63. Keilmann, F., *Surface-Polariton Propagation for Scanning near-Field Optical Microscopy Application.* J. Microsc., 1999. **194**: p. 567.

64. Ropers, C., et al., *Light Confinement at Ultrasharp Metallic Tips.* Jpn. J. Appl. Phys., 2008. **47**(7): p. 6051-6054.

65. Goncharenko, A.V., J.-K. Wang, and Y.-C. Chang, *Electric near-Field Enhancement of a Sharp Semi-Infinite Conical Probe: Material and Cone Angle Dependence.* Phys. Rev. B, 2006. **74**: p. 235442.

66. Ji, Y.B., et al., *Enhancement of the Detection of THz Sommerfeld Wave Using a Conical Wire Waveguide.* Optics Express, 2008. **16**(1): p. 271-278.

67. Valk, N.C.J.v.d. and P.C.M. Planken, *Electro-Optic Detection of Subwavelength Terahertz Spot Sizes in the near Field of a Metal Tip.* Appl. Phys. Lett., 2002. **81**: p. 1558.

68. Planken, P.C.M., C.E.W.M.v. Rijmenam, and R.N. Schouten, *Opto-Electronic Pulsed THz Systems.* Semicond. Sci. Tech., 2005. **20**: p. S121-S127.

69. Astley, V., et al., *A Study of Background Signals in Terahertz Apertureless Near-Field Microscopy and Their Use for Scattering-Probe Imaging.* J. Appl. Phys., 2009. **105**: p. 113117.

70. Astley, V., *A Study of Background Signals in Terahertz Apertureless Near-Field Microscopy and Their Use for Scattering-Probe Imaging (MS Thesis)*, 2009, Rice University: Houston.

71. Huber, A.J., et al., *Terahertz near-Field Nanoscopy of Mobile Carriers in Single Semiconductor Nanodevices.* Nano. Lett., 2008. **8**(11): p. 3766-3770.

72. Knoll, B. and F. Keilmann, *Enhanced Dielectric Contrast in Scattering-Type Scanning near-Field Optical Microscopy.* Opt. Commun., 2000. **182**: p. 321-328.

73. Wang, K. and D.M. Mittleman, *Antenna Effects in Terahertz Apertureless near-Field Optical Microscopy.* Appl. Phys. Lett., 2004. **85**(14): p. 2715-2717.

74. Cory, H., et al., *Electric Field Intensity Variation in the Vicinity of a Perfectly Conducting Conical Probe: Application to near-Field Microscopy.* Microwave and Opt. Tech. Lett., 1998. **18**(2): p. 120-124.

75. Hecht, B., et al., *Facts and Artifacts in Near-Field Optical Microscopy.* J. Appl. Phys., 1997. **81**: p. 2492.

76. Astley, V., et al., *Analysis of Rectangular Resonant Cavities in Terahertz Parallel-Plate Waveguides.* Opt. Lett., 2011. **36**(1452-1454).

77. Astley, V., et al., *Terahertz Multichannel Microfluidic Sensor Based on Parallel-Plate Waveguide Resonant Cavities.* Appl. Phys. Lett., 2012. **submitted**.

78. Hassani, A., A. Dupuis, and M. Skorobogatiy, *Surface-Plasmon-Resonance-Like Fiber-Based Sensor at Terahertz Frequencies.* J. Opt. Soc. Am. B, 2008. **25**(10): p. 1771-1775.

79. You, B., et al., *Subwavelength Film Sensing Based on Terahertz Anti-Resonant Reflecting Hollow Waveguides.* Optics Express, 2010. **18**(18): p. 19353.

80. Bingham, A.L. and D. Grischkowsky, *Terahertz Two-Dimensional High-Q Photonic Crystal Waveguide Cavities.* Opt. Lett., 2008. **33**(4): p. 348-350.

81. Yee, C.M. and M.S. Sherwin, *High-Q Terahertz Microcavities in Silicon Photonic Crystal Slabs.* Appl. Phys. Lett., 2009. **94**: p. 154104.

82. Gerhard, M., C. Imhof, and R. Zengerle, *Compact Three-Dimensional Terahertz Resonators Based on Periodically Corrugated Metallic Slit Waveguides.* J. Appl. Phys., 2010. **108**: p. 026102.

83. Yoshida, S., et al., *Terahertz Sensing of Thin Poly(ethylene terephthalate) Film Thickness Using a Metallic Mesh.* Appl. Phys. Express, 2009. **2**: p. 012301.

84. Debus, C. and P.H. Bolivar, *Frequency Selective Surfaces for High Sensitivity Terahertz Sensing.* Appl. Phys. Lett., 2007. **91**: p. 184102.

85. O'Hara, J.F., et al., *Thin-Film Sensing with Planar Terahertz Metamaterials: Sensitivity and Limitations.* Optics Express, 2008. **16**(3): p. 1786.

86. Chiam, S.-Y., et al., *Increased Frequency Shifts in High Aspect Ratio Terahertz Split Ring Resonators.* Appl. Phys. Lett., 2009. **94**: p. 064102.

87. Nagel, M., P.H. Bolivar, and H. Kurz, *Modular Parallel-Plate THz Componenents for Cost-Efficient Biosensing Systems.* Semicond. Sci. Tech., 20. **2005**: p. S281-S285.

88. Bingham, A.L. and D. Grischkowsky, *High Q, One-Dimensional Terahertz Photonic Waveguides.* Appl. Phys. Lett., 2007. **90**: p. 091105.

89. Harsha, S.S., N. Laman, and D. Grischkowsky, *High-Q Terahertz Bragg Resonances within a Metal Parallel Plate Waveguide.* Appl. Phys. Lett., 2009. **94**: p. 091118.

90. Mendis, R. and D.M. Mittleman, *Comparison of the Lowest-Order Transverse-Electric (TE1) and Transverse-Magnetic (TEM) Modes of the Parallel-Plate Waveguide for Terahertz Pulse Applications.* Optics Express, 2009. **17**(17): p. 14839-14850.

91. Balanis, C.A., *Advanced Engineering Electromagnetics*1989, New York: Wiley.

92. Mendis, R. and D.M. Mittleman, *An Investigation of the Lowest-Order Transverse-Electric (TE1) Mode of the Parallel-Plate Waveguide for THz Pulse Propagation.* J. Opt. Soc. Am. B, 2009. **26**(9): p. A6-A13.

93. Mendis, R. and D.M. Mittleman, *Whispering-Gallery-Mode Terahertz Pulse Propagation on a Curved Metallic Plate.* Appl. Phys. Lett., 2010. **97**: p. 031106.

94. Mendis, R. and D.M. Mittleman, *A 2-D Artificial Dielectric with 0 <= n < 1 for the Terahertz Region.* IEEE Trans. Microwave Theory Tech., 2010. **58**(7): p. 1993-1998.

95. Mendis, R., et al., *A Tunable Universal Terahertz Filter Using Artificial Dielectrics Based on Parallel-Plate Waveguides.* Appl. Phys. Lett., 2010. **97**: p. 131106.

96. George, P.A., et al., *Integrated Waveguide-Coupled Terahertz Microcavity Resonators.* Appl. Phys. Lett., 2007. **91**: p. 191122.

97. Bingham, A., *Propagation through Terahertz Waveguides with Photonic Crystal Boundaries (Phd Thesis)*, 2007, Oklahoma State University: Stillwater.

98. Borsboom, P.-P. and H.J. Frankena, *Field Analysis of Two-Dimensional Integrated Optical Gratings.* J. Opt. Soc. Am. B, 1995. **12**(5): p. 1134-1141.

99. Thumvongskul, T. and T. Shiozawa, *Reflection Characteristics of a Metallic Waveguide Grating with Rectangular Grooves as a Frequency-Selective Reflector.* Microwave and Opt. Tech. Lett., 2002. **32**(6): p. 414-418.

100. Itoh, T., ed. *Numerical Techniques for Microwave and Millimeter-Wave Passive Structures.* 1989, Wiley.

101. Fano, U., *Effects of Configuration Interaction on Intensities and Phase Shifts.* Phys. Rev., 1961. **124**(6): p. 1866-1878.

102. Lukyanchuk, B., et al., *The Fano Resonance in Plasmonic Nanostructures and Metamaterials.* Nat. Mater., 2010. **9**: p. 707-715.

103. Fan, S., *Sharp Asymmetric Line Shapes in Side-Coupled Waveguide-Cavity Systems.* Appl. Phys. Lett., 2002. **80**: p. 908.

104. Miroschnichenko, A.E., S. Flach, and Y.S. Kivshar, *Fano Resonances in Nanoscale Structures.* Reviews of Modern Physics, 2010. **82**(3): p. 2257-2298.

105. Prodan, E., et al., *A Hybridization Model for the Plasmon Response of Complex Nanostructures.* Science, 2003. **302**: p. 419-422.

106. Lee, J.W., et al., *Antibonding Plasmon Mode Coupling of an Individual Hole in a Thin Metallic Film.* Phys. Rev. B, 2009. **80**: p. 205417.

107. Preu, S., et al., *Coupled Whispering Gallery Mode Resonators in the Terahertz Frequency Range.* Optics Express, 2008. **16**(10): p. 7336-7343.

108. Smith, D.D., H. Chang, and K.A. Fuller, *Whispering-Gallery Mode Splitting in Coupled Microresonators.* J. Opt. Soc. Am. B, 2003. **20**(9): p. 1967-1974.

109. Bayer, M., et al., *Optical Modes in Photonic Molecules.* Phys. Rev. Lett., 1998. **81**(12): p. 2582-2585.

110. Kuswandi, B., et al., *Optical Sensing Systems for Microfluidic Devices: A Review.* Anal. Chim. Acta, 2007. **601**: p. 141-155.

111. Wu, J. and M. Gu, *Microfluidic Sensing: State of the Art Fabrication and Detection Techniques.* Journal of Biomedical Optics, 2011. **16**(8): p. 080901.

112. Zhu, H., et al., *Integrated Refractive Index Optical Ring Resonator Detector for Capillary Electrophoresis.* Anal. Chem., 2007. **79**: p. 930-937.

113. Hong, J., et al., *A Mach-Zender Interferometer Based on Silicon Oxides for Biosensor Applications.* Anal. Chem. Acta, 2006. **573-574**: p. 97-103.

114. Brandenburg, A., *Differential Refractometry by an Integrated-Optical Young Inteferometer.* Sens. and Act. B, 1997. **38-39**: p. 266-271.

115. Hasek, T., et al., *Photonic Crystals for Fluid Sensing in the Subterahertz Range.* Appl. Phys. Lett., 2006. **89**(173508).

116. Loncar, M., A. Scherer, and Y. Qiu, *Photonic Crystal Laser Sources for Chemical Detection.* Appl. Phys. Lett., 2003. **82**(26): p. 4648.

117. Hanumegowda, N.M., et al., *Refractometric Sensors Based on Microsphere Resonators.* Appl. Phys. Lett., 2005. **87**: p. 201107.

118. Laib, J.P. and D.M. Mittleman, *Temperature-Dependent Terahertz Spectroscopy of Liquid N-Alkanes.* J. Infrared Milli Terahertz Waves, 2010. **31**: p. 1015-1021.

119. Mendis, R., *Nature of Subpicosecond Terahertz Pulse Propagation in Practical Dielectric-Filled Parallel-Plate Waveguides.* Opt. Lett., 2006. **31**(17): p. 2643-2645.

Appendix A

In this appendix is the annotated MATLAB code for calculating the transmission through a grooved PPWG with a dielectric filling by mode-matching analysis. This code is modular so the geometry can be easily modified. The parts of the code are (1) the overall/control program, (2) calculation of the transmission matrix for a groove, (3) function to calculate the β_z solutions for the modes in the dielectric-filled waveguide (Equation [3-65]), (4) calculation of the transmission matrix for a flat waveguide section (such as that between grooves), and (5) a subroutine to calculate the star product of two transmission matrices.

Code 1: Overall Program

```
%Victoria Astley 04/2012
%This model calculates the transmission through a TE-mode PPWG with a
%groove filled with a dielectric.
%Parameters include the waveguide geometry, frequency, the index of
%the dielectric filling material, and the number of modes used in the
%calculation

%Universal variables
freq = 200e9:.1e9:310e9;  %frequency range
K = 44;    %modes in small waveguide
L = 46;    %modes in large waveguide

%Range of indices in each groove.  Each row is a different run of the
%loop.  In this example, both are empty and then both are full of C14
indexrange = [1.00 1.00; 1.4224 1.4224];

%Groove 1
%Define geometry and fill level
%a is the spacing in the waveguide as a whole
%b is the effective spacing in the grooved section (a + groove depth)
%h is the height of the dielectric fill in the groove.  In this case it
%is a perfect fill, but this is not necessary
%zwidth1 is the width of the groove
a1 = 1.000e-3;
b1 = 1.406e-3;
h1 = b1-a1;
```

```
zwidth1 = 711e-6;

%Distance to Groove 2
%zbetween is the distance between grooves
%abetween is the plate spacing in this ungrooved section
zbetween = 2.08e-3;
abetween = 1.000e-3;

%Groove 2
%similar to Groove 1
a2 = 1.000e-3;
b2 = 1.406e-3;
h2 = b2-a2;
zwidth2 = 457e-6;

%Groove 3
%and so on for other grooves, limited only by computingpower

%Loop over each index fill combination
%Find out how many loops are required.
indsize = size(indexrange);    %gives answer as rows x columns.  # rows
is # runs of the loop
ncount = 0;


%First loop - calculations are done for all combinations of dielectric
%filling (empty, one full, both full, etc.) given in indexrange
for ncount = 1:indsize(1)
    fcount = 0;



%Second loop - frequency

      for f = freq
       fcount = fcount+1;

  %For each groove and each flat section between grooves, the
transmission matrices S11, S12, S21, and S22 are obtained
% Variables being passed are the geometry of the section, the index,
the number of modes to calculate and the frequency

        [G1U11 G1U12 G1U21 G1U22] = OneGrooveMatrix(a1, b1, zwidth1,
h1, K, L, indexrange(ncount,1), f);

        [G2U11 G2U12 G2U21 G2U22] = OneGrooveMatrix(a2, b2, zwidth2,
h2, K, L, indexrange(ncount,2), f);

        [Gap11 Gap12 Gap21 Gap22] = FlatSectionMatrix(zbetween,
abetween, K, f);

        %Combine these using the star product.
```

```
        [W11, W12, W21, W22] = starproduct(G1U11, G1U12, G1U21, G1U22,
Gap11, Gap12, Gap21, Gap22);
        [Final11, Final12, Final21, Final22] = starproduct(W11, W12,
W21, W22, G2U11, G2U12, G2U21, G2U22);

        %Output the transmission of the TE1 mode.  Other modes can also
%be specified if desired.
        Trans(fcount, ncount) = abs(Final21(1,1)).^2;
    end
end
```

Code 2: Grooved Section

```
%%Modematching functionalized program.
%Designed to be called as function by some other program
%Inputs: Geometry of the groove, the fill, the indices, modes, and
%frequency range
%Output: The overall transmission matrix only.

function [U11, U12, U21, U22] = OneGrooveMatrix(a, b, zbig, h, K, L,
index, f)


%h0 is the depth of the groove
h0 = b-a;

%for calculating mode patterns, we generate a series of points on the
%y-axis
ymode = (0:1e-6:b);
yiter = size(ymode);


%Constants
epsilon = 8.854187817e-12;
mu = pi*4e-7;
clight = 1/sqrt(mu*epsilon);

%Information about the dielectric filling
er = index^2;      %relative permittivity of the dielectric

%Calculation of frequency variables
lambda = clight / f;
w = 2*pi*f;
k = 2*pi/lambda;

%Clear variables for this part
clear BZ lowest BZtemp By0 Byd relation Ex i NORM

%pre-allocation for memory issues, to make it all faster
```

```
BZtemp = zeros(1, L);
By0 = zeros(1,L);
Byd = zeros(1,L);
relation = zeros(1, L);
NORM = zeros(1,L);
Ex = zeros(yiter(2),L);

%Calculate the Beta values for this waveguide section
%Use separate function, Solver Bz

BZ = SolverBz(L, w, b, h, er);

% Solver Bz returns solutions out of order (the first is not the TE1)
%and so must be rearranged to put in mode order,
% Real solutions are in reverse order, so find highest real answers
% and make it the TE1 solution.  Imaginary solutions are in order.
if any(real(BZ) ~=0)
    lowest = find(BZ == max(real(BZ)));
%by lowest I mean lowest order mode

    for i = 1:lowest
        BZtemp(i) = BZ(lowest+1-i);
    end
   BZ(1:lowest) = BZtemp(1:lowest);
end

%Now it's in mode order, get the By values
for i = 1:L
    By0(i) = sqrt((w^2)*mu*epsilon-(BZ(i)^2));
    Byd(i) = sqrt((w^2)*mu*epsilon*er-(BZ(i)^2));
end


%Calculate the mode patterns.
%start by calculating the relations between the two parts of the Ex
%field pattern, essentially Ao/Ad (without er)

for i = 1:L
    relation(i) = sin(Byd(i)*(h))/sin(By0(i)*(b-h));
end

%Get normalization factors.  Calculated by setting the integral of the
%square (field * complex conjugate) to equal 1.

for i = 1:L
    NORM(i) = sqrt(((h/2) - sin(2*Byd(i)*h)/(4*Byd(i))+
(relation(i)^2)*(b-h)/2 -
(relation(i)^2)*sin(2*By0(i)*(b-h))/(4*By0(i)))^-1);
end

%So equations are
% Exd = NORM*sin(Byd*y)
% Ex0 = NORM*relation*sin(By0*(b-y))
```

```
%Electric field patterns
%This is just to look at, the integrals use the analytical expression

for count = 1:yiter(2)
    for mco = 1:L
        if ymode(count) >= b-h
            Ex(count, mco) = NORM(mco)*sin(Byd(mco)*(b-ymode(count)));
        else
            Ex(count, mco) =
NORM(mco)*relation(mco)*sin(By0(mco)*ymode(count));
        end
    end
end


%Begin calculation of the matrices
%Start with impedances Z1 and Z2

clear Z1 Z2 M

Z1 = zeros(K);
Z2 = zeros(L);
M  = zeros(L, K);

clear fc

for n = 1:K
    moden= n;
        Z1(n) = w*mu / sqrt((w^2)*mu*epsilon - (moden*pi/a)^2);

end


clear fc

for m = 1:L
    modem = m;
        Z2(m) = w*mu / BZ(modem);
end


%Loop to calculate the overlap integrals for all the modes

if h <= h0
%this set is for the fill not coming up to the top of the groove, so
only Ex0 matters
    for n = 1:K
        moden = n;
        for m = 1:L
```

```
            modem = m;


            %Do the overlap integrals
            %Mode in smaller waveguide (normalized:),
            %n is mode in smaller waveguide (1:K)
            %Ex = sqrt(2/a)*sin(n*pi*y/a)
            %Mode in larger waveguide (normalized)
            %Ex0 = NORM*R*sin(By0*(b-y)


            %Analytical solution
            %integrates from 0 to a
            %consider the case in which the groove is empty and the
            %usual mode patterns can be used.
            if By0(modem) == moden*pi/a
               M0 = NORM(modem) * sqrt(2/a)* (a/2 -
sin(2*By0(modem)*a)/(4*By0(modem)));

            %as well as the filled case
            else
               M0 = NORM(modem)*
sqrt(2/a)*relation(modem)*(sin(By0(modem)*a-moden*pi)/(2*By0(modem)-
2*moden*pi/a)-sin(By0(modem)*a+moden*pi)/(2*By0(modem)+2*moden*pi/a));
            end

            M(m,n) = M0;

        end
    end

else
%in this version, the fill comes up above the top, so need Exd and Ex0
    ysep = b-h;
    for n = 1:K
        moden = n;
        for m = 1:L
            modem = m;

           %Do the overlap integrals
            %Mode in smaller waveguide (normalized:),
            %n is mode in smaller waveguide (1:K)
            %Ex = sqrt(2/a)*sin(n*pi*y/a)
            %Mode in larger waveguide (normalized)
            %Ex0 = NORM*R*sin(By0*(b-y))
            %Exd = NORM*sin(Byd*y)


            %Integrates from 0 to ysep, the empty section (measured
            %from the top of the waveguide
            %include special case of empty groove
            if By0(modem) == moden*pi/a
```

```
                M0 = (ysep/2 -
sin(2*By0(modem)*ysep)/(4*By0(modem)))*NORM(modem)*sqrt(2/a)*relation(m
odem);

            %and case that is filled with a dielectric
            else
                M0 = (sin(By0(modem)*ysep-
moden*pi*ysep/a)/(2*(By0(modem)-moden*pi/a))-
sin(By0(modem)*ysep+moden*pi*ysep/a)/(2*(By0(modem)+moden*pi/a)))*NORM(
modem)*sqrt(2/a)*relation(modem);
            end

            %integrates from ysep to a, the filled section
            if Byd(modem) == moden*pi/a
                Md1 = (sin(moden*pi*a/a)^2)/(2*moden*pi/a)-
(sin(moden*pi*ysep/a)^2)/(2*moden*pi/a);
                Md2 = (a/2-sin(2*moden*pi*a/a)/(4*moden*pi/a))-(ysep/2-
sin(2*moden*pi*ysep/a)/(4*moden*pi/a));
                Md = NORM(modem)*sqrt(2/a)*(sin(Byd(modem)*b)*Md1-
cos(Byd(modem)*b)*Md2);
            else
                Md1a = -1*cos(moden*pi*a/a-
Byd(modem)*a)/(2*(moden*pi/a-Byd(modem)))-
cos(moden*pi*a/a+Byd(modem)*a)/(2*(moden*pi/a+Byd(modem)));
                Md1b = -1*cos(moden*pi*ysep/a-
Byd(modem)*ysep)/(2*(moden*pi/a-Byd(modem)))-
cos(moden*pi*ysep/a+Byd(modem)*ysep)/(2*(moden*pi/a+Byd(modem)));
                Md1 = Md1a-Md1b;

                Md2a = sin(Byd(modem)*a-moden*pi*a/a)/(2*(Byd(modem)-
moden*pi/a))-
sin(moden*pi*a/a+Byd(modem)*a)/(2*(moden*pi/a+Byd(modem)));
                Md2b = sin(Byd(modem)*ysep-
moden*pi*ysep/a)/(2*(Byd(modem)-moden*pi/a))-
sin(moden*pi*ysep/a+Byd(modem)*ysep)/(2*(moden*pi/a+Byd(modem)));
                Md2 = Md2a-Md2b;

                Md = NORM(modem)*sqrt(2/a)*(sin(Byd(modem)*b)*Md1-
cos(Byd(modem)*b)*Md2);
            end

            M(m,n) = Md + M0;

        end
    end
end



%Impedance matrices
clear Y1 Y2 Yx
Y1 = zeros(K,K);
Y2 = zeros(L,L);
```

```
for p = 1:K
Y1(p,p) = 1/Z1(p);
end

for q = 1:L
Y2(q,q) = 1/Z2(q);
end

%Combo matrix
Yx = M'*Y2*M;
Yy = M*Y1*M';

IK = eye(K,K);
IL = eye(L,L);

%Scattering matrix coefficient definitions, from small to big waveguide
%small to big designated as A
%big to small designated as B
SA11 = (Yx+Y1)\(Y1-Yx);
SA12 = 2*inv(Y1+Yx)*M'*Y2;
SA21 = M*(IK+SA11);
SA22 = M*SA12-IL;

SB11 = SA22;
SB12 = SA21;
SB21 = SA12;
SB22 = SA11;

%Propagation matrix through the grooved section
Tbig11 = zeros(L,L);
Tbig22 = zeros(L,L);
Tbig12 = zeros(L,L);
Tbig21 = zeros(L,L);

for m = 1:L
    modem = m;
    Tbig12(m,m) = exp(1i*BZ(modem)*zbig);
    Tbig21(m,m) = exp(1i*BZ(modem)*zbig);
end



%Combine matrices for the groove as a whole
clear W11 W12 W21 W22
clear V11 V12 V21 V22
clear U11 U12 U21 U22


%Start with the first junction
W11 = SA11;
W12 = SA12;
W21 = SA21;
```

```
W22 = SA22;


%Combine with the transmission to the next junction
[W11, W12, W21, W22] = starproduct(W11, W12, W21, W22, Tbig11, Tbig12,
Tbig21, Tbig22);

%and then the second junction
[W11, W12, W21, W22] = starproduct(W11, W12, W21, W22, SB11, SB12,
SB21, SB22);

%Export the final transmission matrix
U11 = W11;
U12 = W12;
U21 = W21;
U22 = W22;
```

Code 3: Solutions for β_z

```
%Calculation of the solutions for the dielectric filled waveguide
%section
function  [Bzero] = SolverBz(L, w, b, h, er)

clear sol
clear solcheck
clear count
clear Bzero


epsilon = 8.854187817e-12;
mu = pi*4e-7;

%Define the function, Equation [3-65]

Bz = @(x) (sqrt((w^2)*mu*epsilon*er-
(x^2))/mu)*cot(h*sqrt((w^2)*mu*epsilon*er-
(x^2)))+(sqrt((w^2)*mu*epsilon-(x^2))/mu)*cot(sqrt((w^2)*mu*epsilon-
(x^2))*(b-h));

%Range of Bz values to be checked.
%These are used to set the limits for the fzero solver
Bzrange = [0:1:1e5 1e5:10:3e5];
rangetotal = size(Bzrange);

count = 0;
Bzero(1) = 0;
```

```
for i = 1:rangetotal(2)

      %Look between each set of possible points.  If there's a sign
%change, look for a solution (else it will find points that are not
%solutions
    if Bz(Bzrange(i)) < 0 && Bz(Bzrange(i+1)) > 0
         sol = fzero(Bz, [Bzrange(i) Bzrange(i+1)]);


        %check that it's a true solution.  Not an asymptote, and not a
       % negative value (nonphysical)
        solcheck = Bz(sol);

      if solcheck >= -100 && solcheck <= 100 && real(sol) >= 0 &&
imag(sol) >= 0
         if any(abs(Bzero-sol) <= .1)
                %do nothing, it's already on the list
         else
                count = count+1;

            %%real solutions are found in reverse order, so solutions
get added to the beginning of the list until all are real solutions
have been found.  Then the first L modes on the list are the lowest L
modes and are returned to the calling function. %%
                if count > L
                    for mit = 1:(L-1)
                        Bzero(mit) = Bzero(mit+1);
                    end
                    Bzero(L) = sol;
                else
                    Bzero(count) = sol;
                end

         end
      end


    end
end

%%once all the real values have been found, if we still need solutions
for even higher-order modes, we can search for imaginary ones, using
Bzrange*i as our test range. These solutions come up in the correct
order so the first L-count are all that are needed.%%

if count < L
    for i = 1:rangetotal(2)

        %Look for the change in sign, get solution
        if Bz(Bzrange(i)*j) >0 && Bz(Bzrange(i+1)*j) < 0
            sol = fzero(Bz, [Bzrange(i)*j Bzrange(i+1)*j]);
```

```
            %check that it is a true solution
            solcheck = Bz(sol);
            if solcheck >= -100 && solcheck <= 100 && real(sol) >= 0 &&
imag(sol) >= 0
                if any(abs(Bzero-sol) <= .1)
                    %do nothing
                else
                    count = count+1;
                    Bzero(count) = sol;
                end
            end

            if count >= L  %we only need L solutions
                break
            end
        end
    end
end
```

Code 4: Flat Section Between Grooves

```
%Calculate the transmission matrix on the ungrooved waveguide sections

function [T11, T12, T21, T22] = FlatSectionMatrix(zbetween, abetween,
K, f)

epsilon = 8.854187817e-12;
mu = pi*4e-7;
clight = 1/sqrt(mu*epsilon);

k = 2*pi*f/clight;

 T11 = zeros(K,K);
 T22 = zeros(K,K);
 T12 = zeros(K,K);
 T21 = zeros(K,K);

 for n = 1:K
     moden = n;
     betan = sqrt(k^2-(moden*pi/abetween)^2);
     T12(n,n) = exp(j*betan*zbetween);
     T21(n,n) = exp(j*betan*zbetween);
 end
```

Code 5: Star Product routine

```
function [U11, U12, U21, U22] = starproduct(W11, W12, W21, W22, V11,
V12, V21, V22)

%Calculates the "star product" for mode-matching calculations


[size1 size2] = size(V11*W22);
I1 = eye(size1, size2);

U11 = W11 + W12*inv(I1-V11*W22)*V11*W21;
U12 = W12*inv(I1-V11*W22)*V12;
U21 = V21*inv(I1-W22*V11)*W21;
U22 = V21*inv(I1-W22*V11)*W22*V12+V22;
```